Finite Element Modelling of a Transmission Steel Lattice Tower Based on LiDAR Point Cloud Data

An Automatic Procedure for

Geometrical Model Generation

Author: Filip Wrzosek

TU Delft

Finite Element Modelling of a Transmission Steel Lattice Tower Based on LiDAR Point Cloud Data

An Automatic Procedure for

Geometrical Model Generation

by

Filip Wrzosek

in partial fulfillment of the requirements for the degree of

Master of Science in Civil Engineering

at the Delft University of Technology,

to be defended publicly on Thursday August 4, 2022 at 11:00 AM.

Abstract

A series of critical transmission lattice towers failures due to severe ice and wind loads forced German utility companies to reassess the structural stability of their power grid infrastructure. During the structural reassessment process, a problem related to an outdated or even missing documentation of the in-use infrastructure occurred. This issue forced utility companies to gather the data regarding the geometry of the lattice towers on-site, using specialized and labor-intensive geodetic measuring methods. The scale of the required data acquisition endeavor and stability checks to be performed encouraged the use of alternative methods to capture the geometry of the in-situ structures and reconstruct geometric models to be applied during the structural stability checks in a reliable and efficient way.

This work presents an innovative method to generate a geometric CAD model using point cloud data captured by a LiDAR scanner. The CAD model can be later implemented for FEA utilized during structural stability assessments. The modeling process defined in this study is fully automatized, enabling to obtain repeatable results and save the time required for manual data processing. For the input point cloud data, two types: Aerial and Terrestrial LiDAR point clouds have been investigated allowing to identify the applicability of both data sets for the proposed method.

The model generated with the automatic method proposed in this study is compared in terms of geometric discrepancies to an idealized model based on design documentation and a LiDAR point cloud based model manually generated with a commercial software. The two models used for comparison depict a traditional structural engineering approach and a state-of-the-art method within the point cloud processing field accordingly. At the final stage of this work, the automatically generated point cloud based model is used for a non-linear FEA and compared to a FEA response of the idealized model.

Results showcase that LiDAR point cloud data is a good source of geometric information to reconstruct a geometric CAD model which can later be implemented in FEA. Obtained results are comparable to the ones of an idealized model based on design documentation in terms of collapse mechanism and ultimate load applied at the failure step. Additionally, the geometrical comparison between the point cloud based models generated with the manual method and the one proposed in this work underline the advantage of the automatic method in terms of permissible level of detail and overall precision of the final geometric model. What is more, the impact of point cloud data usage for FEA modeling is shown. Investigating differences between FEA results of the point cloud based and idealized models allow to showcase the influence of real life imperfections on force redistribution across the analyzed structure and ultimate forces reached by members loaded in compression.

The modeling method and analysis results presented in this work can be applied as a set of guidelines for future applications related to point cloud data processing of steel lattice structures used for FEA modeling purposes.

I dedicate this work to my grandmother Stefania Kadzikowska

Acknowledge

Contents

1 Introduction

In this chapter an introduction to the research will be given. Section 1.1 focuses on the problem statement for the Thesis, following with defining the research questions in Section 1.2. In the last Section 1.3, the outline of the work is described and presented on a schematized graph.

1.1   Problem statement

German utilities are forced to reassess the structural stability of their greater than 110kV lattice towers. The reason behind it is a series of critical tower failures due to ice and wind loads in 2005 and the following black outs across western Germany [1]. An example of a lattice tower collapsed during that period is presented in Fig. 1.

Figure 1 Collapse of the lattice tower [1]

The vast majority of structures has outdated technical drawings or the documentation does not exist anymore. The lack of technical documentation encourages usage of innovative solutions for three-dimensional (3D) geometric model generation which could be later utilized in a finite element analysis(FEA), an integral part in the process of determining a tower's structural stability.

In this study, an approach for a 3D geometric model generation method using point cloud data will be proposed. The hypothesis of this thesis is that the approach will allow to refine the finite element analysis procedure by allowing to work on in-situ based models rather than referencing outdated design documentation, which might differ from the current state of the tower. The analysis has to follow current EU Norms and standards including VDE-AR-N 4210, a document prepared after the 2005 failures [2]. Notably, additional safety factors (SF.s) were introduced in these standards, in which the magnitude of the SF.s depend on the location and level of importance of the tower.

The tower analyzed in this work is standing next to the river "Weser", close to the city of Bremen, Germany. The tower was built in 1979, has a height of 110 meters. Point clouds were gathered using terrestrial and drone-based LiDAR scanners. Both data types will be utilized to generate 3D geometric models using two different approaches explained in the state of art and presented in the methodology.

The main goal of this thesis is to investigate if a point cloud data captured by LiDAR scanners is a sufficient source of information to create an accurate geometric model for FEA of lattice towers. Moreover, a comparison of the FEA results between a traditional model based on original design drawings and one derived from a point cloud data set will be conducted. The limitations and advantages of point cloud usage for FEA will also be addressed in the work.

1.2 Research Question & Objectives

1.2.1 Research Questions

The work presented in this thesis will allow to answer two research questions stated below:

- ***Does LiDAR point cloud data acquired by an aerial/terrestrial scanner provide sufficient geometric information to create a 3D geometric model with level of detail adequate for FEM application?***

- ***How does discrepancy of 3D geometric model based on point cloud data compared to an idealized 3D geometric model based on technical drawings impact FEA results?***

1.2.2 Objectives

To answer the aforementioned research questions a set of objectives have been formulated:

- Assess the applicability of the acquired LiDAR point cloud data for geometric features extraction of the analyzed lattice tower,

- Investigate the difference between the geometry of an in-situ based steel profile and idealized steel profile based on EN 1090-2 specification,

- Generate geometric models using three different approaches:

  - **Idealized model**, based on design documentation depicting the traditional modeling approach utilized in Civil Engineering, serving the purpose of the reference model.
  - **Manually generated point cloud based model**, representing a point cloud processing state-of-the-art method using commercial software.
  - **Automatically generated point cloud based model**, based on the innovative method proposed in this thesis.

- Identify differences in geometry of point cloud based models compared with the idealized model,

- Investigate differences in results for FEA performed on the idealized model and the automatically generated point cloud based model.

1.3   Thesis Outline

The thesis report consists of 6 Chapters addressing the research questions in Section 1.2. Chapter 2 summarizes the literature study carried during the work, allowing the reader to understand about terminology and state of the art procedures performed during point cloud processing. Chapter 3 presents the methodology defined for the purposes of this work. Chapter 4 describes the FEA assumptions and conditions applied during the analysis. Chapter 5 presents the results of the study divided into two parts, a geometrical comparison of all models generated and the finite element analysis results. The last chapter will draw conclusions and recommendations regarding the topic. A schematized outline of the thesis is provided in Fig. 2.
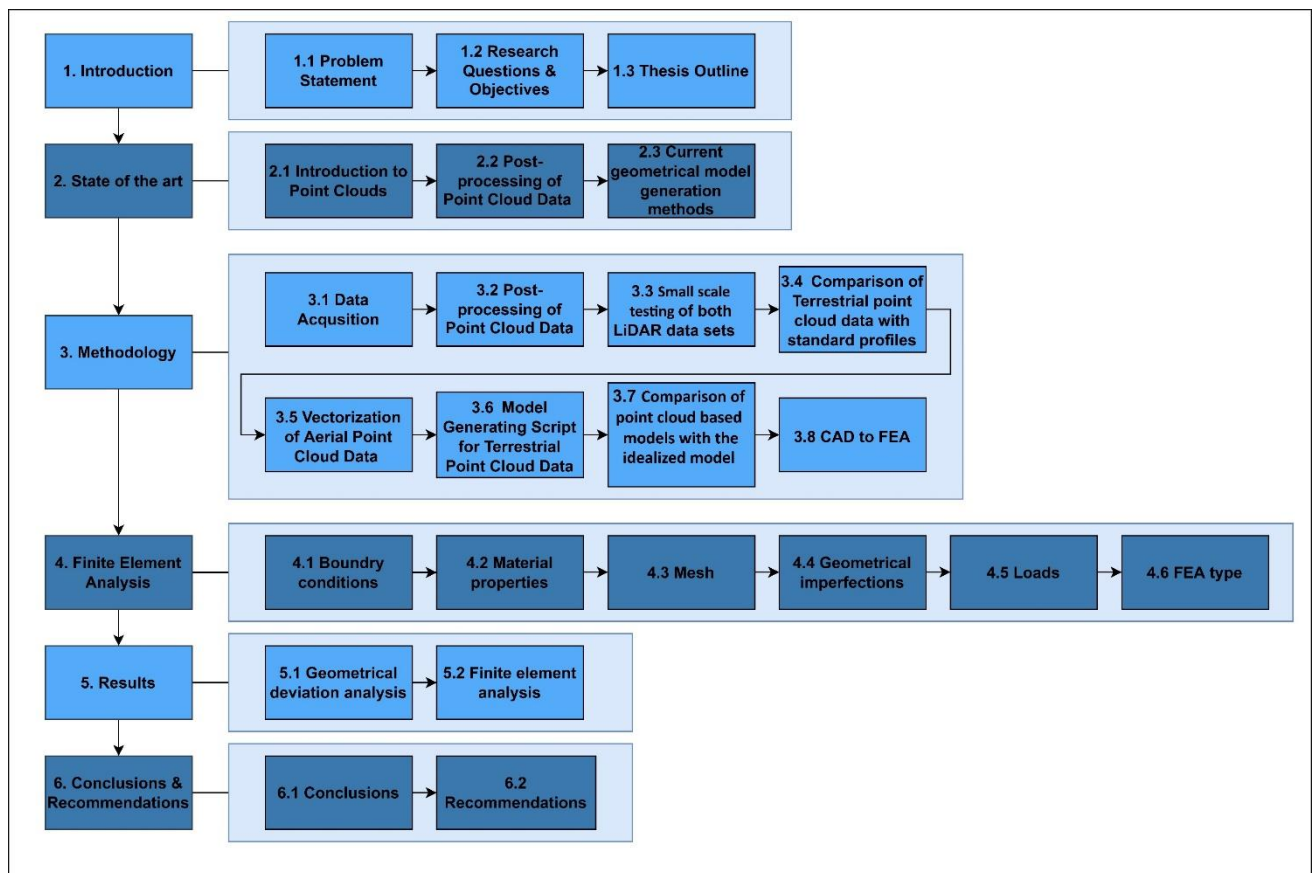
Figure 2 Thesis outline
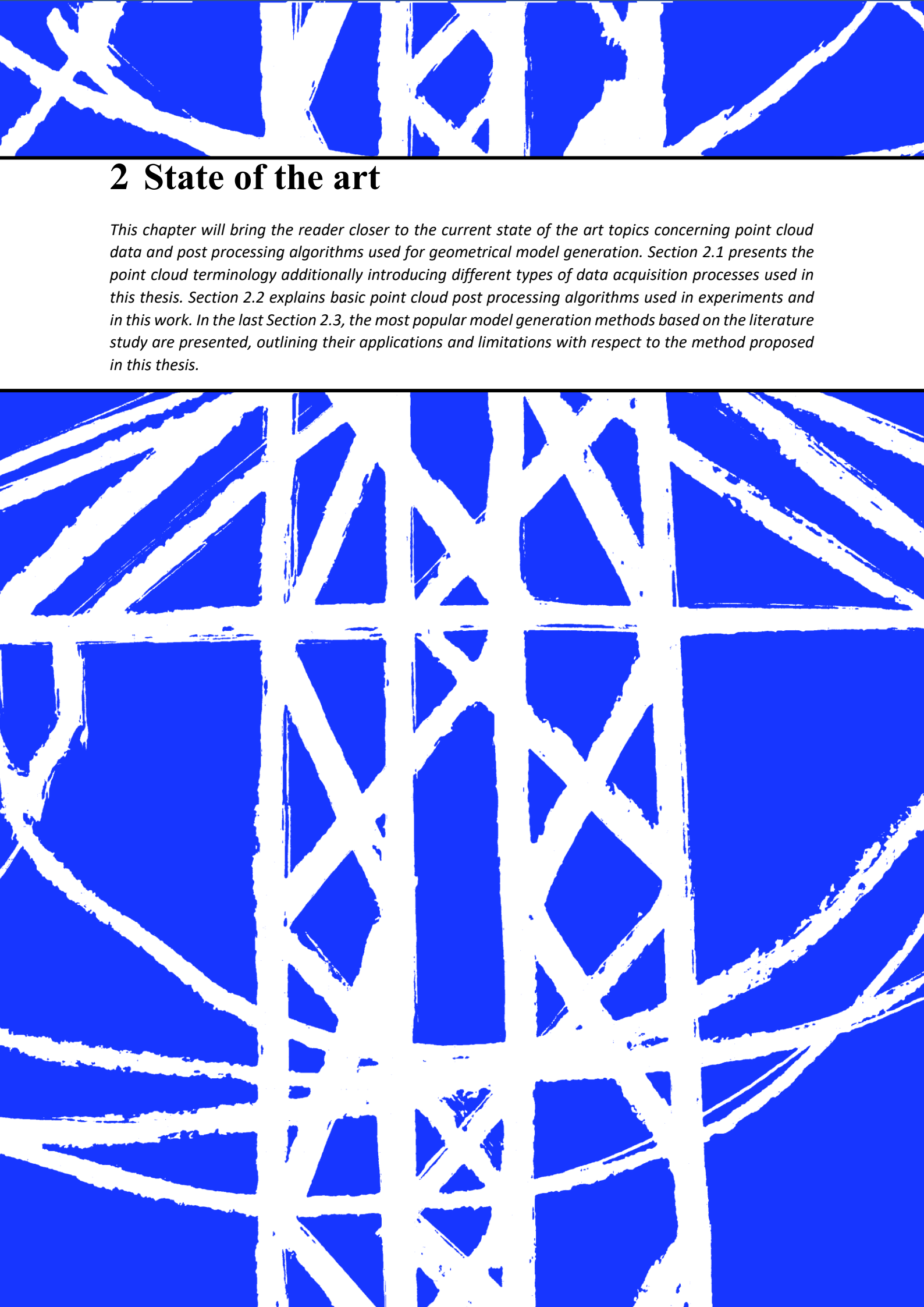
2 State of the art

This chapter will bring the reader closer to the current state of the art topics concerning point cloud data and post processing algorithms used for geometrical model generation. Section 2.1 presents the point cloud terminology additionally introducing different types of data acquisition processes used in this thesis. Section 2.2 explains basic point cloud post processing algorithms used in experiments and in this work. In the last Section 2.3, the most popular model generation methods based on the literature study are presented, outlining their applications and limitations with respect to the method proposed in this thesis.

2.1   Introduction to Point Clouds

What is a point cloud? What is a LiDAR point cloud and how does it differ from other types of point cloud data? These among other questions regarding point cloud data and the acquisition process will be addressed in this Section. What is more, data acquisition procedures for LiDAR point cloud data will be introduced showcasing the advantages and disadvantages of both solutions utilized in this work.

2.1.1   Point Cloud data

A definition of a point cloud relevant for this work could be stated as a data set consisting of points in a three dimensional Cartesian coordinate system. Each point consists of x, y and y. Additionally, depending on the scanning method every point can contain more information, like: color code or intensity which helps to group points inside the entire data set. Example of a point cloud is depicted in Fig. 3.
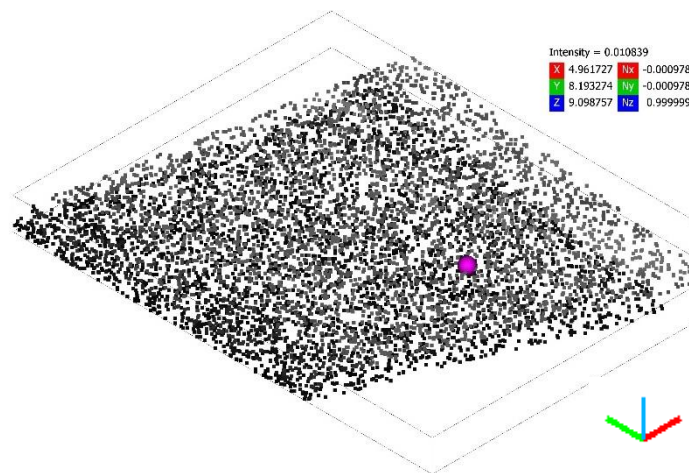
Figure 3 Point cloud example

Commonly, point clouds are the output of a 3D scanning or photogrammetric processes, which by definition are an indirect measuring method of a real-life object. Depending on sensors, data acquisition method, environment, and objects, quality and quantity of the point cloud can be varied. Both methods introduce measuring errors in a form of noise and inaccuracies of points, as shown in Fig. 4.

Figure 4 Point cloud data noise.

Noisy points highlighted with darker color

Data inaccuracies are unavoidable and are the main issue during the reconstruction of the object in digital format. Point cloud features like intensity or RGB color and known geometrical properties of the measured object can be used to filter out the noise during the pre-processing stage, presented in Section 2.2. When processing point clouds, the data quality should be assessed by measuring errors and making sure the accuracy of our point cloud is higher than the desirable precision of the output geometric model. The evaluation of point clouds used in this work will be provided in Section 3.2. Based on the literature study, the topic of assessing point cloud quality for Civil Engineering applications is not usually addressed. Many researchers focus on the extraction of geometrical information from the point cloud, assuming the quality of the data as a known variable provided by the specification of the hardware or the person responsible for data acquisition [3].

2.1.2   Point Cloud data in Civil Engineering

Point Cloud data usage is becoming more and more popular in Civil Engineering industry. Point cloud to BIM, inspection and maintenance or monitoring of deflections are popular topics of point cloud data applications [4, 5, 6]. Although, its application is limited to acquiring geometric information by measurements inside the point cloud data rather than converting the point cloud to a geometric model [7].

Using point cloud data to generate FEM models for Civil Engineering applications is not a new research concept. Many researchers have worked on the topic with different results [8]. Based on the current state-of-the-art, a majority of work focuses on 3D building reconstruction of robust buildings with large flat surfaces [9] like concrete structures. Another common research topic are digital reconstructions of bridges. In this case, a CAD software is employed to create the geometric model for FEM application from point clouds [7]. Additional examples of point cloud usage will be provided in Section 2.3a higher focus is put on structures with large and simple geometrical shapes, while the topic of steel lattice structures is omitted. An example of a point cloud application for geometric model reconstruction of a building rooftop is depicted in Fig. 5.
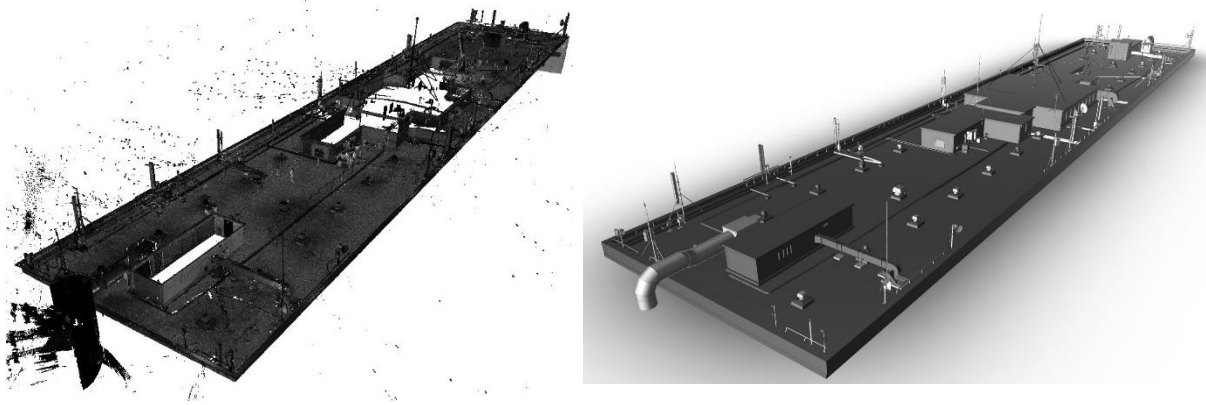
Figure 5. Point cloud application in Civil Engineering industry.
Point cloud (left), CAD model (right).

2.1.3 LiDAR Point Cloud

Laser scanners are a popular choice as data acquisition technology due to its ability to acquire high quality point cloud with less noise compared to photogrammetric solutions [10]. Laser scanners use LiDAR(Light Detection and Ranging) technology as the basic measurement principle. LiDAR technology is based on the measurement of the time delay between light pulse travelling from a scanner to a reflective target surface and back to a scanner allowing to evaluate the distance of the scanned object from the measuring device [10], Fig. 6 depicts a technical scheme of the process.
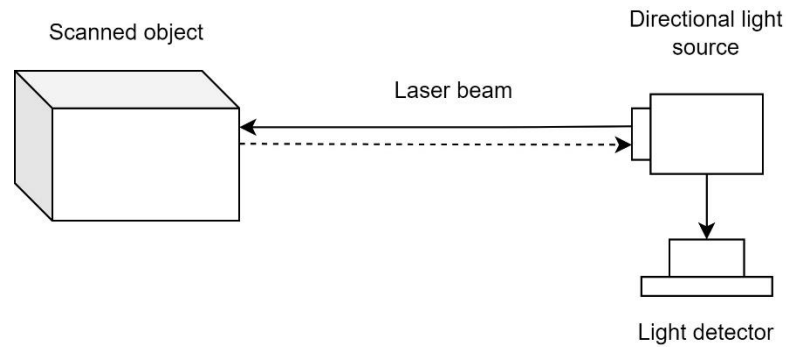
Figure 6 LiDAR technical scheme

As the output of the data acquisition, a LiDAR point cloud is generated with the x, y and z coordinates and additional features specified for every point. The most common attribute of a LiDAR point cloud are intensity values and Red Green Blue(RGB) colors. Fig. 7 depicts a LiDAR point cloud, in which the points are rendered by the intensity value.

Figure 7 LiDAR point cloud, scalar field gradient on right

The decision to use the point cloud data to reconstruct a model of a steel lattice tower was based on advantages mentioned in the beginning of this Section. What is more, LiDAR data required less expertise in the pre-processing step when generating the point cloud from the acquired data. Therefore, LiDAR scanning was a more suitable data acquisition method to be applied during this work.

LiDAR scanners can be classified into three types: terrestrial, mobile and aerial. Whereas, mobile scanners are used to acquire data on larger areas for example point clouds of entire cities gathered with a LiDAR scanner mounted on top of a car, terrestrial scanning focuses on isolated objects. Aerial LiDAR

scanning is utilized for both of those applications using aerial vehicles of different sizes. The large difference in data acquisition processes for all given types results in varying point cloud densities and accuracies. A detailed description of both types of LiDAR scanning methods is provided in Sections 2.1.4 and 2.1.5 accordingly.

2.1.4   LiDAR Terrestrial scanning

Terrestrial laser scanning(TLS) uses a static measuring device which gathers the data from a fixed position. In order to capture the entire structure multiple scans need to be acquired. Compared with aerial LiDAR scanner, a fixed placement of the device allows for higher accuracy of the point cloud with smaller errors due to scanner movement. The field of view of the static scanner is limited. Therefore, to obtain full coverage of an object, point clouds from multiple scanning stations must be registered. During the merging process additional errors are introduced caused by registration issues, an example is depicted in Fig. 8.
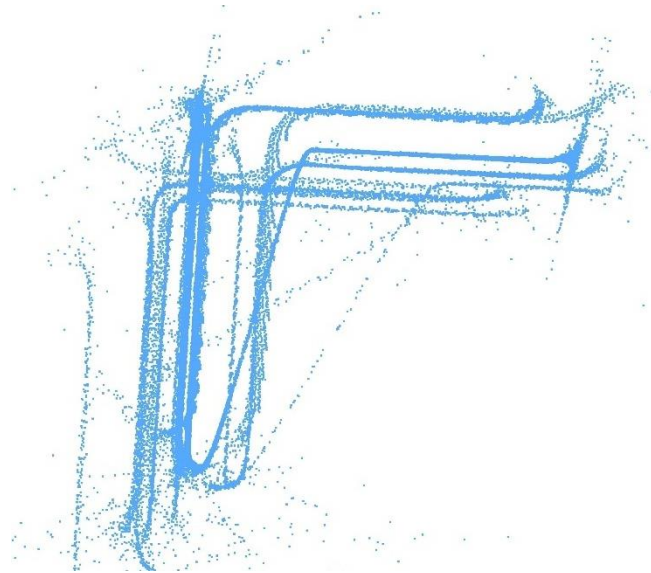
Figure 8 Registration issue

The cross-sectional view of a point cloud of a scanned L shaped member (Fig. 8) depicts the registration issue caused by poor alignment of data points from different scanning stations used to scan the member from multiple sides.

 What is more, the point density is not constant, it decreases the further the object is from the scanner. The non-uniform density of the point cloud is especially apparent for high structures, for which the point cloud density deviation can be significant and have an impact on final processing results. Nonetheless, despite the problems mentioned above, the quality of the point cloud data captured with a terrestrial laser scanner is superior compared to data gathered with an aerial laser scanner. The overall point density and accuracy are much higher. The main reason behind it is the time spend on acquiring the data from one position. The longer the object is scanned the more points are generated for the data set. A visual comparison of the two different point clouds derived from a drone and TLS is depicted in Fig. 9.
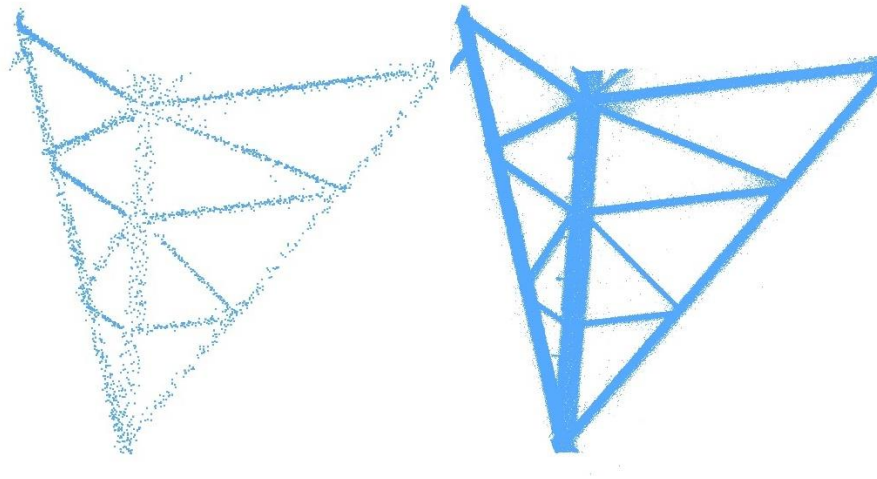
Figure 9 Aerial(left) and Terrestrial(right) LiDAR point loud

2.1.5   LiDAR Aerial scanning

Aerial laser scanning(ALS) originates from point cloud data acquisition for large terrain surveys, primarily planes and helicopters were used to scan landscapes allowing for short data collection time. With improvement of LiDAR scanning hardware aerial laser scanning became an attractive method to collect detailed scans of structures. The closer the LiDAR scanner is to the scanned object the higher the point density of the acquired data, due to safety reasons manually controlled aircrafts could not be used. Fortunately, the development of unmanned aerial vehicles (UAV) (also known as drones) allowed to mount LiDAR scanning devices on the unmanned aircrafts enabling to decrease the scanning distance. Incorporating UAV into ALS opened new opportunities for laser scanning, becoming an alternative to TLS in high resolution scanning of structures. The main difference between the ALS and TLS is the data acquisition process. While TLS devices requires a fixed placement during acquisition, ALS is always in the move allowing to capture larger areas of the structure in a single scan . What is more, ALS captures a nearly uniform density point cloud. The scanning device is always at a similar distance range from the scanned object which enables to gather data of almost uniform density in every part of the structure. Nonetheless, ALS biggest drawback is caused by the constant movement of the LiDAR device. The accuracy and density of the point cloud cannot compete with TLS data (Fig. 10). For tower-like structures with substantial height, an aerial laser scanner is a suitable solution, allowing for data acquisition with a more uniform density along the altitude.
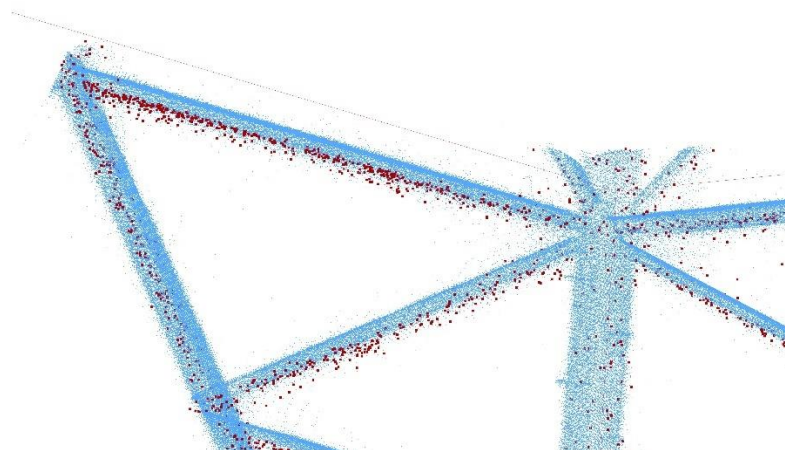
Figure 10 Comparison between Aerial(red) and Terrestrial(blue) point loud density

What is more, using drones for data acquisition can be very effective. The UAV can scan the entire power grid in one flight instead of scanning every mast separately. Nevertheless, until the available hardware of ALS cannot compete with the TLS devices in terms of the point cloud quality the question of what scanning approach is superior is left open. In this work, both types for LiDAR point clouds will be utilized which will allow to compare the data sets and outline pros and cons of both approaches for the analyzed lattice tower.

2.2   Post-processing of Point Cloud

How to treat point cloud data? What are the algorithms to classify, cluster and filter point cloud data in order to read geometrical information from the data set? These among other questions regarding post processing of point clouds will be addressed in this Section, enabling the reader to better understand the basic algorithms utilized in this work required for the model generating script introduced in Section 3.5.

2.2.1   Kernel Density Estimation

Kernel density estimation(KDE) allows to estimate in a non-parametric manner the probability density function(pdf) of a random variable [11]. Compared to a histogram, a simpler probability density function, its shape is smooth and not as highly dependent on the number of intervals to which the sample is divided. A definition based on [11] is given below:

Definition:
Let (x_1, x_2, …, x_n) be independent and identically distributed samples drawn from distribution with an unknown density f at any given point x. We are interested in estimating the shape of this function f. Its kernel density estimator is:

$$\hat{f}_h(x) = \frac{1}{n}\sum_{i=1}^{n} K_h(x - x_i) = \frac{1}{nh}\sum_{i=1}^{n} K\left(\frac{x - x_i}{h}\right)$$

Equation 1

Where n is the sample size, K is the kernel smoothing function and h is the bandwidth.
K defines the shape of the curve used to generate the probability density function.
The bandwidth h allows to determine the smoothness of the density curve and indirectly defines the number of peaks visible in the curve the larger the bandwidth is the less peaks are depicted.

Kernel density estimations application in point cloud processing allows to search for large concentrations of points based on the peak values derived from a probability density shape generated by KDE. As KDE originally operates with a single variable the search for peaks is usually done only for one coordinate of the point cloud. An example of a KDE search is depicted in Fig. 11.
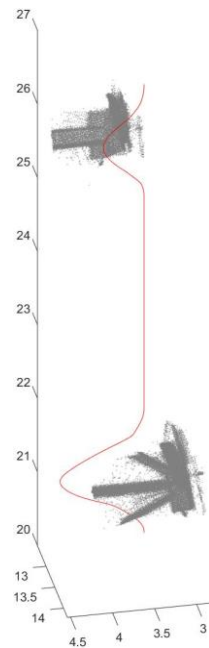
Figure 11 KDE search applied to a point cloud

As shown in Fig. 11, in the KDE function applied along the altitude two peaks in regions of high concentration of points are visible. By defining the location of a peak in the KDE function we can localize important regions in our point cloud which allows us to segment our data based on those locations. The application of KDE in this work will be described in Section 3.5.1.

2.2.2 Octree

Octree allows to divide a three dimensional space into voxels in a tree data structure manner. It is often used in 3D graphics and point cloud processing to reduce the computational time of the data processing. Fig. 12 depicts a recursive subdivision of a 3D space into smaller voxels.
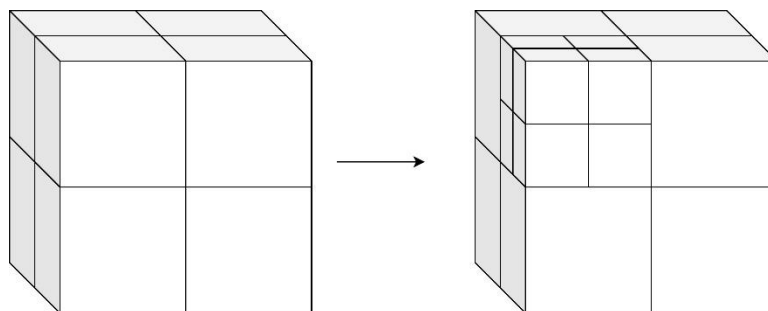
Figure 12 Recursive subdivision of a voxel

Each voxel contains data points stored inside its volume. The subdivision recursively process until the defined voxel size is reached or a given voxel is empty(no information is stored inside the voxel). For point cloud processing, octree algorithms are a useful tool to simplify the data set. An example of an octree applied to a point cloud is given in Fig. 13.
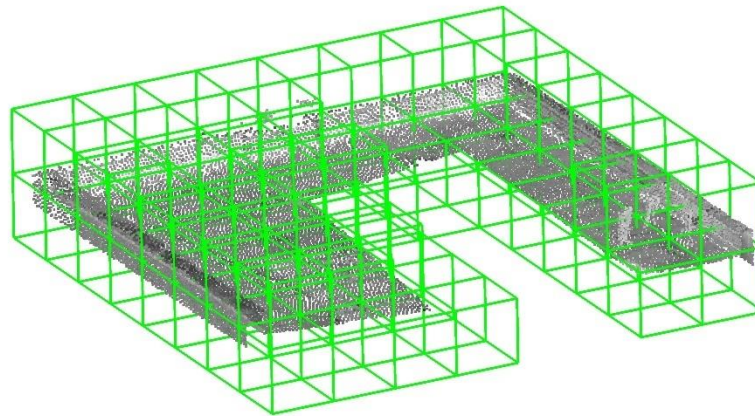
Figure 13 Octree applied to a 3d point cloud

During point cloud processing, the voxel point cloud can be utilized in classification, segmentation and geometric modelling of the original point cloud data. The use of octree allows to reduce the computational time and avoid issues caused by the noise and outliers of the original data set. The application of Octree can be found in Section 3.5.2.

2.2.3   Region growing

Region growing is a popular segmentation algorithm utilized in digital image processing [12] and became a very useful tool for point cloud data applications. The algorithm aims to subdivide the data into regions defined by specific features like normal vectors or color values . An example of the region growing applied to a point cloud data is depicted in Fig. 14.
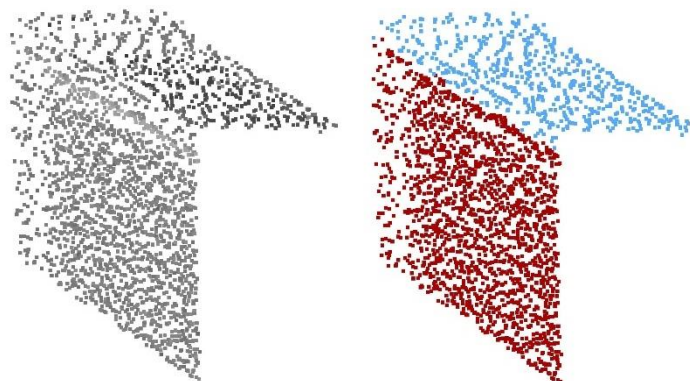
Figure 14 Region growing applied to the point cloud.

Original point cloud (left), data subdivided into two regions (right).

The data set in Fig. 14 is segmented based on the directional vectors of points, which represent a normal vector of the best fit plane of neighboring points. Applying region growing to the data presented in the example allows to divide points into two segments representing the flanges of the scanned L-shaped profile. The two detected regions/planes colorized in a red and blue (Fig. 14, right). A more detailed applications of the region growing in this work will be described in Section 3.5.2.

2.2.4 Nearest neighbor search

Nearest neighbor search (KNN) is a non-parametric classification algorithm which allows to gather information of K-neighboring points for the given query point in a given distance radius. Applying KNN algorithm to a point cloud data set allows to extract information regarding density, outliers and data issues. Points having small number of neighboring points or large distances from other points can be filtered out considering them as outliers. By filtering outlier points, a negative impact of point cloud quality on further processing of the point cloud can be minimized. Fig. 15 illustrates a KNN algorithm applied to a point cloud.
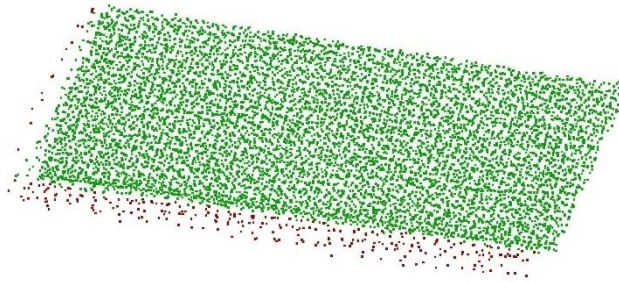
Figure 15 KNN applied to a 3d point cloud

Red and green points represent outliers and valid points accordingly. The application of the KNN in this work will be described in Section 3.5.2.

2.2.5 Hough Transform

The Hough transform allows to extract geometrical features from images. It is a commonly used technique in digital image processing. The method was first introduced by P.V.C Hough in 'Machine analysis of bubble chamber pictures'[13] in which he was able to define lines of colinear points in a binary image by deriving points of concurrent lines in a parameter space. The parameter space is a two-dimensional space defined by the slope and intercept coefficients of the parametric line equation. The concurrent lines are lines in the parameter space representing each point(white pixels) in the binary image. By computing the intersection points of the concurrent lines in the parameter space we can define the line parameters of the colinear points line in our binary image.

$$y = ax + b$$

<div align="right">*Equation 2*</div>

Another way of defining the parameter space is by θ and ρ parameters of the equation:

$$\rho = x * cos\theta + y * sin\theta$$

<div align="right">*Equation 3*</div>

Where ρ is the distance from the origin to the line along a vector perpendicular to the line and θ is angle between the x axis and this vector. Fig. 16 depicts an exemplary problem in both image and parameter space.
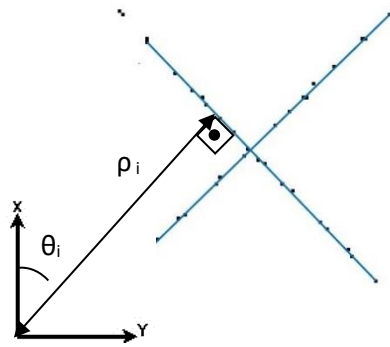
Figure 16.1 Hough transform, binary image
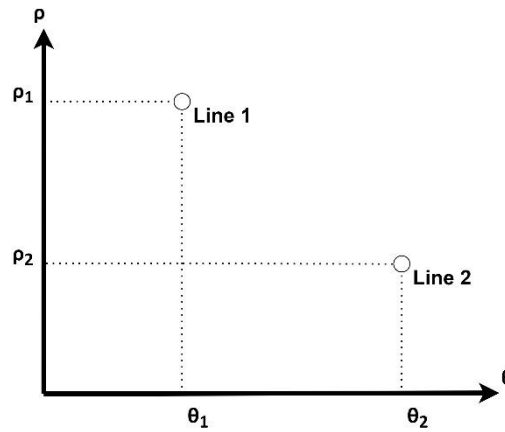
Figure 16.2 Hough transform, parameter space.

Vertical axis- ρ, horizontal axis ϑ

Its application in point cloud processing requires transformation of the analyzed 3D point cloud into a binary image, which is possible by projecting the points on a plane. The application of the Hough Transform in this work will be described in Section 3.5.2.

2.3 Current geometrical model generation methods

What are the current methods of generating geometrical models using point cloud data in Civil Engineering applications? How those methods can be implemented in the method proposed in this thesis? These among other questions will be addressed in this Section.

As stated in Section 2.1.2, point cloud data processing for reconstruction of digital models of in-situ structures in Civil Engineering applications focuses on buildings with larger structural elements. Amongst different model generating methods the most popular approaches will be presented below.

2.3.1 Shape fitting

Shape fitting mentioned in this study is a process converting point clouds representing 3D topographic information of object surfaces into primitive shapes. The process can be conducted manually or by aid of semi-automatic algorithms [14]. For structures with large flat surfaces, like concrete slabs or walls, measurements can be easily extracted directly from the point cloud without any complex data processing. The geometrical model is then reconstructed based on those dimensions. Fig. 17 depicts an example of that process.
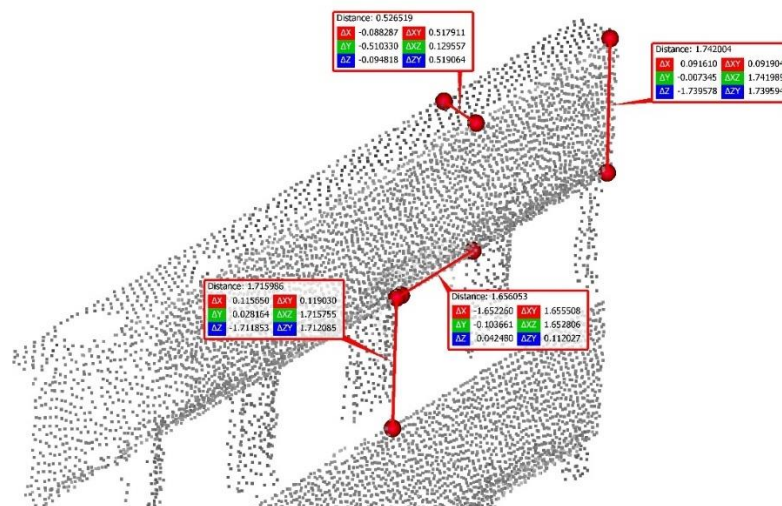
Figure 17 Manual measurement of point cloud data

As one can imagine, the manual extraction of all the dimensions for a complex structure is time consuming, therefore semi-automatic or automatic methods are introduced to reduce the model generation time. RANSAC based methods are very popular for primitive detection in computer vision [15], due to their good accuracy combined with high computational speed. The main issue with the RANSAC approach for point cloud data comes from the dependency of the results on the data set quality. The results of the shape fitting are dependent on the point density and noise level. High point cloud density and low noise are easier to obtain for small objects in a controlled environment, unfortunately acquiring data of a structure in a real environment introduces more data issues described in Section 2.1. The relative accuracy of popular TLS LiDAR scanners estimates in a centimeter range [16]. Therefore, results of shape fitting allows to capture dimensions for concrete or masonry structures within allowable accuracy by EN standards [17], which enable to gather information about the global geometry of those structures. Nevertheless, accuracy within a centimeter range is not enough for steel profiles, where millimeter accuracy is required. Therefore applying shape fitting methods to TLS LiDAR point clouds of

complex steel structures with millimeter thick cross-Sectional members does not allow to reconstruct an accurate geometrical model for FEA purposes.

2.3.2   Point cloud meshing

Meshing a point cloud allows to reconstruct 3D surfaces of the scanned object. Within the current state of the art two approaches are used to create meshes from point clouds:

- Delaunay Triangulation
- Poisson Surface Reconstruction

Delaunay Triangulation

Delaunay Triangulation is based on work of Boris Delaunay titled 'Sur la sphère vide'[18]. The method uses a triangular mesh to define a surface for a set of points on a plane. In order to apply the method to a three-dimensional point cloud, these points need to be projected onto a best fit plane.

The requirement of projecting points onto a plane limits the application to a specific type of point clouds, called 2.5D point clouds. A 2.5D point cloud is a data set in which all points projected along a given coordinate have no points laying below or above along the coordinate plane. Fig. 18 depicts the difference between a 2.5D and a 3D point cloud.
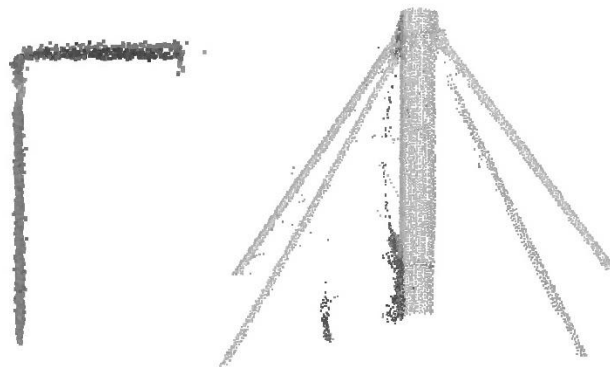
Figure 18 2.5D point cloud(left) and 3D point cloud(right)

This method is very sensitive to noise and outliers during the best fit plane definition. The method works well for reconstruction of large flat aeras like roofs, walls or facades of buildings. Considering the geometry and size of members of the steel lattice tower, the density and accuracy of required point cloud are not feasible to obtain using the current state of the art technology. Therefore, this approach is not possible to be utilized in this work.

Poisson Surface Reconstruction

The Surface Reconstruction is based on work titled 'Poisson Surface Reconstruction' [19]. The method allows to reconstruct a surface of the scanned object using the point cloud and relation between points' directional vectors (defined in 2.3.3) and gradient of indicator function χ . The indicator function χ is defined as an implicit function with values of 1 for points inside and values of 0 for points outside the objects volume. The gradient of the indicator function χ is a vector filed with non-zero values at points near the surface of the object. Fig. 19 depicts a two dimensional example of an indicator gradient vector field, an indicator function χ and a point cloud

With directional vectors of a 2D surface.

2D surface points with directional vectors | Indicator function | Indicator gradient
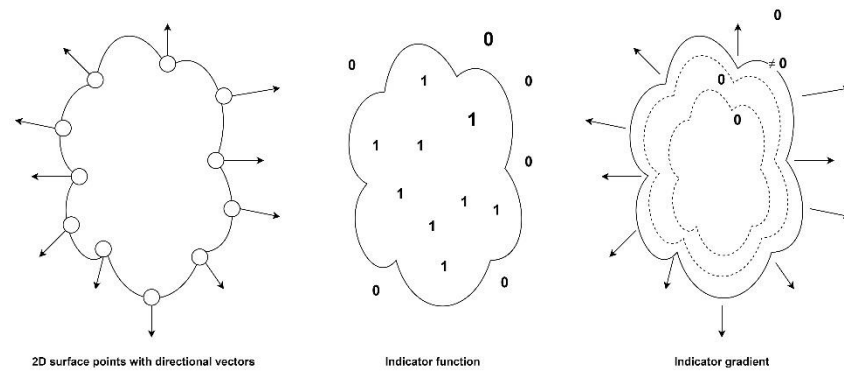
Figure 19 2d point cloud with directional vectors(left), Indicator function(center), Indicator gradient(right)

Defining the indicator function χ allows to find the surface of the scanned object by extracting the appropriate isosurface. The solution for the indicator function χ is found by solving the Poisson problem:

$$\Delta\chi = \nabla \cdot \nabla\chi = \nabla \cdot \vec{V}$$

The Laplacian of the indicator function χ equals to the directional vector field.
Similarly to Delaunay Triangulation, for this method both point cloud density and accuracy need to be of high quality. Based on requirements imposed by the size of members of the steel lattice tower the desired point cloud quality is not feasible to be obtained with the current state of the art technology. Due to this reason, Poisson Surface Reconstruction is not possible to be utilized in this work.

2.3.3   Methods relevant to the proposed approach

Methods introduced above work well for concrete or masonry structures. Large planes of walls, roofs and floor slabs are easy to reconstruct using one of the mentioned methods. For steel structures where the majority of structural components are steel profiles with small planes and complexity in shapes and orientations, a novel approach needs to be adopted. No explicit solution for steel lattice structures is currently published. For the approach proposed in this work, a number of relevant existing methods were used as the basis to define the methodology described in Section 3.5. All the relevant methods are introduced in this Section.

Segmentation

Segmentation is one of the key steps in point cloud processing. It allows to extract point clouds of simple objects (e.g. plane or individual members of the structure) from an entire, complex point clouds of the structure. This step can reduce complexity of the data processing from single members/ parts of the structure enabling to simplify our problem by transitioning our work from global to local member perspective. Segmentation can be divided into three main groups [20]:

- Model fitting
- Region growing
- Clustering

Model fitting

For model fitting segmentation methods, two common feature extraction algorithms are utilized- Hough Transform and RANSAC. All methods segment the data by detecting planes and geometrical shapes based on predefined search conditions similarly to shape fitting (Section 2.3.1). The only difference lies in its application, shape fitting focuses on generating the final digital model when model fitting segmentation allows to divide the point cloud into smaller Sections. Fig. 20 depicts a model fitting segmentation example.
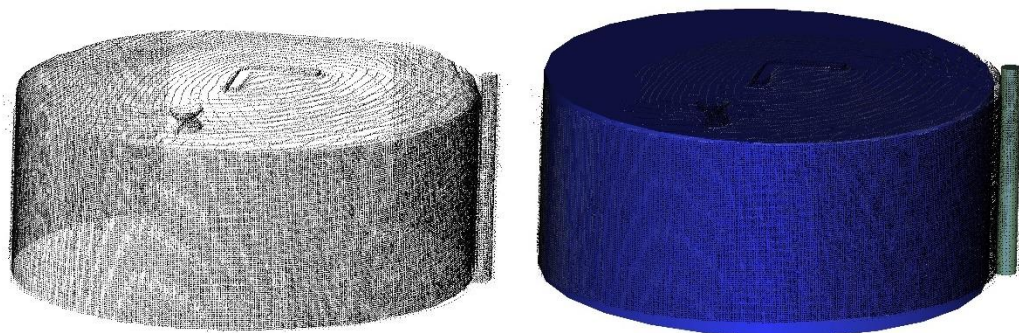
Figure 20 Model fitting segmentation

Its main application, concerns planes and simple geometrical shapes like cylindrical oil tanks. Similarly to shape fitting, model fitting segmentation methods face similar issues, which were sensitivity to point cloud data quality(density, noise and accuracy) and inability to work with complex structures. Therefore, model fitting methods are not a suited for steel lattice towers.

Region growing

Region growing is a popular segmentation algorithm utilized in digital image processing and very useful for point cloud data applications. It allows to subdivide the data into regions defined by specific features. Fig. 21 showcases a general algorithm for region growing.
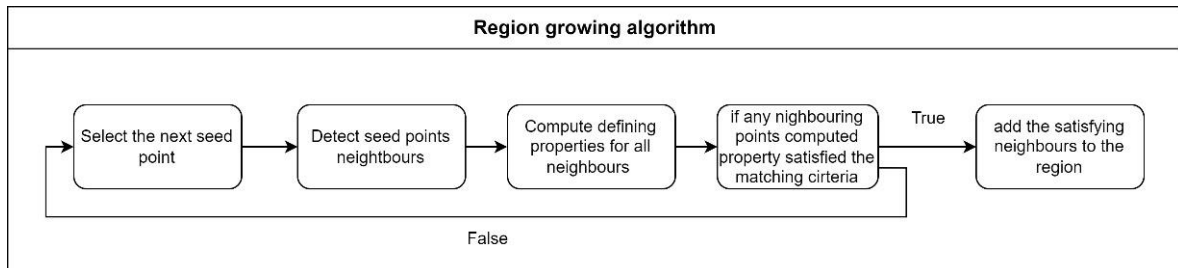
Figure 21 region growing algorithm

An example of the region growing applied to a point cloud data is depicted in Fig. 22.
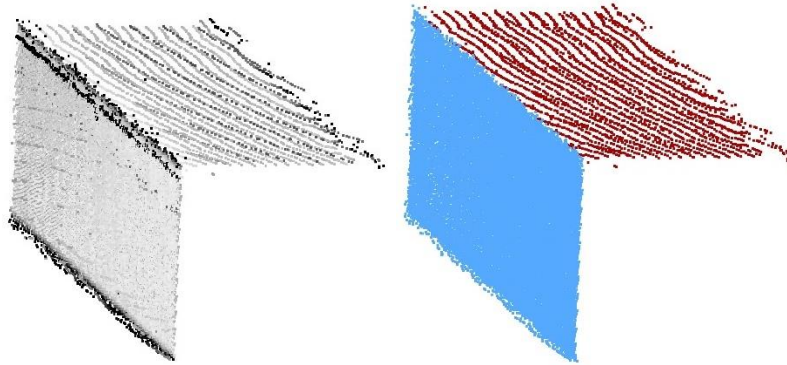
Figure 22 Region growing segmentation

The data in Fig. 22 is segmented based on the directional vectors of points, which represent a normal vector of the best fit plane of neighboring points. Applying region growing to the data presented in the example allows to divide points into two segments representing the flanges of the scanned L-shaped profile. Region growing segmentation is a very universal method applicable for different types of data.

Clustering

Clustering method focuses on grouping the point cloud into clusters using geometrical relation between all points in the data set. If points are concentrated in separate regions, a clustering segmentation can be applied to divide the point cloud to form sub-groups. An example of a clustering applied to a point cloud is depicted in Fig. 23.

Figure 23 Clustering of a point cloud

By grouping point clouds, the problem is simplified, enabling to locally focus on specific clusters. Additionally, all points within the cluster can now be globally represented by one point labeled as the center of our cluster.

In the approach proposed in this work both region growing and clustering segmentation methods will be utilized. Their application will be described in Section 3.5.2.

Extracting lines

Line extraction covers many topics in point cloud processing. It allows for an easy to interpret representation of the data, which can later be used for modeling purposes in CAD softwares. It can be divided into three main groups [20]:

- Point-based methods
- Plane-based methods
- Image-based methods

Point-based methods

Point based line extraction focus on segmenting edge points from the input point cloud using region based or model fitting segmentations described earlier. The edge points are later used to detect line segments using different line fitting methods [20]. An example of a point-based line extraction is depicted in Fig. 24.
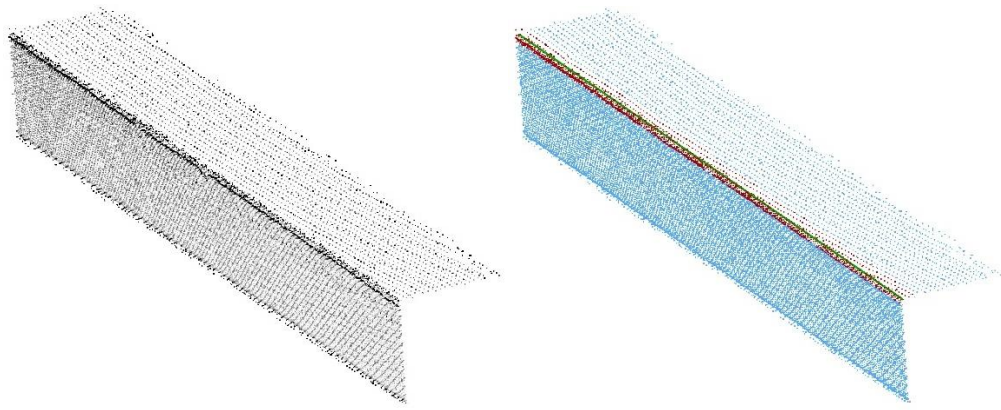
Figure 24 Point based line extraction

The disadvantage of point-based methods come from an edge point extraction step due to high sensitivity to noise and outliers. This can be minimized by filtering out outlier points prior to the process.

Plane-based methods

Plane-based methods detect lines as the intersection between two planes. Plane detection is the initial step for the process, any segmentation method described above can be used to find points representing a given plane. Afterwards, line segments are then detected for all the adjacent planes finalizing the process. An example of plane-based line extraction is depicted in Fig. 25.
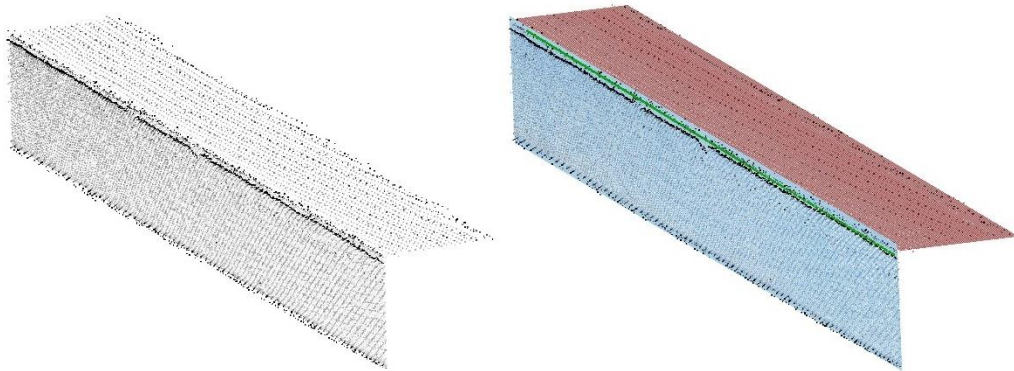
Figure 25 Plane based line extraction

This approach is limited to point clouds of structures with large planar dimensions like roofs or building facades. Therefore, the method applicability to steel lattice towers is limited considering size of analyzed L shaped members.

Image-based methods

Image-based line extraction transforms 3D point cloud into a 2D image by projecting the data onto a predefined plane and converts the points into pixels. Afterwards, image processing algorithms for line detection are utilized allowing to extract the line segments in the two dimensional environment which need to then be translated back into the three dimensional environment of the original data set. An example of image-based line extraction method is the application of Hough Transform for line detection presented in Section 2.2.5. Image-based methods are very diverse and robust, but requires pre-

processing of the analyzed point cloud data. In order to extract the line segments, the data set needs to be divided into cross-Sections and a projection plane has to be defined enabling clear view on the processed point cloud.

In the approach proposed in this work both point based and image based line extraction methods are utilized. More details of their implementation are described in Section 3.5.2.

2.4   Contribution to the state-of-the-art

What is the contribution of the geometrical model generation method proposed in this thesis to the current state-of-the-art? What are the main knowledge gaps which need to be covered? How the current state-of-the-art relates to the method proposed in this work? These among other questions will be addressed in this Section.

As stated in the previous Section, generating geometrical models of steel lattice structures based on point cloud data is not a commonly researched topic addressed within the state-of-the-art in the Civil Engineering filed. Although semi-automatic and automatic methods for geometrical model generation for steel lattice structures have been already investigated [34,35], the most popular methods are still based on manual processing of point cloud data [34]. The biggest disadvantage of manual based methods is the high demand on time required for the process and the quality of the produced CAD model which is solely dependent on the drafter. In order to minimize the human error and accelerate the model generation, semi-automatic methods have been developed. Amongst semi-automatic approaches utilized for model generation of lattice towers using point cloud data the majority focuses on model fitting methods [35]. The model fitting method presented in [34] uses a set of pre-generated lattice tower CAD models to which the point cloud is fitted to, based on the geometrical features extracted in the point cloud data. This method allows for an efficient geometrical reconstruction of lattice towers, assuming the analyzed structures geometry is standardized and exists in the pre-defined CAD model database. In cases where no prior information regarding the geometry of tower is known, the applicability of the method is deniable and might lead to inaccurate results. For those cases, automatic methods allowing to reconstruct the geometrical model of a lattice tower based on point cloud data with no prior tower geometry classification required. An example of this approach is given in [2], where the towers structural elements are discretized as system lines using a point cloud processing algorithm. The method presented in [2] allowed to obtain geometrical system line models with absolute accuracy of the line positioning in a range of 5cm. The accuracy is based on the root mean square error (RMSE) of the line fitted to the analyzed point cloud not the geometry of the structure. Therefore, the accuracy of the final geometrical model relative to the real geometry of the structure was not assessed. What is more, the cross-sectional position of the system line in the generated model is dependent on the point cloud distribution rather than the geometry of the structure.

Understanding the limitations of model generation methods using point cloud data available within the current state-of-the-art, a novel approach is being proposed in this thesis. The method defined in this study allows for an automatic geometrical model generation of a lattice structure without the need of manual processing and pre-definition of the analyzed tower geometry. Additionally, the positioning of system lines for structural members is based on the geometry of the analyzed lattice tower.

Based on the literature review performed for this study, the model generation method developed in this thesis proposes an innovative approach that has not been investigated yet.

Next chapter will present the methodology for the geometric model generation process developed for the purposes of this thesis, which leads to creation of geometrical CAD model utilized for the FEA covered in chapter 4 of this work.
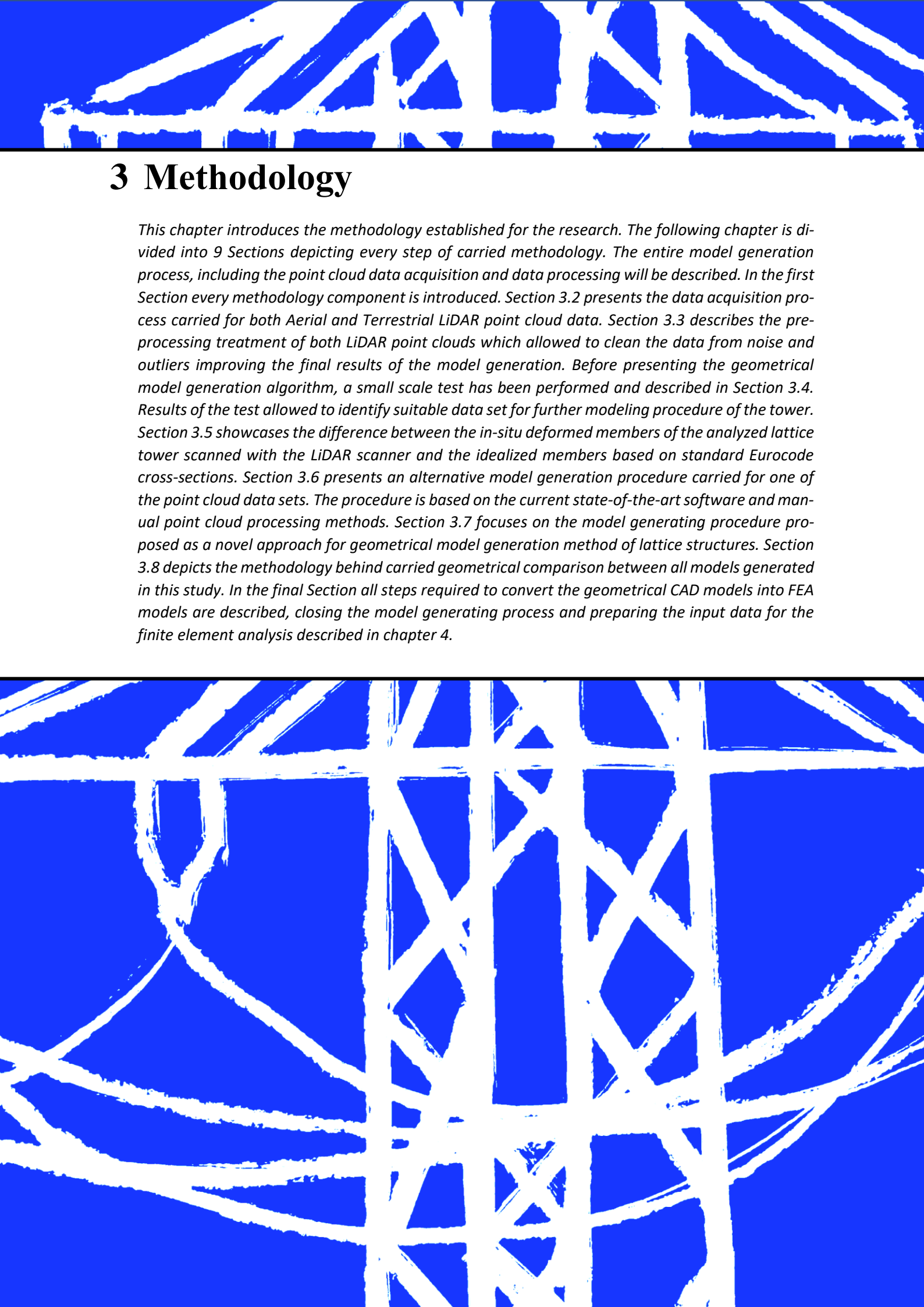
3 Methodology

This chapter introduces the methodology established for the research. The following chapter is divided into 9 Sections depicting every step of carried methodology. The entire model generation process, including the point cloud data acquisition and data processing will be described. In the first Section every methodology component is introduced. Section 3.2 presents the data acquisition process carried for both Aerial and Terrestrial LiDAR point cloud data. Section 3.3 describes the pre-processing treatment of both LiDAR point clouds which allowed to clean the data from noise and outliers improving the final results of the model generation. Before presenting the geometrical model generation algorithm, a small scale test has been performed and described in Section 3.4. Results of the test allowed to identify suitable data set for further modeling procedure of the tower. Section 3.5 showcases the difference between the in-situ deformed members of the analyzed lattice tower scanned with the LiDAR scanner and the idealized members based on standard Eurocode cross-sections. Section 3.6 presents an alternative model generation procedure carried for one of the point cloud data sets. The procedure is based on the current state-of-the-art software and manual point cloud processing methods. Section 3.7 focuses on the model generating procedure proposed as a novel approach for geometrical model generation method of lattice structures. Section 3.8 depicts the methodology behind carried geometrical comparison between all models generated in this study. In the final Section all steps required to convert the geometrical CAD models into FEA models are described, closing the model generating process and preparing the input data for the finite element analysis described in chapter 4.

3.1 Methodology

This Section presents an overall workflow of 3D geometric model generation of a lattice tower from a point cloud, which consists of three main steps:
- Data acquisition
- Handling the point cloud data
- Geometrical modeling

steps carried out during the method proposed in this thesis are given in a schematized overview in Fig. 26.
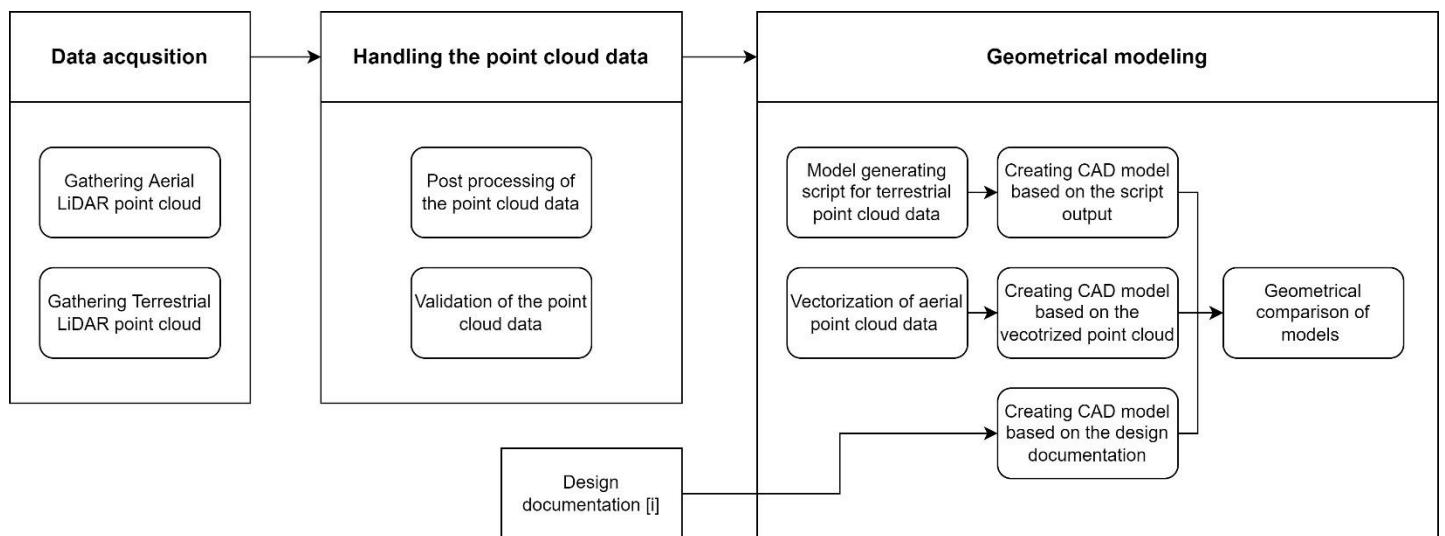
Figure 26 Methodology

The application of the developed approach will focus on analyzing only the bottom part of the steel lattice tower, from the ground up to a height of 27m, as marked in Fig. 27.
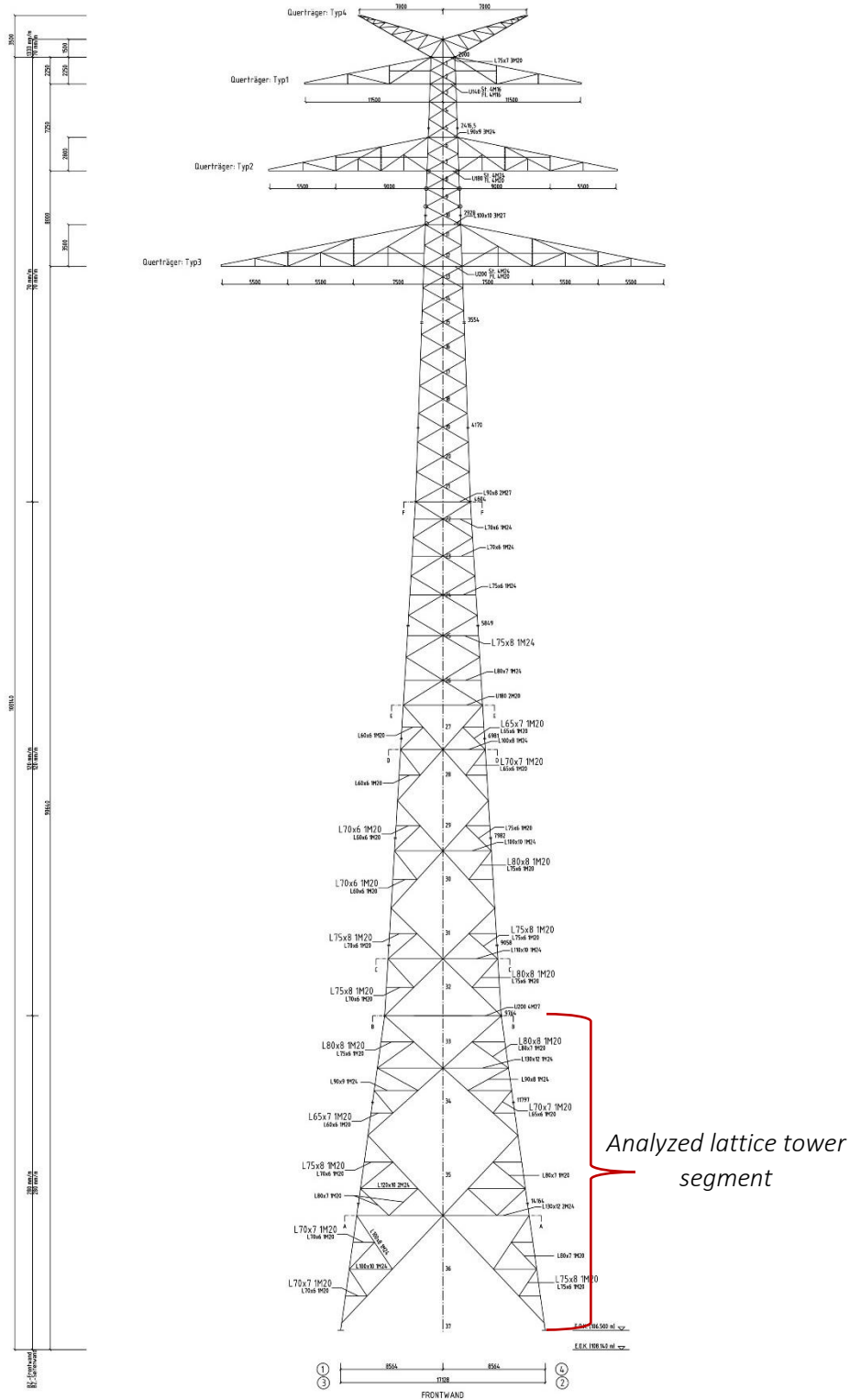
Figure 27 Analyzed lattice tower segment

Considering the repetitive geometry of the lattice tower segments, limiting the geometrical model generation to a specific part of the structure allowed to answer the research questions without the need to create and analyze the entire tower. The main purpose of this study is to investigate if point cloud data can be used for digital reconstruction of lattice structures for structural

engineering applications. The selected part of the structure depicts all types of possible members used in the tower (labeled in Fig. 28):

- vertical members,
- horizontal bracings,
- diagonals.
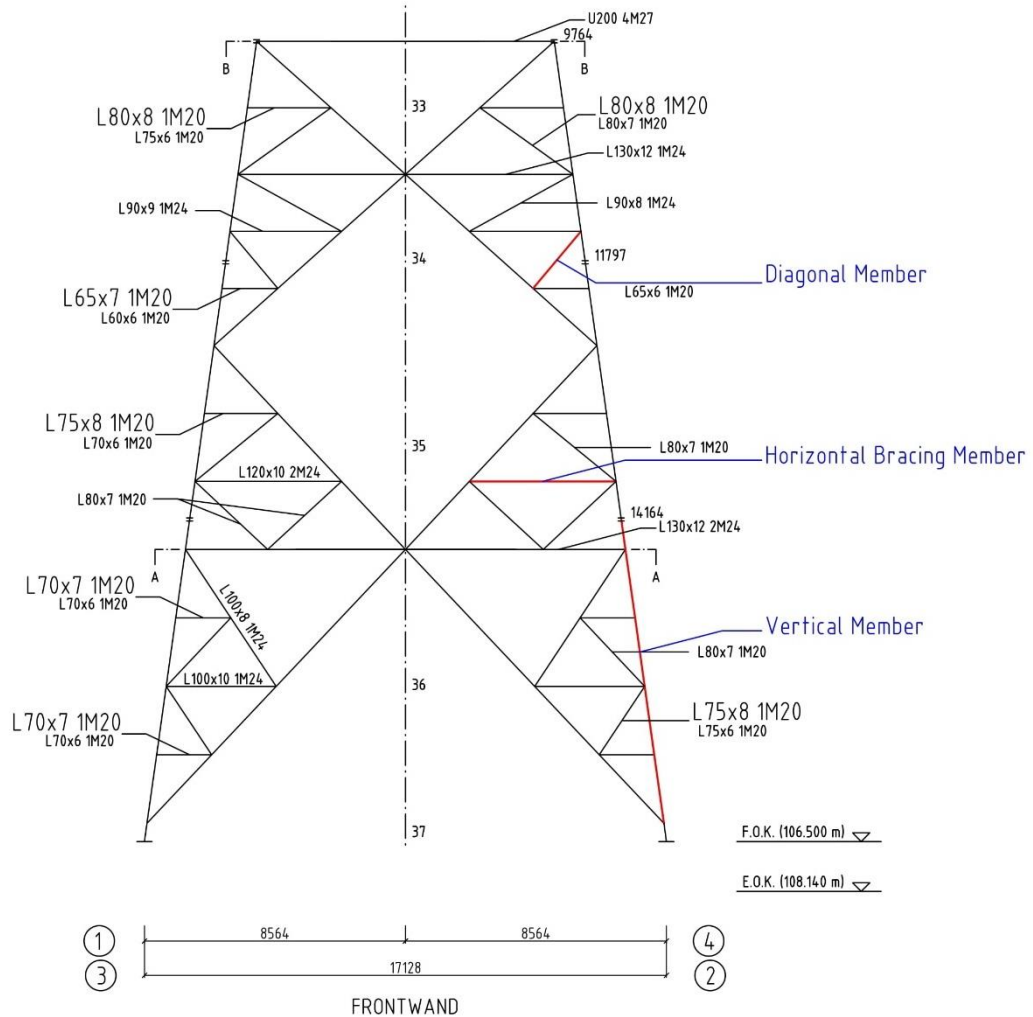
Figure 28 Analyzed lattice tower segment with highlighted member types

Additionally, by analyzing only the lower part of the tower, the data acquisition process for terrestrial LiDAR data was simplified and allowed to avoid the issue of non-uniform point cloud density along the height of the structure mentioned in Section 2.1.4.

Data acquisition

At the beginning of the study LiDAR point clouds were gathered using two available technologies defined in Section 2.1. The data acquisition process is described in Section 3.1, showcasing the hardware specifications and output point cloud parameters with a visual representation of both data sets.

Handling the point cloud

In order to improve the quality of the data, post processing algorithms were implemented for both point clouds allowing to clear outliers and large noise issue. Furthermore, the quality of both point clouds was validated in terms of accuracy, noise level and coverage. The validation was conducted for a set of point cloud clusters of isolated members.

Geometrical modeling

In the final step both data types were used to generate geometrical model using two different approaches. The first approach, using manual line extraction methods was applied to the aerial LiDAR data. The manual method represents a solution achievable within the current state of art software. In the second method, terrestrial LiDAR data was used as the input for the script developed during the Thesis showcasing a novel approach to the problem.

Afterwards, both geometrical models are compared to a reference model based on design documentation which allows to answer the first research question:

'*Does LiDAR point cloud data acquired by an aerial/terrestrial scanner provide sufficient geometric information to create an accurate 3D geometric model for FEM application*'.

The further part of the study was continued with the terrestrial LiDAR data of which the geometrical model was used as the basis for the finite element model defined in Section 4.

3.2   Data acquisition

A lattice tower located close to the city of Bremen, Germany was selected to capture topographic information for this study, Fig. 29. The tower was built in 1979, has a design height of 110 meters and stands next to the river "Weser".
The tower located in the free space area, which enabled to collect the data with highest possible accuracy, and high data coverage. The quality of the point cloud is a very important aspect during data treatment. The level of precision of the final geometrical model will be directly related to the initial quality of the point cloud.

Figure 29 Analyzed lattice tower location.

UTM 32: 53.123217, 8.669695

Considering pros and cons of both available LiDAR acquisition techniques acknowledged in Section 2.1, choosing between one of them before acquiring the data could lead to a wrong decision which would have an impact on final expected results. Therefore, both techniques were used so that acquired point clouds could be compared and the geometrical model generating approach proposed in this work could be applied to a more suitable data set.

3.2.1   Aerial LiDAR point cloud

The aerial data was the first point cloud to be acquired. The data collection took place in September 2019 and was conducted prior to the start of the work on the thesis, therefore the entire structure was scanned. The point cloud was collected by Swiss company- Aeroscout. The technology used for gathering the data was a Riegl VOX1 LiDAR scanner mounted on an UAV drone. The specification of the hardware is given in Tab. 1.

Maximum measurement range	up to 920m
Max. Operating Flight Altitude AGL	350 m
Max. Operating Flight Altitude AGL at 550 kHz	110 m
Minimum range	5 m
Accuracy	25 mm
Precision	25 mm
Beam divergence	0.5 mrad
Scan angle range	330°
Scan speed	200 scans/sec

Table 1 Riegl VOX1 LiDAR specification

Fig. 30 depicts the UAV drone with the scanner.

Figure 30 UAV drone with Riegl VOX1 LiDAR scanner

An important aspect of aerial LiDAR scanning is to establish the flight path of the drone allowing for a good data collection from all sides of the structure at the same time satisfying all the safety measures while working around high voltage. The established flight path during scanning of the lattice tower is depicted in Fig. 31.
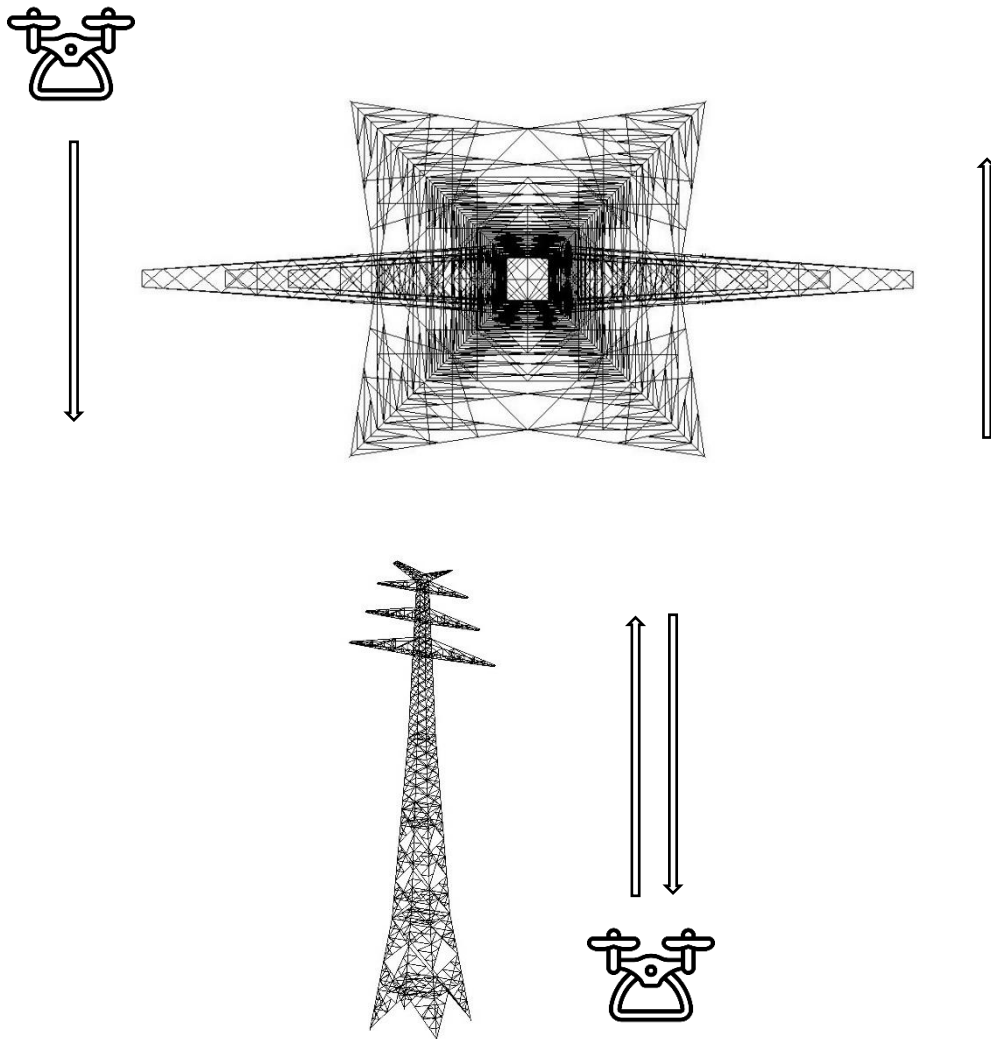
Figure 31 Data acquisition flight path

The safety measures for works around high voltage power lines were based on minimum air clearances specified in EN50431-1 [21], where different values are provided within Tables xx in Section 5.9. As a precaution, the UAV drone stayed minimum 5 meters away from the powerlines and never flew below them. The average distance of the UAV drone from the scanned tower was in a range of approximately 1.5m to 2.0m. Such a distance allows to collect the data with accuracy of 1cm according to the specification of the Riegl scanner, Tab. 1.

The density of the point cloud is related to the scanning time and the distance of the object to the device. The density of the point cloud collected for the purpose of this study is estimated as 800 ppm^2 (points per meter square), which is a relatively high density for an aerial LiDAR data.

The resulting aerial LiDAR point cloud is depicted in Fig. 32.
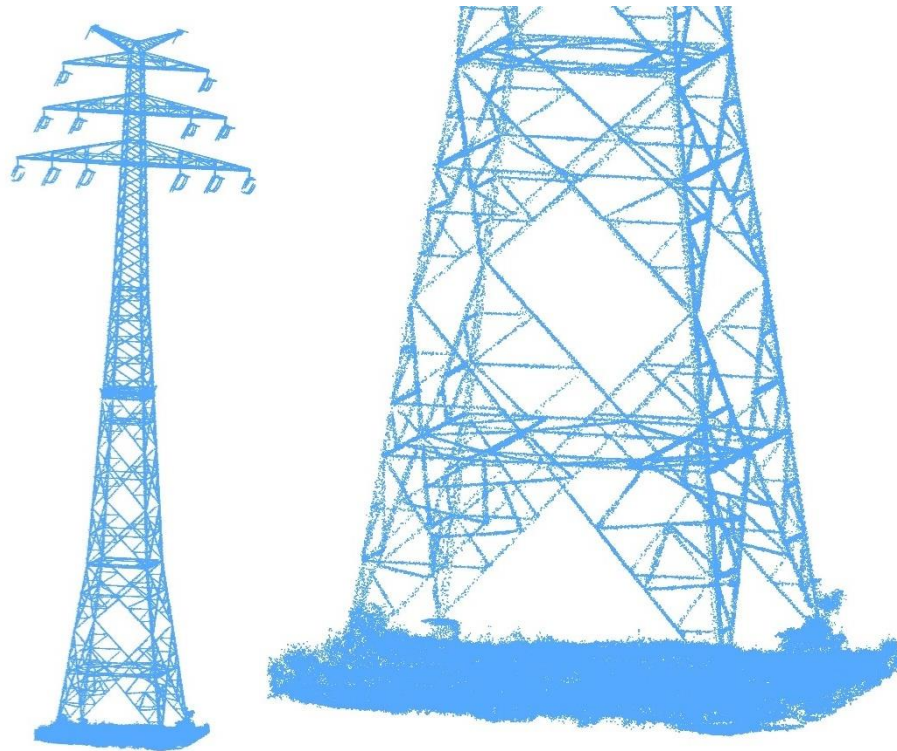
Figure 32 Aerial LiDAR point cloud

For the acquired aerial LiDAR data 870 462 points were collected.

3.2.2   Terrestrial LiDAR point cloud

The terrestrial LiDAR point cloud was gathered in September 2020, as opposed to the aerial LiDAR data only the analyzed lower part of the tower was scanned. The data acquisition was conducted by the LSA (Laser scanning architecture), a German company specialized in terrestrial laser scanning. Similarly to the aerial LiDAR point cloud, Riegl scanner was used to capture the data. The terrestrial model Riegl VZ400i specification is provided in Tab. 2.

Maximum measurement range	up to 400m
Minimum range	1.5 m
Accuracy	5 mm
Precision	3 mm
Beam divergence	0.35 mrad
Scan angle range	100°
Scan speed	240 scans/sec

Table 2 Riegl VZ 400i specification

The scanner is depicted in Fig. 33.

Figure 33 Riegl VZ 400i terrestrial LiDAR scanner

Contrary to the aerial method terrestrial laser scanning allows to gather the data from a safe distance sufficing all the minimum air clearances specified in EN50431-1 [23]. Therefore no additional safety measures needed to be taken while acquiring the data.

The final point cloud of the tower was a combination of four different scanning stations, in which the scanning positions of these points is shown in Fig. 34. In order to enable for a good alignment of the four point clouds collected from different scanning stations, an overlap between the scans is required. For the lattice tower investigated in the thesis an overlap of 50% was assumed, as shown in Fig. 34.
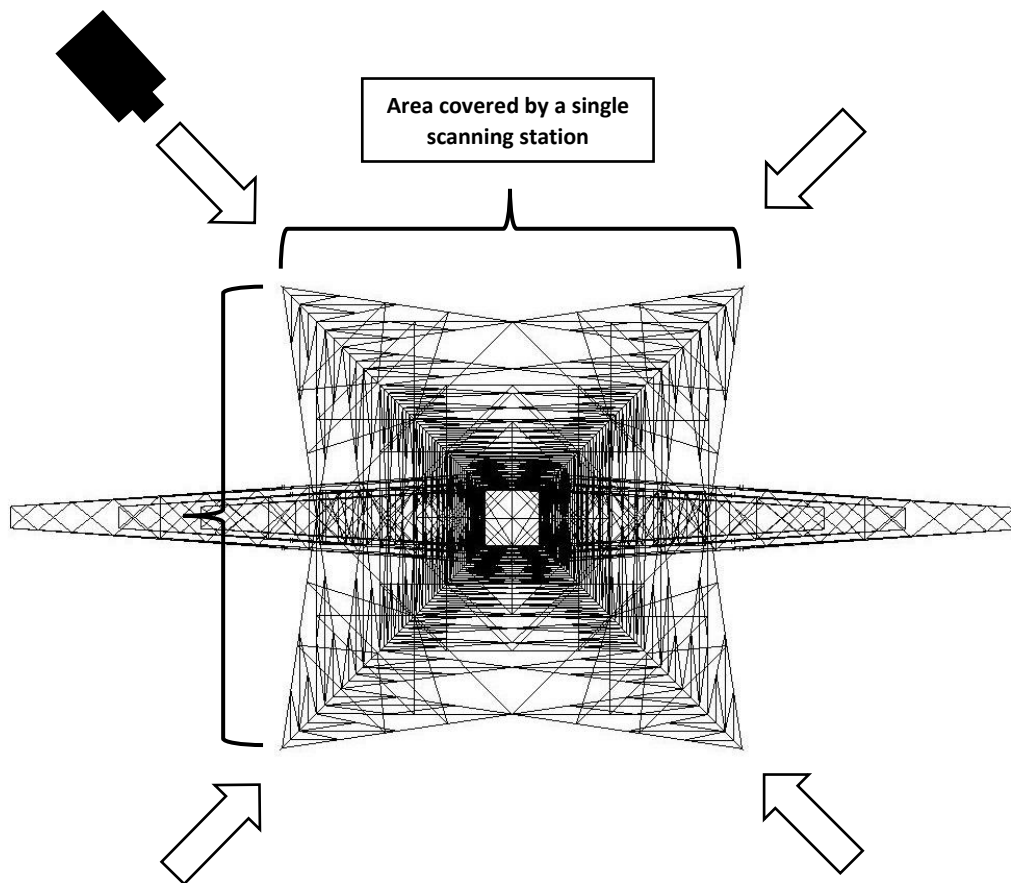
Figure 34 Terrestrial LiDAR data acquisition plan

With the assumed data collection distance and overlap, an accuracy of 0.5cm was achievable according to specification of the Riegl VZ400i scanner. Fig. 35 shows the point cloud of the tower after registering data points from 4 scanning station.
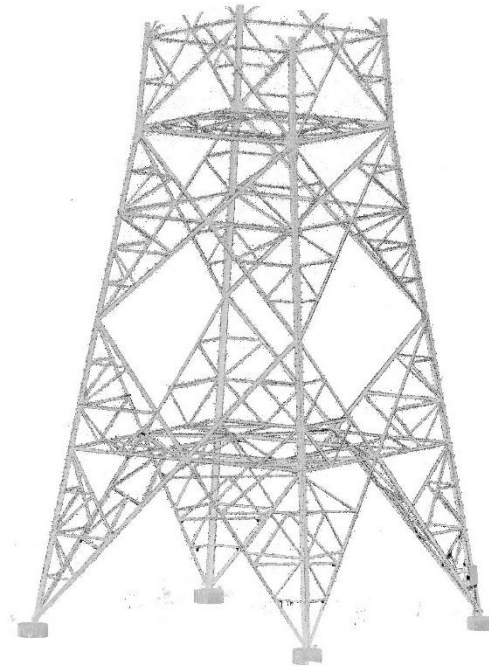
Figure 35 Terrestrial LiDAR point cloud of the analyzed lattice tower segment

For the acquired terrestrial LiDAR data 24 382 955 points were collected.

3.3 Pre-processing of the point cloud data

Before validating the quality of point clouds, both data sets were cleaned from large noise and outliers which improved their overall quality. This stage used two basic pre-processing algorithms described in Section 2.2.

The initial step used one of the properties of the LiDAR point cloud which is the intensity value. For such Riegl sensors, the intensity value is expressed in a grayscale range of 1 to 256, in which 1 defines a total absence of point (black) and 256 represents the highest possible return value of the laser beam (white). The intensity value is not only depended on the reflectivity of the scanned object but also the scan angle at which the laser beam hits the surface meaning that the same material will have a higher intensity on a plain surface compared to the edges. This feature allows to remove the noisy data visible near the edges of scanned L shaped profiles, portrayed in Fig. 36.
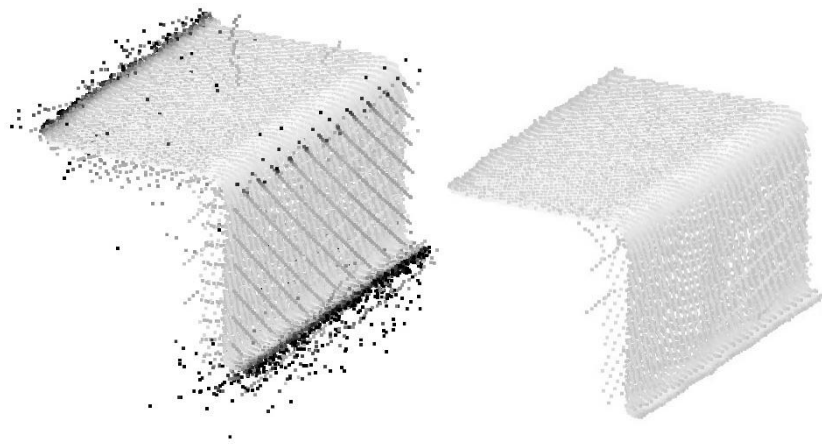
Figure 36 Intensity filtering

Similar issue is apparent in the connection regions, where noise points with low intensity values are present Fig. 37.
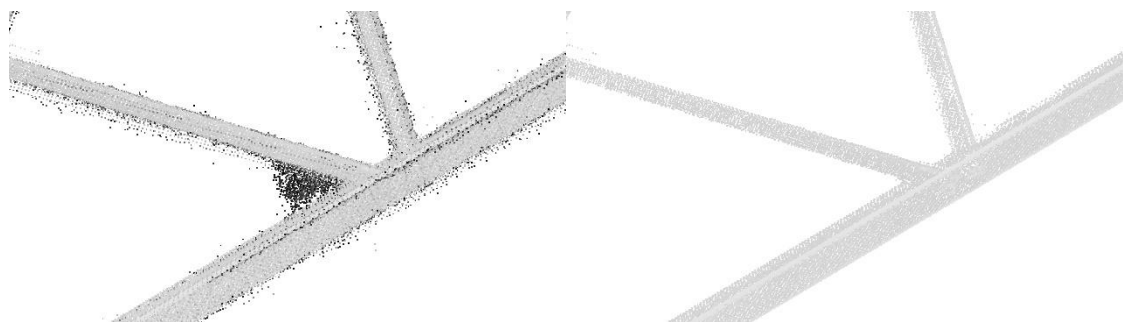
Figure 37 Intensity filtering in connection region

By introducing the minimum threshold all points with low intensity values are filtered out for both data sets, an intensity value of 190 has been assumed.

Figures below depict both point cloud before and after intensity filtering, Fig. 38, 39.
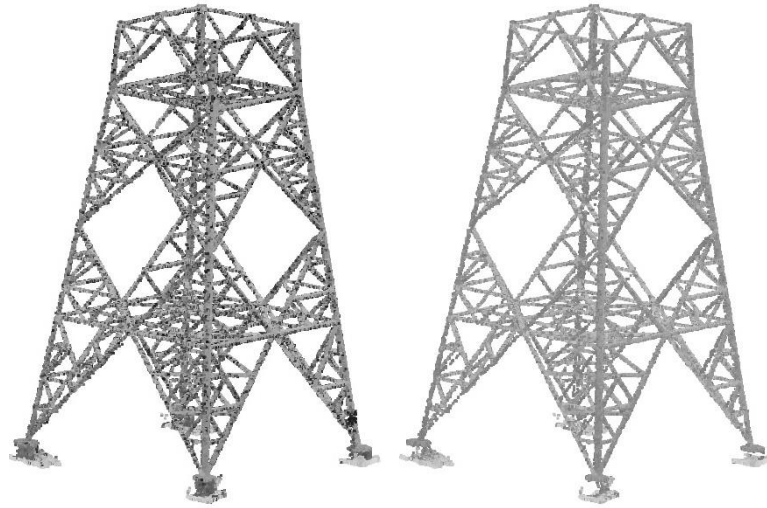
Figure 38 Intensity filtering applied to the Aerial LiDAR point cloud.

Unfiltered data with noise points in dark grey (left), filtered data (right).
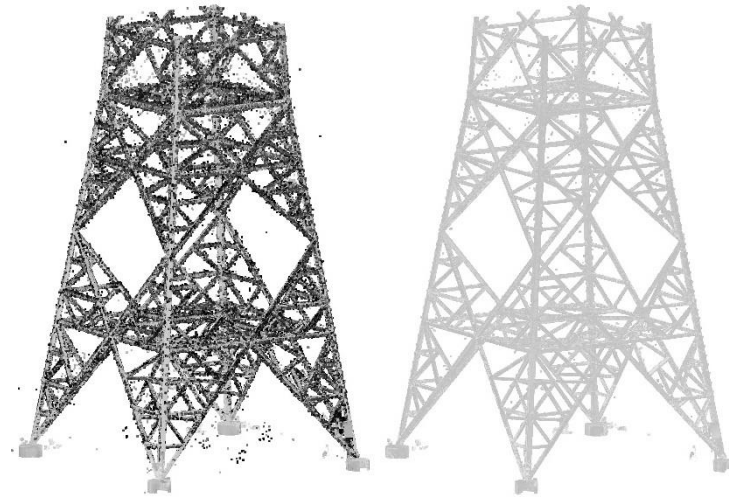
Figure 39 Intensity filtering applied to the Terrestrial LiDAR point cloud.

Unfiltered data with noise points in dark grey (left), filtered data (right).

After filtering out points based on their intensity, a nearest neighbor search(KNN) algorithm was utilized to remove the leftover outliers from both point clouds. The functional principle of the algorithm was to identify for each query point in the point cloud neighboring points in a spherical region with a predefined diameter. Points with no neighbors in the defined region occurred were treated as outliers and filtered out from the point cloud. A visual explanation is presented in Fig. 40.
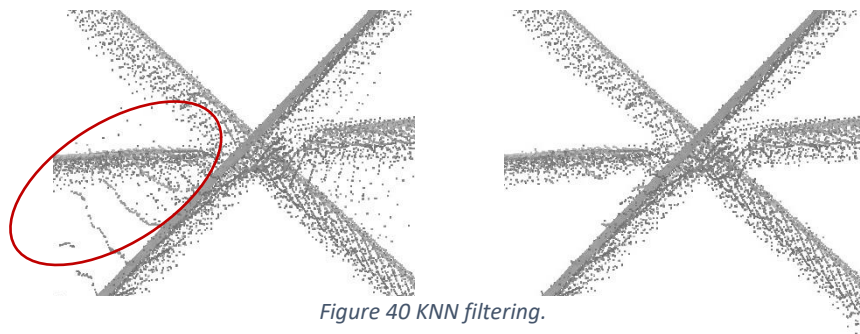
Figure 40 KNN filtering.

Unfiltered data with noise points in dark grey (left), filtered data (right).

The region diameters values were different for both data sets. The dimension was based on the accuracy provided in the hardware specification (Tab. 1 & 2). The threshold diameter ***d*** for the search region was assumed as ***d***=2* point cloud accuracy, which for both data types differed.

- The aerial LiDAR data region diameter was set as d_{aerial}=2cm
- The terrestrial LiDAR data region diameter was set as $d_{terrestrial}$=1cm

Figures below depict both point clouds before and after KNN filtering, Fig. 41, 42.
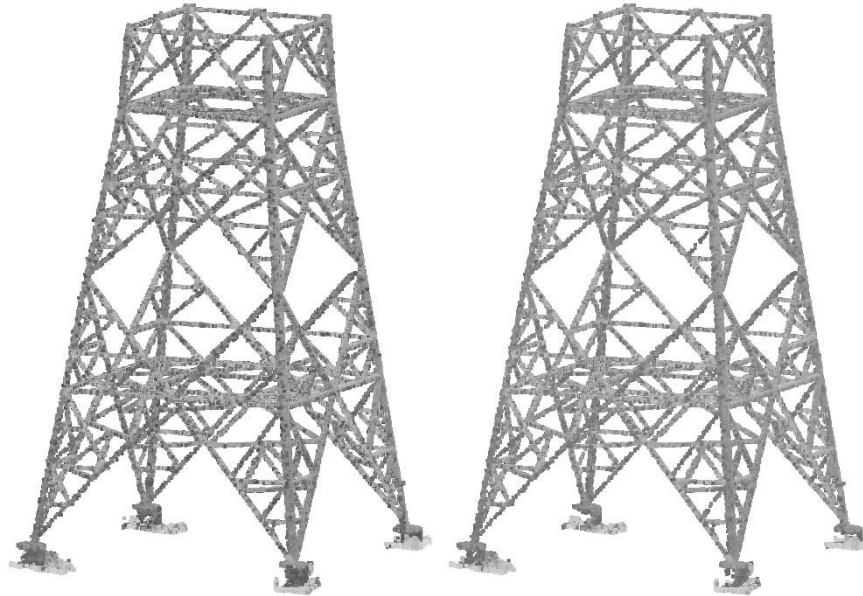
Figure 41 KNN filtering applied to the Aerial LiDAR point cloud.

Unfiltered data with noise points in dark grey (left), filtered data (right).
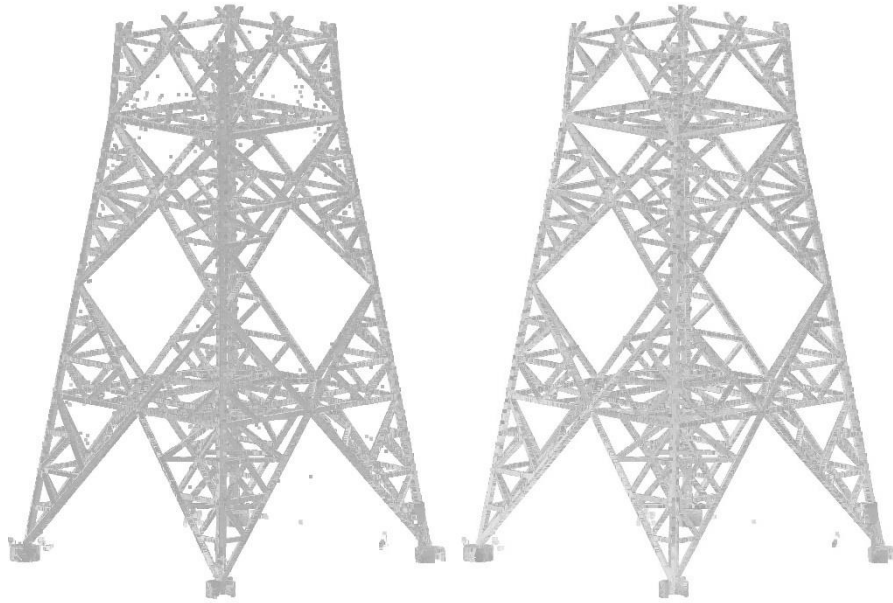
Figure 42 KNN filtering applied to the Terrestrial LiDAR point cloud.

Unfiltered data with noise points in dark grey (left), filtered data (right).

After the post processing stage:

- 15 % of the points in the aerial LiDAR data were filtered out
- 21 % of the points in the terrestrial LiDAR data were filtered out

Applying the filters allowed to improve the overall quality of both data sets and remove points which would cause problems during the model generation stage described in next Sections. The percentile value of points filtered during pre-processing is larger for the TLS data compared to ALS data which could be caused by registration issues presented in Fig. 8.

At this stage no additional pre-processing was introduced to the point clouds, therefore a comparison of both data sets could be performed.

Next Section focuses on the small scale testing of both filtered point clouds allowing to investigate locally, on a member level, which point cloud will be utilized for the model generating approach proposed in the thesis.

3.4   Small scale testing of both LiDAR data sets

A preliminary small scale testing has been performed based on data points of individual member extracted from both data sets to investigate which data set fits better to the method proposed in the thesis. The extracted members were tested on the line generation algorithm, which is a part of the developed geometric model generating script introduced in Section 3.6.

The workflow of the small scale testing is presented in Fig. 43.
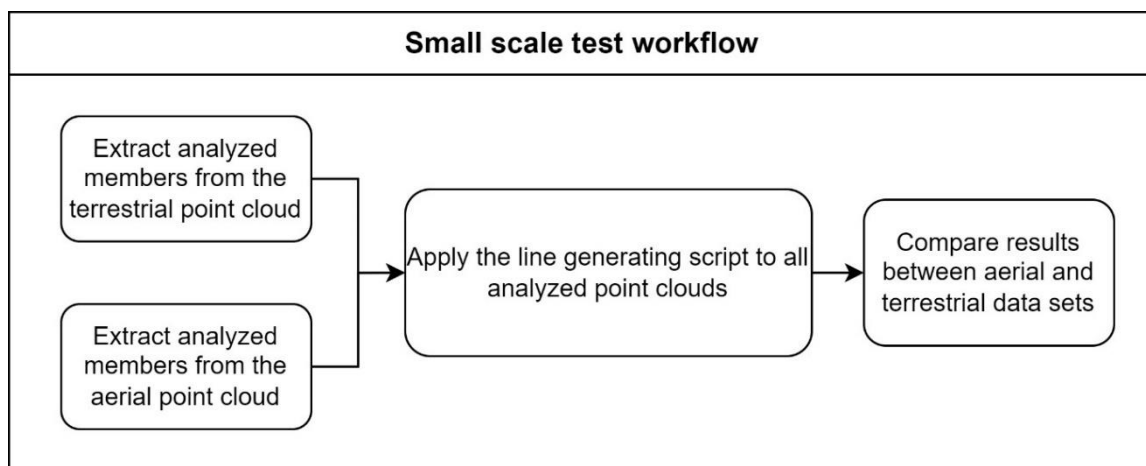
Figure 43 Small scale test workflow

3.4.1   Extraction of analyzed members

The analyzed members were chosen based on the cross-sectional dimensions. Considering the difficulty of the data acquisition increases the smaller the object is, the smallest profiles were investigated allowing to assure the comparison was performed on the critical members in terms of possible scanning issues.

In the analyzed lattice tower segment all utilized cross-sections are L-shaped steel profiles ranging from 60mm up to 250mm flange height. The smallest 60x6mm L profiles were used for diagonals at top part of the analyzed lattice tower segment, as shown in Fig. 44.
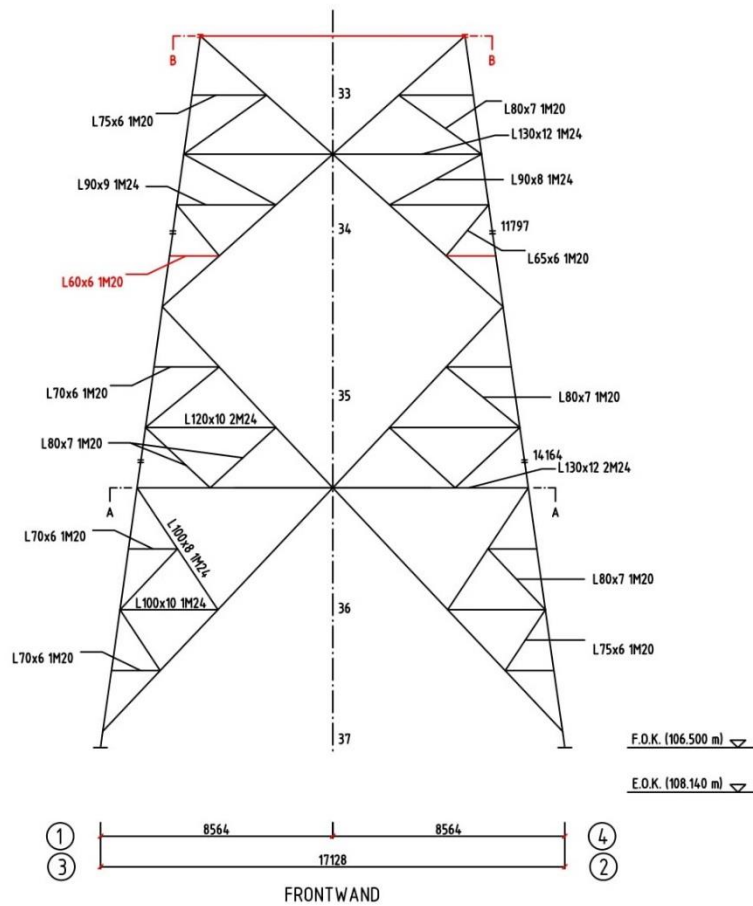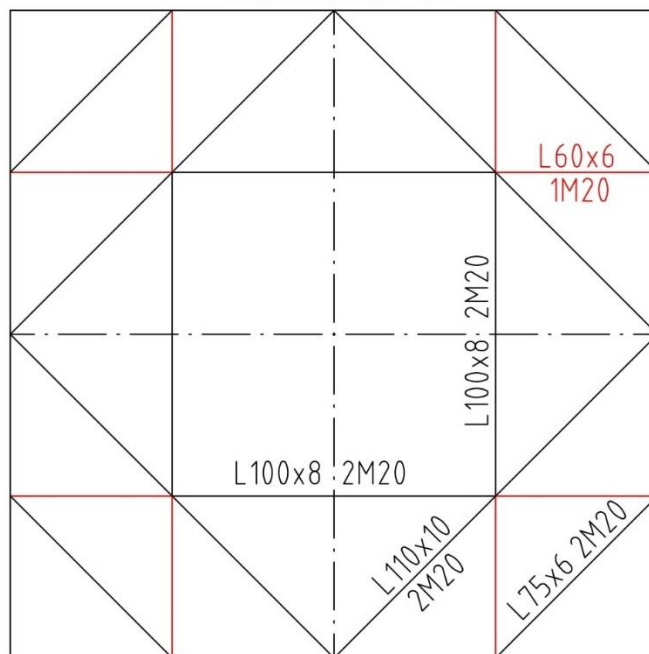
Figure 44 Analyzed lattice tower segment with highlighted L60x6 members

The dimensions of the standard L60x6 profile according to [22] are depicted in Tab. 3.

b = 60 mm	A = 690.9 mm^2
t = 6 mm	G = 5.423 kg.m^{-1}
r_1 = 8 mm	A_L = 0.2331 m^2.m^{-1}
r_2 = 4 mm	v = 42.4 mm
y_s = 16.9 mm	u_1 = 23.9 mm
y'_s = 43.1 mm	u_2 = 21.1 mm

Table 3 L60x6 dimensions
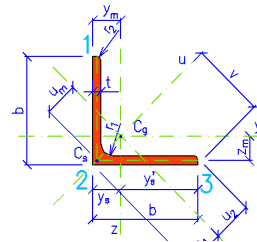
Figure 45 L cross-section

Fig. 46 depict the manually extracted point clouds of all L60x6 members for both the terrestrial and the aerial LiDAR data sets.
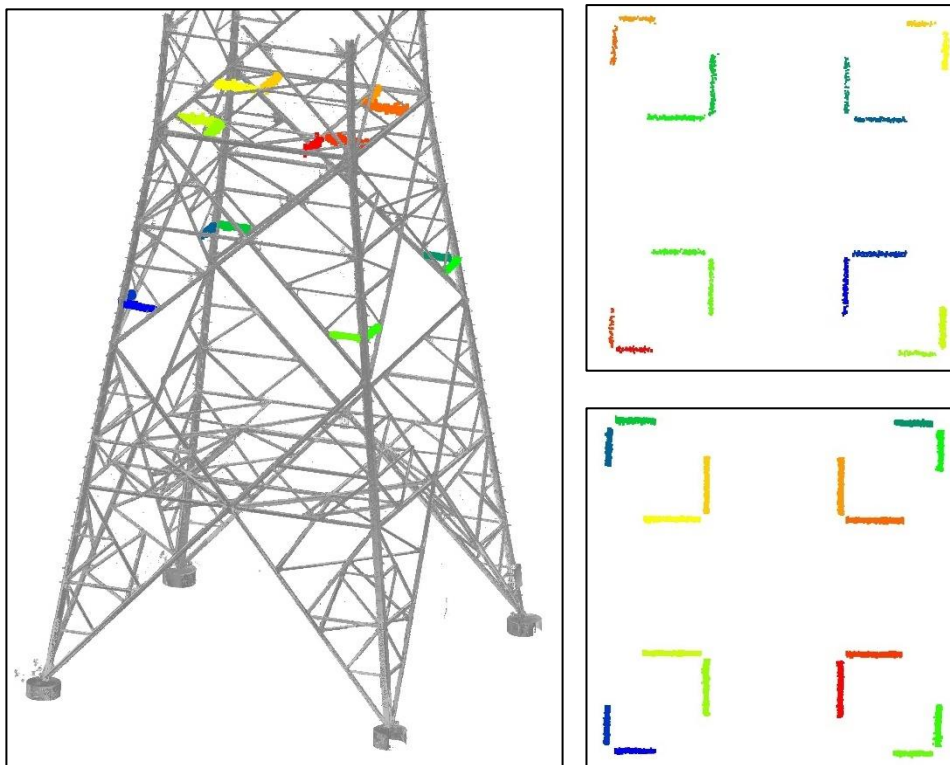
Figure 46 Highlighted L60x6 members in the analyzed lattice tower segment, Aerial data (top right),

Terrestrial data (bottom right)

After extracting point clouds of these members, the line generating script was applied to them.

3.4.2 Line generating algorithm

The introduced algorithm is one of the components of the geometrical model generating script developed for the purpose of this study. In this Section, the algorithm behind the script will be explained on an example of its application for the small scale test for both aerial and terrestrial LiDAR data sets.

The methodology for the line generating algorithm is inspired by the work of Laefer and Truong-Hong titled 'Toward automatic generation of 3D steel structures for building information modelling' [23]. In the research 3D models of I shaped steel girders are generated using a terrestrial laser scan point cloud.

The case investigated in the thesis focuses on a similar problem, a creation of a beam model using steel profile extrusion defined with geometrical features measured from extracted cross-sections of the analyzed point cloud data. However, the steps utilized in this study differ from the approach proposed in

[23]. The line detection, where Hough transform instead of KDE(Kernel density estimation) is being used to detect the geometrical features of the steel profile.

Considering the difference of the point cloud quality acquired in a laboratory controlled environment and the in-situ collected data of the analyzed lattice tower, a precise thickness measurement was not achievable with the analyzed data. Therefore, the proposed approach is limiting members' detection to defining the position of the longitudinal axis at the L shaped profile. The line generation algorithm is presented in Fig. 47. the line generating script consists of 6 steps, using the point cloud of the isolated member as the input data while outputting a line representing the longitudinal line along the corner points where two flanges meet. All steps defined in the algorithm are explained below on a L60x6 isolated member example
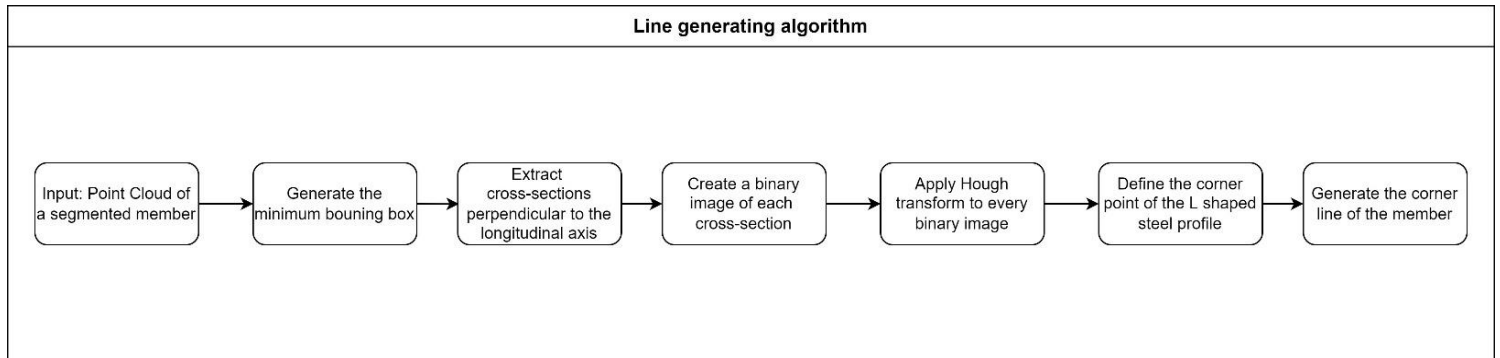
Figure 47 Line generation algorithm

Estimate the minimum bounding box for an isolated member

In the first step, a 3D minimum bounding box enclosing all points of the member is created, Fig. 48. It enables to define the local coordinate system of the member, in which three unit vectors of a local Cartesian coordinate system are defined three directions of the member. The vector along the longest edge is the longitudinal vector of the member.
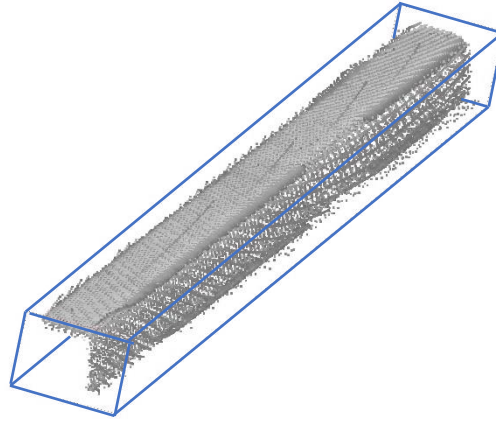
Figure 48 Minimum bounding box for the isolated member

Extracting cross-Sections perpendicular to the main longitudinal axis

Afterwards, cross-sections perpendicular to the longitudinal vector are equally extracted from the point cloud. The number and thickness of those cross-sections can be adjusted depending on the quality/quantity of the point cloud data. In order to standardize the results for the small-scale testing for both data sets, the cross-section parameters were fitted to the lower quality aerial point cloud. The distance between each cross-section has been set equally along the longitudinal direction of the member. Taking into account a lower point cloud density of the aerial data, the distance between each Section was set to 30mm for both data sets. Due to a non-uniform distribution of the point cloud, every cross-section has a depth dimension, enabling to increase the number of points collected for each cross-section. In the small-scale test, the depth of the cross-section has been assumed as 15mm. The example of extracted cross-sections of the member from a terrestrial point cloud data are depicted in Fig. 49.
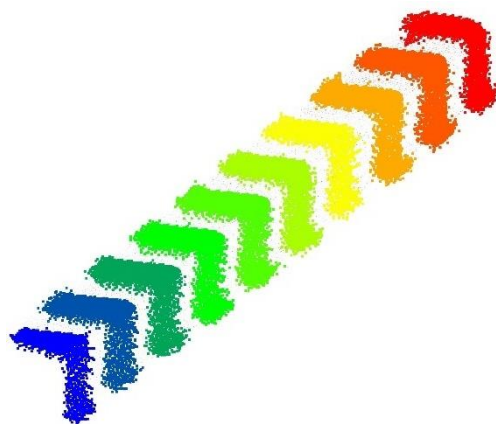
Figure 49 Point cloud cross-sectional segments perpendicular to the main longitudinal axis

Create a binary image of each cross-section

To extract edges of the cross-Section using Hough transform, the point cloud of the cross-section has been converted into images. For this task, all points of the cross-Section are projected onto a 2D plane located in the middle of the depth of the cross-section. Afterwards, a conversion to a binary image, with the resolution equal to the dimension of the minimum bounding box of the cross-section, is performed and visualized in Fig. 50.

Figure 50 Binary image of a cross-section

Apply Hough transform to every binary image

Hough transform is used to detect lines representing edges of the flanges of the L shaped profile based on binary images. The Hough transform is applied in the θ and ρ parametric domain defined by equation $\rho = x * cos\theta + y * sin\theta$, described in Section 2.2.5, Fig. 51.

.
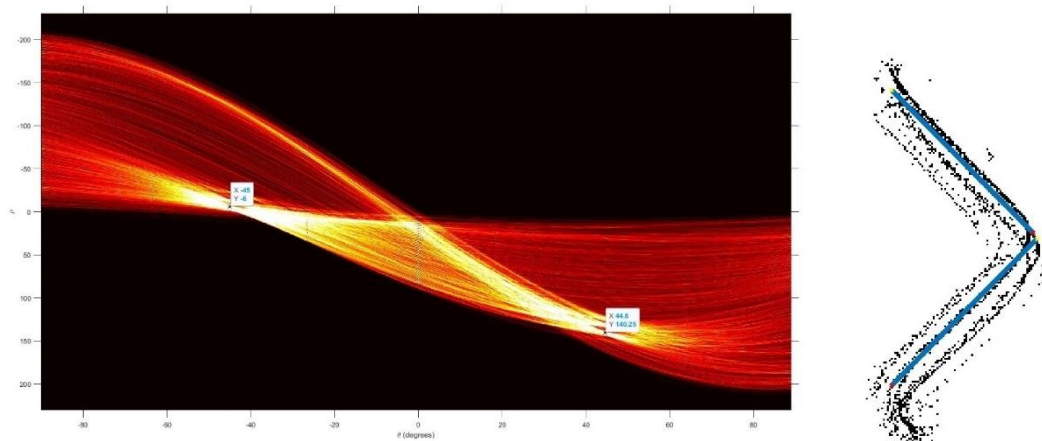
Figure 51 Hough transform line detection, parametric θ, ρ domain (left),

binary 2d domain (right)

Two peaks detected in the parametric domain represent the lines detected in the binary 2d domain.

Defining the corner point of the L shaped steel profile

After defining the lines representing the edges of flanges, an intersection point between them is computed, for the purpose of this study defined as the corner point of the L shaped profile, Fig. 52.
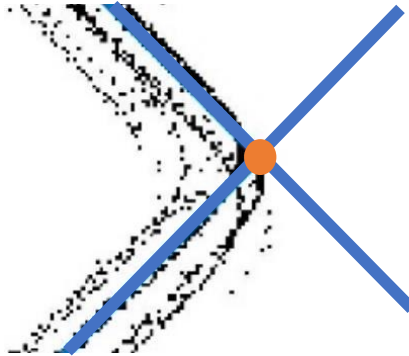
Figure 52 Corner point definition

Generating the corner line of the member

For all detected corner points a regression function is fitted, defining the longitudinal shape of the member. In the small-scale test, a linear regression has been assumed, considering all investigated members as straight during the data acquisition. The assumption on the members' straightness is based on the limitation of measurable deformation. The accuracy of the aerial point cloud is defined as 1cm, implying deformations below 1cm are not reliably captured with the aerial point cloud. Fig. 53 depicts line fitted to corner points generated by the script overlapped with the original scan.
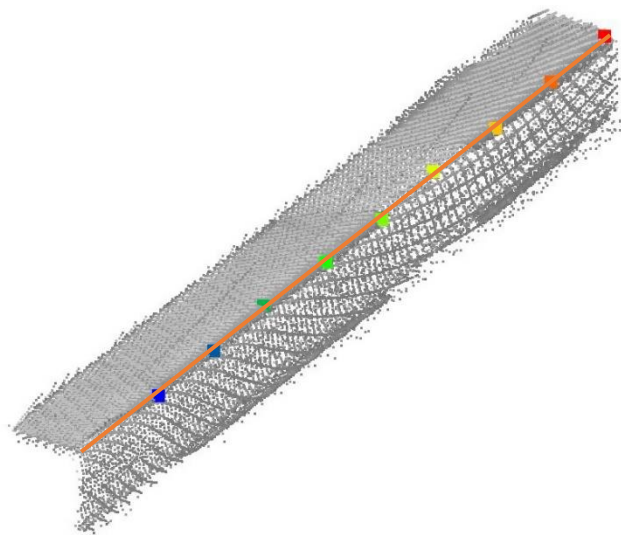
Figure 53 Corner line definition

3.4.3 Comparison of results

The output of the algorithm are corner points for every analyzed member for both data sets, as shown in Fig. 54.
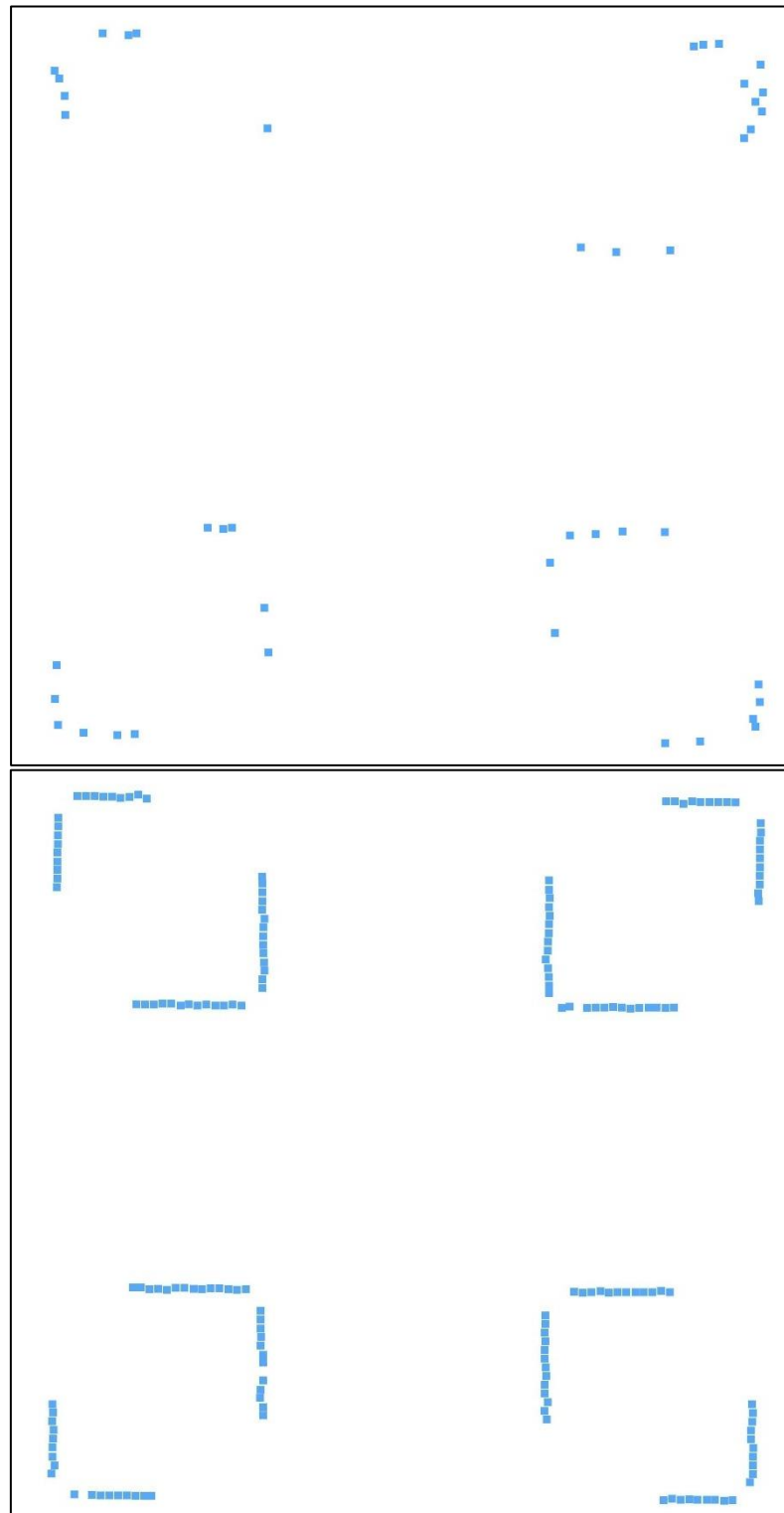
Figure 54 Corner points for every analyzed L60x6 member for both datasets.

Aerial point cloud(top), Terrestrial point cloud(bottom)

Results for every member from the aerial LiDAR scan were compared with the corresponding member from the terrestrial LiDAR point cloud in terms of number of outliers and the total number of inlier points defined for each member. The outlier boundary for both data sets was set as 5mm absolute distance of the corner point from the fitted line.

Results of the script for each members' point cloud pair are presented in Tab. 4.

	Member ID	1	2	3	4	5	6	7	8	9	10	11	12	13	14	15	16
Terrestrial LiDAR point cloud	Number of inlier points	7	8	6	7	6	8	7	9	10	7	8	7	6	9	9	8
	Number of outlier points	2	1	3	3	4	1	2	0	4	5	5	5	7	5	5	5
Aerial LiDAR point cloud	Number of inlier points	2	2	2	2	3	2	3	2	2	2	2	2	2	0	0	0
	Number of outlier points	1	1	0	2	4	1	0	2	1	0	0	2	1	0	1	0

Table 4 Small scale test results
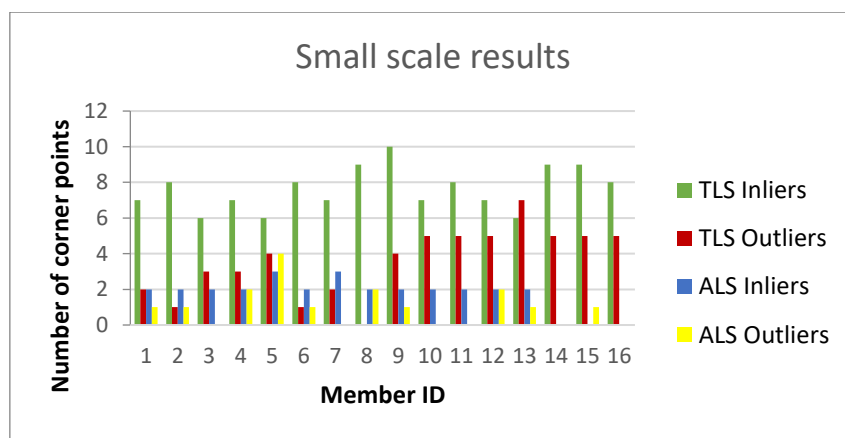
Figure 55 Graphical representation of small scale results presented in table 4

The visual output of the small-scale test is depicted in Fig. 56.
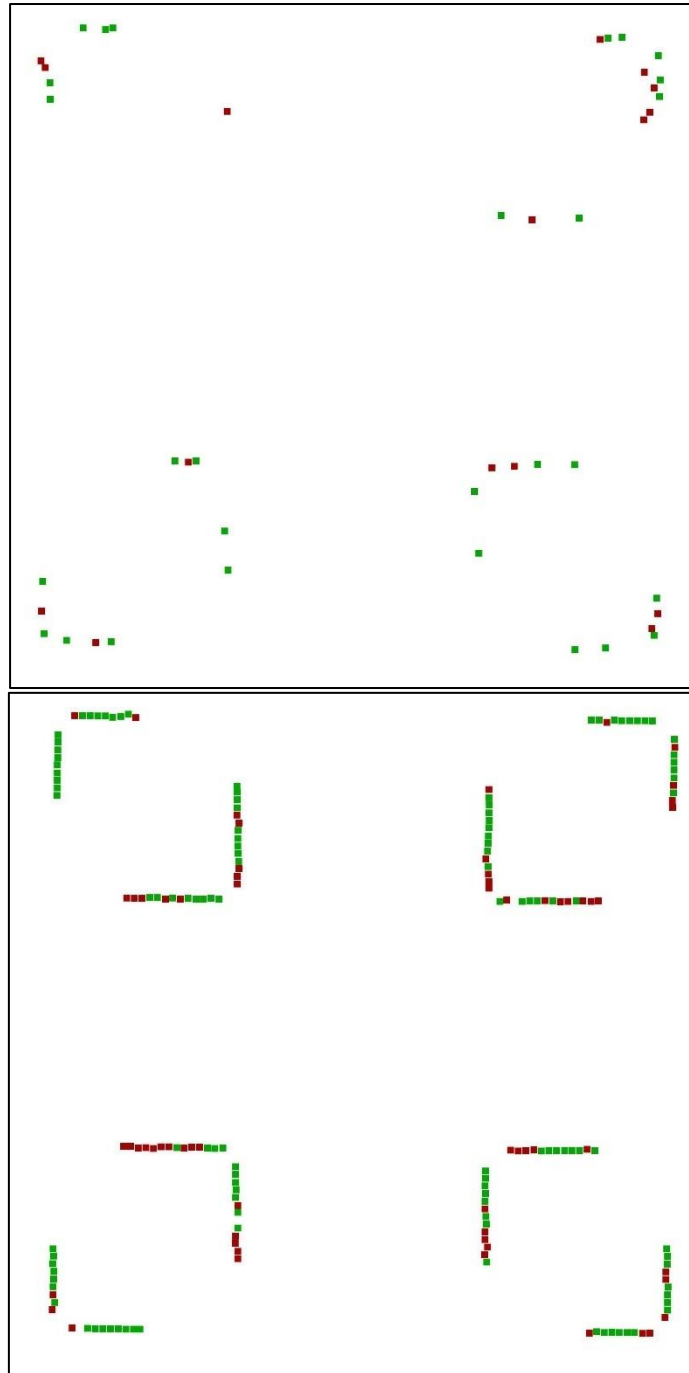
Figure 56 Small scale test results, inlier and outlier points are depicted in green and red color accordingly.

Aerial point cloud(top), Terrestrial point cloud(bottom)

Based on the comparison results, a decision has been made to apply the developed model generating script to the terrestrial point cloud. Considering the overall higher accuracy of the test results obtained with the terrestrial LiDAR data which will lead to a higher quality of the final geometrical model.

Nonetheless, the aerial point cloud data will be utilized for geometrical modelling purposes using a line extraction method available within a commercial software TerraSolid.

A detailed description of both modelling approaches is described in Sections 3.5 and 3.6.

3.5 Comparison of the Terrestrial LiDAR point cloud with standard profiles geometry according to EN 1090-2

Before delving into the geometrical model generating methods, to better understand the differences of scanned in-situ steel profiles and standardized European steel profiles, a comparison between the two was performed.

The process involved a comparison of selected members extracted from terrestrial point cloud with idealized reference models based on design documentation and standardized European steel profiles according to [22].

The workflow for the comparison of the point cloud data and the idealized reference model is presented in Fig. 57.
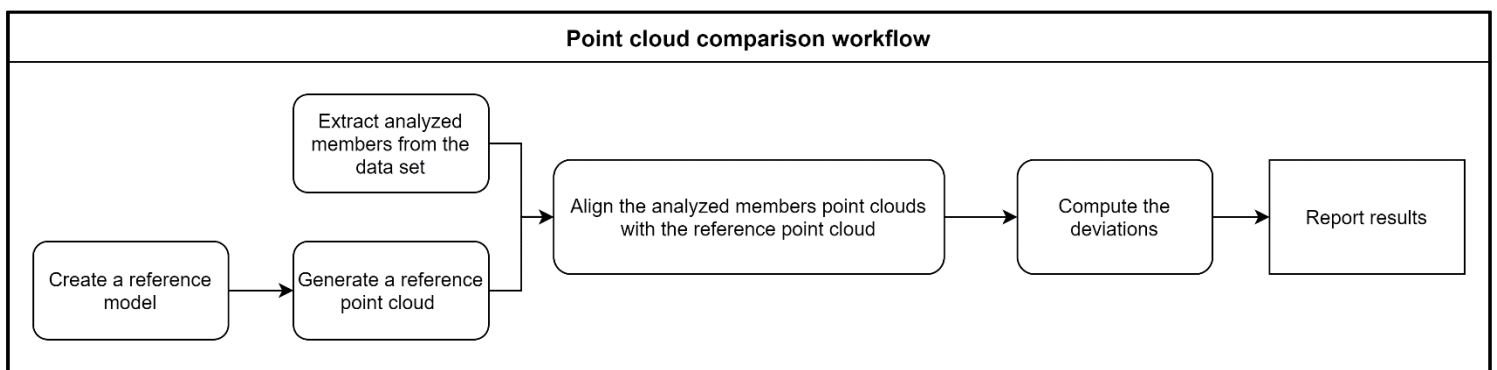
Figure 57 Point cloud comparison workflow

Extraction of analyzed members sections

In order to visualize the difference between the real-life scanned profile and an idealized steel profile, the analyzed members should depict imperfections which underline deviations between an in-situ structure and the idealized model. To show that phenomena, the longest members with high slenderness ratio were chosen for the investigation. The analyzed members are horizontal bracings members, with the section L150x12mm as shown in Fig. 58.
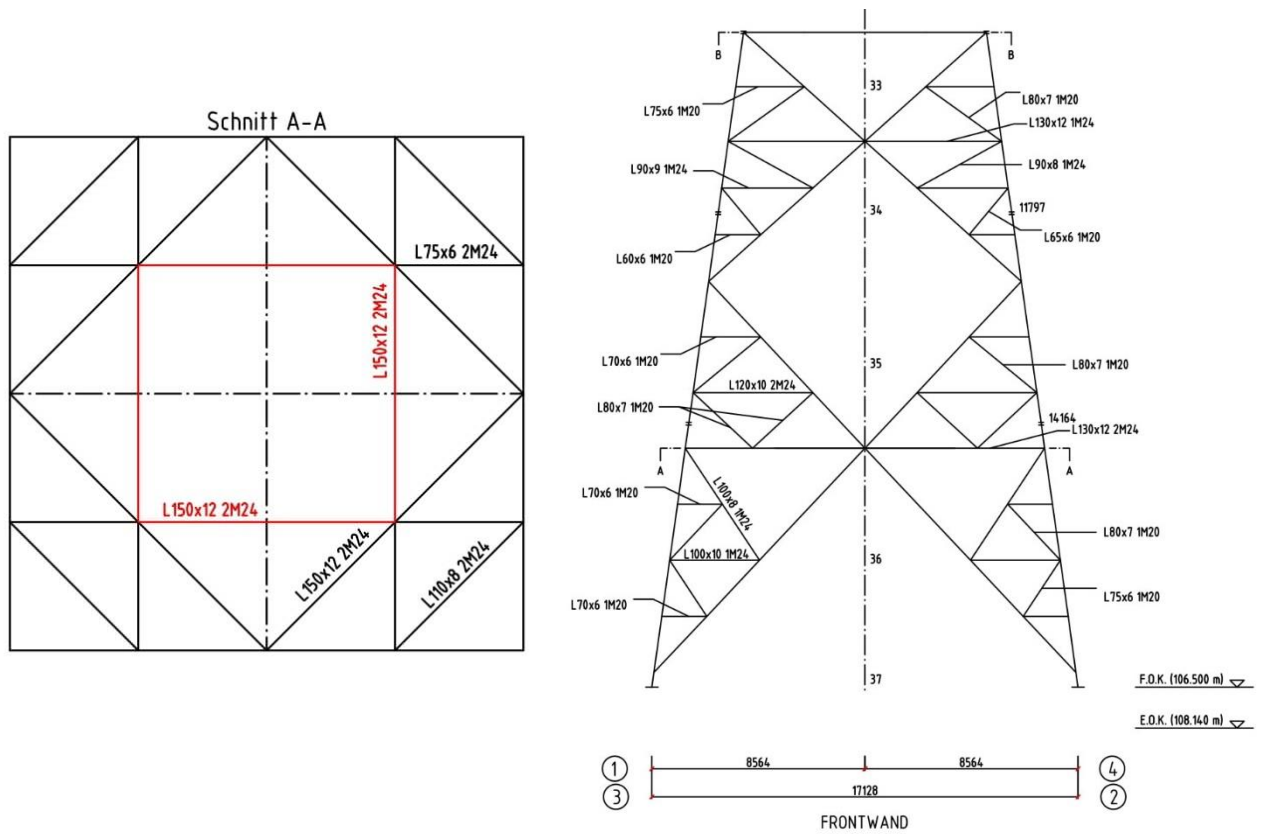
Figure 58 L150x12 members location in the analyzed lattice tower segment

The dimensions of the standard L150x12mm profile based on [22] are depicted in Tab. 5.

b = 150 mm	A = 3483 mm^2
t = 12 mm	G = 27.35 kg.m^{-1}
r_1 = 16 mm	A_L = 0.5863 m^2.m^{-1}
r_2 = 8 mm	v = 106.1 mm
y_s = 41.2 mm	u_1 = 58.3 mm
y'_s = 108.8 mm	u_2 = 52.9 mm

Table 5 L150x12 dimensions
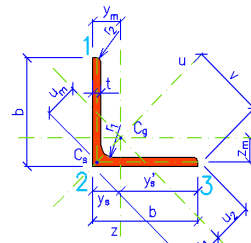
Figure 59 L cross section

Fig. 60 depicts the extracted L150x12 members.
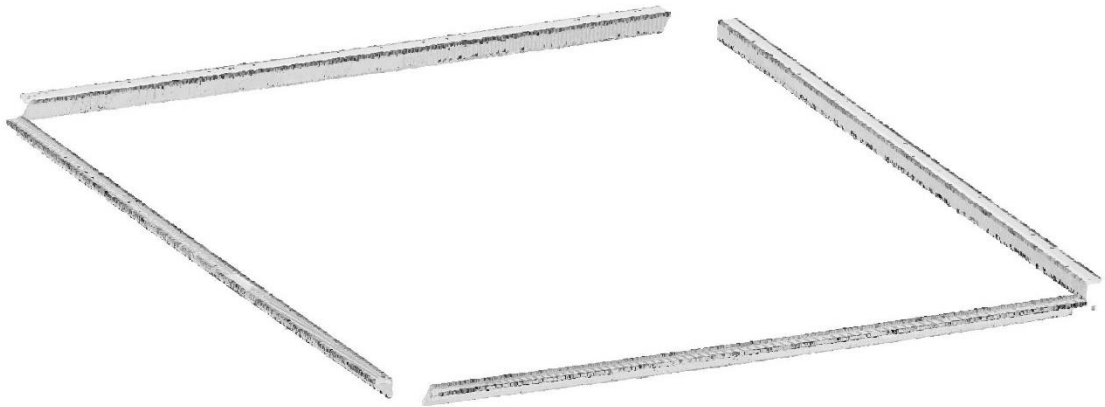
Figure 60 Terrestrial point cloud of L150x12 members in the analyzed lattice tower segment

After extracting the analyzed section, a reference model has been created.

Create the reference model
The reference members have been manually created in Autodesk AutoCAD 2020 software [ref] using extrusion of the steel cross-sections based on design documentation. The model is a 3D surface mesh model with a length of 7 meters, Fig. 61. The reference model is an idealized representation of the L-shaped steel profile, no imperfections were included.
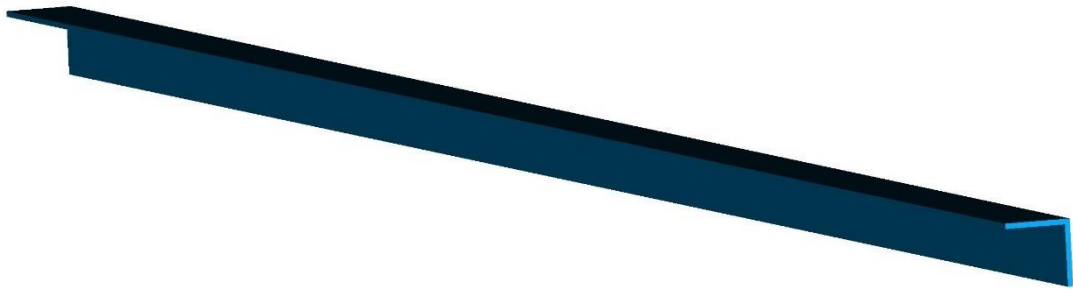
Figure 61 Idealized L150x12 reference member

Generate the reference point cloud
In order to compare the reference model and the point cloud data, the surface of the reference model was converted into a point cloud using a point sampling tool from CloudCompare software. The sampling method uses the information from the surface mesh of the model to interpolate points inside each triangle or quadrilateral.

The resulting point cloud depends on the user specified density or total amount of requested points. For the reference point cloud 1 000 000 points were assumed, allowing to obtain a very high point cloud density of the reference model required for next steps of the comparison process. Fig. 62 depicts the reference point cloud.
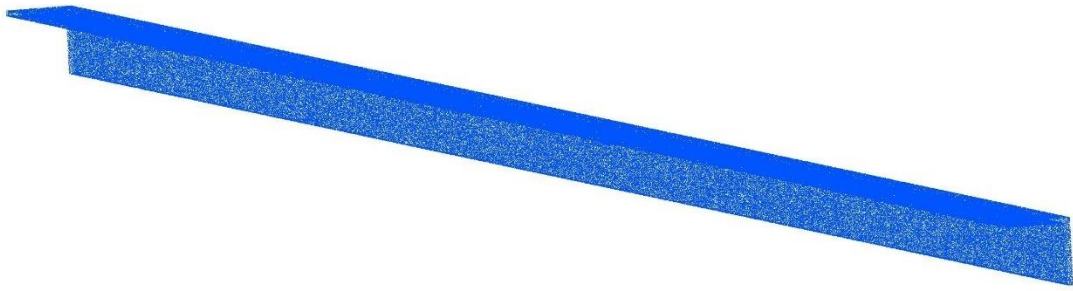
Figure 62 Points sampled on the idealized reference member

Alignment of analyzed members point cloud with the reference point cloud

Conversion of the surface mesh model to a point cloud data allowed to align the acquired LiDAR point cloud with the reference point cloud using iterative closest point(ICP) method.

The ICP algorithm as depicted in Fig. 63 iteratively computes transformation matrixes between two point clouds required to minimize the mean square of Euclidean distance between each pair of closest points of analyzed and reference point clouds.
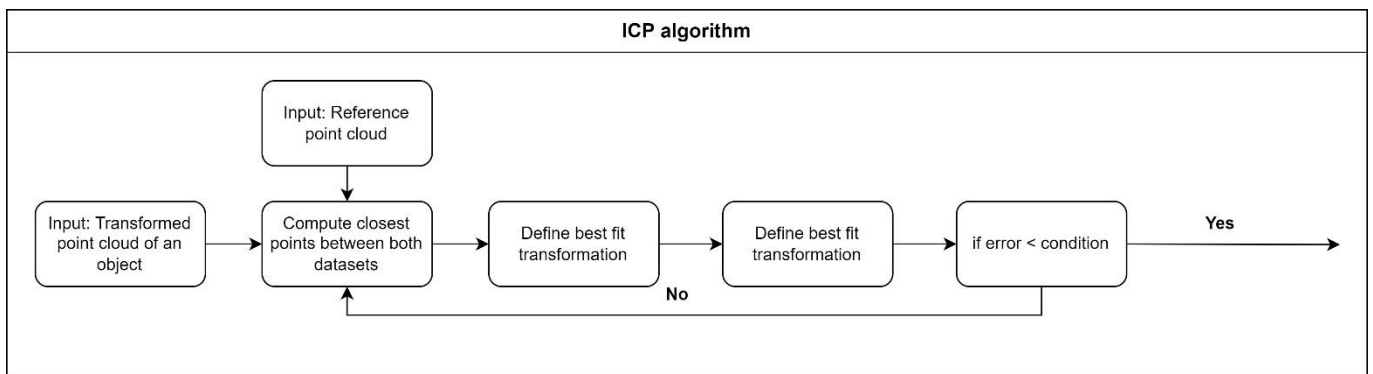
Figure 63 ICP algorithm

Afterwards, the transformation matrix is applied to the analyzed point cloud and the process is re-peated until the minimum mean square threshold is satisfied or the number of iterations is met. When comparing the terrestrial LiDAR point cloud, the analyzed data sets were aligned with the reference point cloud using ICP implementation tool from CloudCompare, the input variables of mean square distance and number of iterations were set to 1e-05 and 20 accordingly.

The aligned point cloud is depicted in Fig. 64.
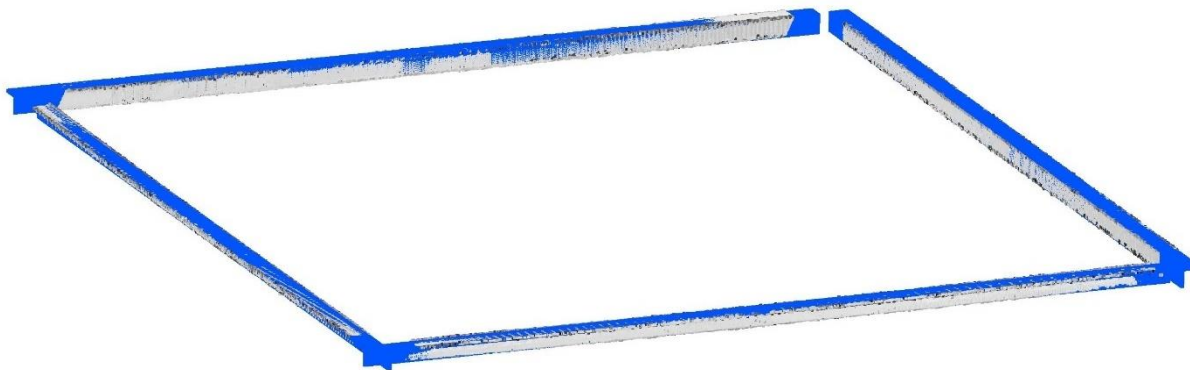
Figure 64 Analyzed L150x12 members' point cloud aligned with the idealized reference members' point cloud

Computing deviations

After alignment of the analyzed LiDAR point cloud with the reference point cloud the deviations for all members were computed as distances using nearest neighbor search algorithm explained in Section 2.2. The computation results are depicted in Fig. 65.
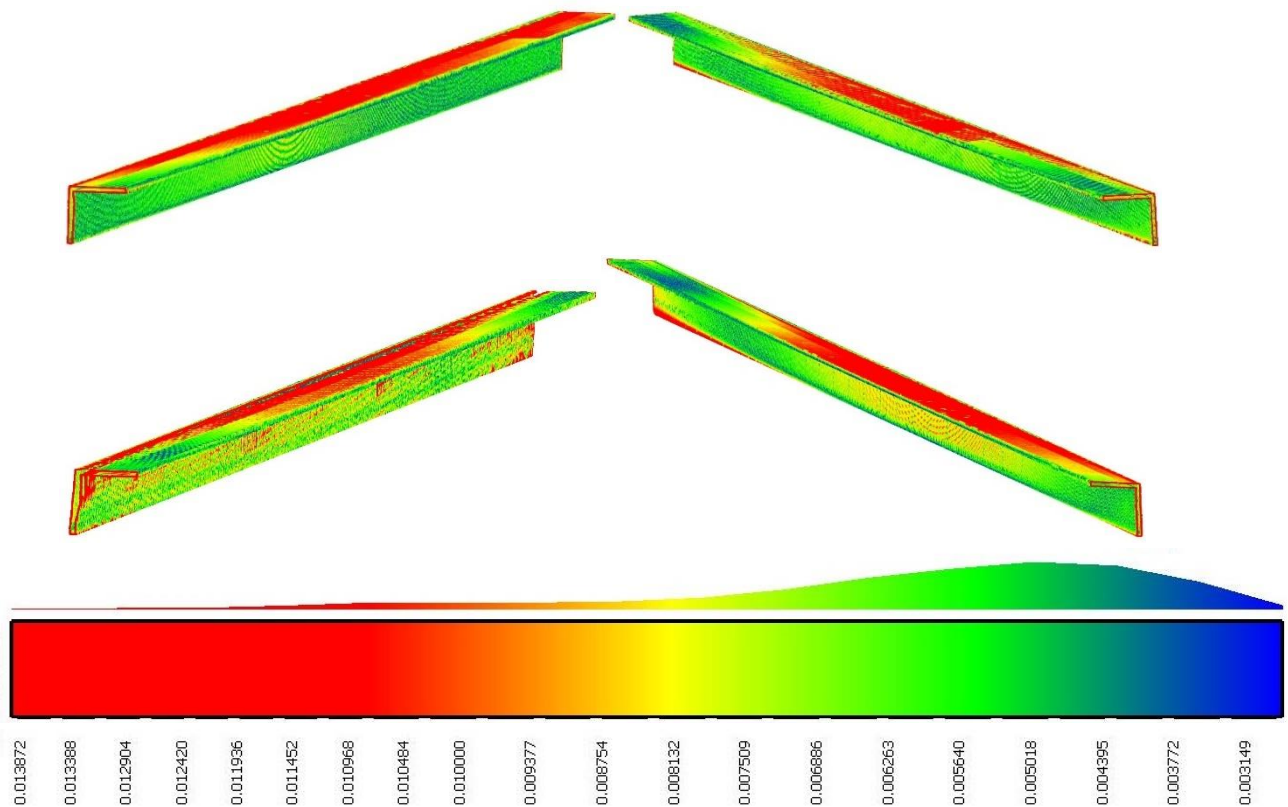
Figure 65 Comparison results

The scalar field depicts the deviation range for all the analyzed specimens. Red color regions indicate deviation larger than 1cm.

Comparing the acquired terrestrial point cloud data to an idealized reference model allows to understand the relevance of using the in-situ geometry of the structure when generating a digital model of a steel lattice tower. As depicted in Fig. 65, for analyzed L150x12 members a parabolic deformation occurs for all four members. The shape and direction of the deformation resemble a simply supported beam loaded by an uniformly distributed load. Presumably, in the analyzed case the major uniform load is the self-weight of the beam. To validate the interpretation, the geometrical comparison results have been compared to an analytical solution of an idealized L150x12 reference beam. The resulting ULS deformation of the reference beam $d_{reference}$=1,3cm. Considering the results of the reference beam oscillate in the range of in-situ beam deviations, the comparison with analytical results indicates that using the point cloud data enables to depict the deformed state of the structure. The computation for the analytical solution is provided in Appendix A.

After validating the post processed point clouds, both data sets will be utilized in the geometrical model generation stage.
In the following Sections, two approaches for geometrical model generating methods using the post processed point clouds data will be explained.

3.6 Vectorization of Aerial point cloud data

The first method to generate the geometrical model of the steel lattice tower using the point cloud data was to use already developed post processing algorithms to obtain the global geometrical information of the structure. In the method, every member was manually detected and discretized as a line element representing the longitudinal axis of each steel member of the analyzed lattice tower segment. This approach gives an insight into a solution using currently available point cloud processing software.

The basic algorithm behind line extraction from point cloud data has been introduced in Section 2.3. For the method utilized in this thesis, a semi-automatized approach has been carried out with the use of a commercial software called TerraSolid Modeler. Lines representing the geometrical center of an analyzed point cloud of a linear object can be generated using a vectorization tool available in the software. Vectorization of a point cloud data is a line extraction algorithm, which generates vectors running through a predefined point cloud cluster, as shown in Fig. 66.
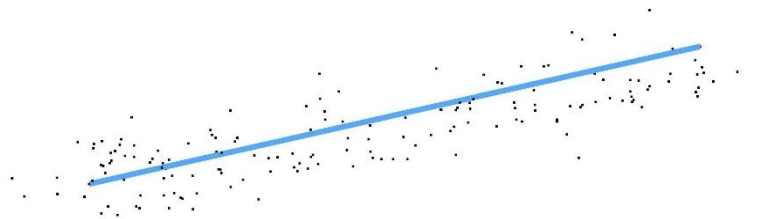
Figure 66 Point cloud data vectorization example

The main feature of the method is its low complexity, lines representing members location in a 3D space are defined by picking two end points for every member. Afterwards, a vector running through a point cloud cluster between the two defined points is generated. In the case of the lattice tower, chosen points were selected in the approximated position of connections of every member. An example of a point cloud data vectorization is given in Fig. 67.
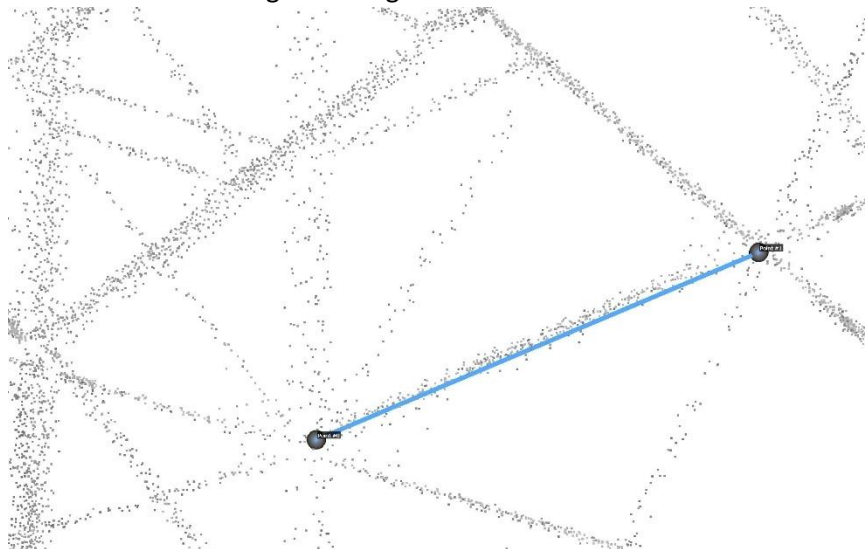
Figure 67 Vectorization applied to the aerial data set

The simplicity of the solution is both a pro and a con of the method. The main advantage of this approach was the ability to generate a model with no prior experience in point cloud processing. The computational part of vectorizing the data is carried by the software, limiting users input to defining the initial boundary points of the generated line.

On the other hand, the low dependency on identifying the line by the user leads to results with accuracy which is hard to evaluate without the knowledge of intermediate steps of the vectorization algorithm. The initial step of defining the end points of the generated line is the only stage when users decisions have an impact on the resulting line. What is more, the point picking step is not solved numerically, they are not calculated based on geometrical features or point cloud properties of the scanned lattice tower but by approximately choosing the end points of the member using visual guidance of the point cloud data.

Therefore, the accuracy of the line positioning in the 3D space could not be validated for the vectorization approach applied to the aerial LiDAR data. To understand the differences in final geometrical models, the resulting geometrical line model based on the vectorization method is compared to that from an idealized model based on design documentation and one based on the line generation algorithm developed for the purpose of this work. For the geometrical model based on the line generation algorithm, the positioning of a line representing a member is computed using geometrical features of scanned steel profiles allowing to estimate the expected position of members.

The geometrical model based on the vectorization approach is treated as an example of a commercial alternative to the method proposed in the thesis. Unfortunately, no details regarding the vectorization tool's algorithm are accessible therefore the method is treated as a black box approach, where only the input and the output of the process are known. Thus, the resulting geometrical model cannot be validated in terms of accuracy.

Nonetheless, due to the fact that the line generating algorithm utilized for the method introduced in the thesis did not give satisfying results for this data type, as stated in Section 3.3, this approach was a good alternative solution to generate a model using the aerial LiDAR point cloud.

Digitally reconstructing the lattice tower based on the aerial data set was important for the context of this work. It gave an in-situ based reference to the geometrical model created with the developed method, enabling to conduct a comparison between two geometrical models of the same lattice structure generated with point cloud data gathered with different LiDAR acquisition instruments. The model generation process using vectorization approach on the aerial data is depicted in the following graph, Fig. 68.
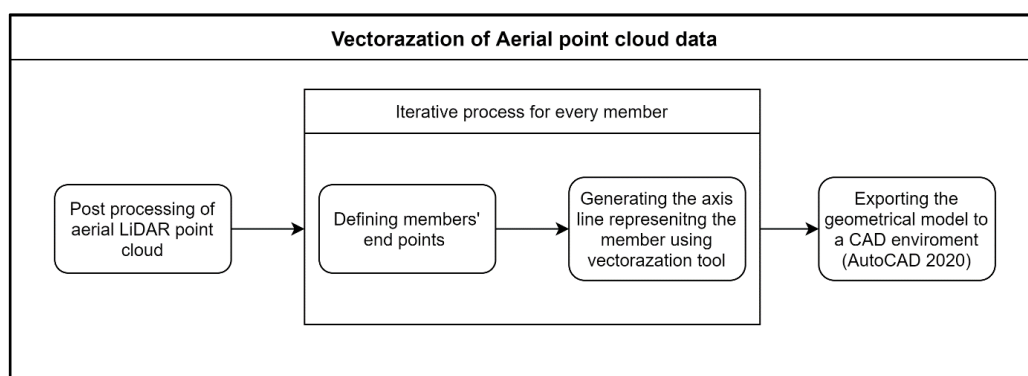
Figure 68 Model generation process using vectorization approach

The resulting geometrical model created with the vectorization method using aerial LiDAR point cloud is depicted in Fig. 69.
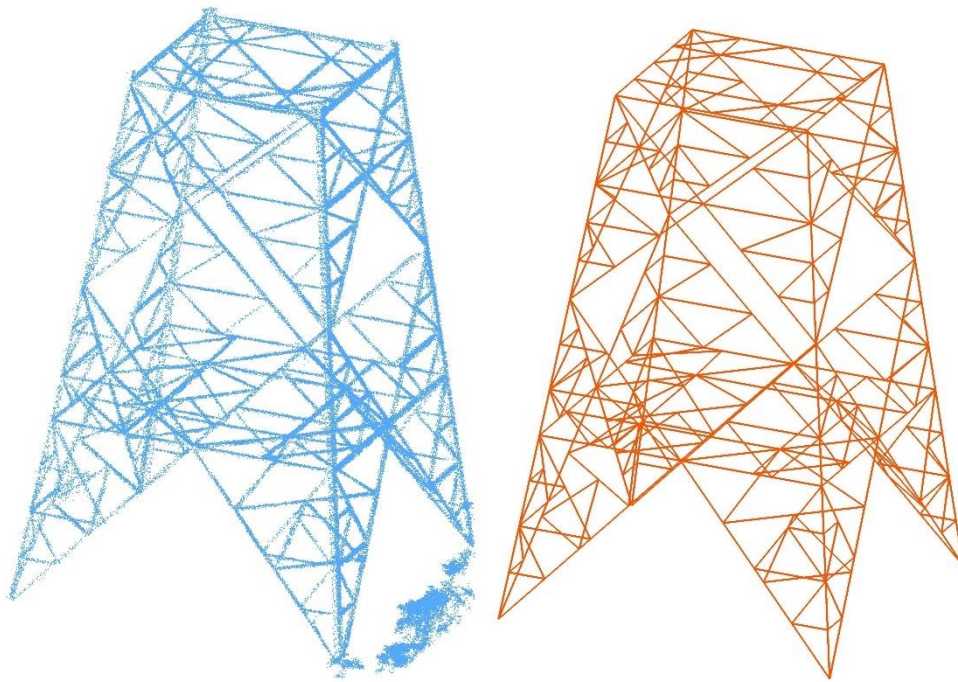
Figure 69 Geometrical model of the analyzed lattice tower segment(right) based on aerial point cloud(left) generated using vectorazation method

3.7   Model generating script for the Terrestrial LiDAR point cloud

In this Section, the method for the model generating method developed for the purpose of this thesis will be explained on its application for the terrestrial LiDAR point cloud. The output of the proposed method is a polyline CAD model representing longitudinal axis of steel members of the lattice tower, similarly to the model defined in the previous approach. The main difference of the proposed approach comes from the implementation of a numerical method used for the line estimation. The line generation step is not based on an approximated manual line detection but on measuring geometrical features of the scanned steel profile from the point cloud data. This way the generated lines location in the cross-section is precisely defined and not randomly positioned depending on the quality of the data. Fig. 70 depicts the difference of both approaches.
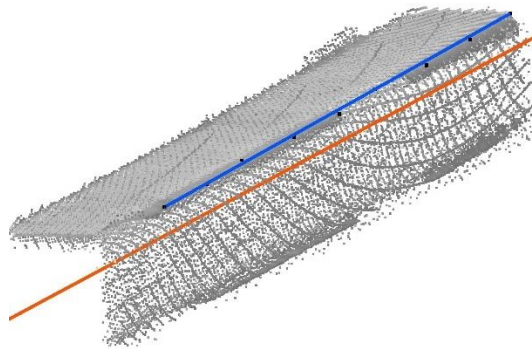
Figure 70 Difference between line fitting methods,

vectorization(orange) and approach proposed in the thesis(blue)

The method introduced in this Section covers the complete process of analyzing the steel lattice tower. Even though its application in the thesis is limited to a lower part of the structure (defined in Section 3.1), the proposed method is applicable to an entire structure.

The general concept of the approach focuses on extracting individual members of the analyzed structure. Thereafter, the line segmentation script is applied to the point cloud of the member to obtain the geometrical information on the polyline representing each member. The output of the process is a polyline CAD model. Due to a complicated geometry of power grid lattice towers, working on member extraction for the entire structure is not effective and very complex. Therefore, prior to member extraction, the tower is subdivided into multiple Sections separated by horizontal bracings of the tower.

The proposed method can be divided in three main parts, as shown in Fig. 71.
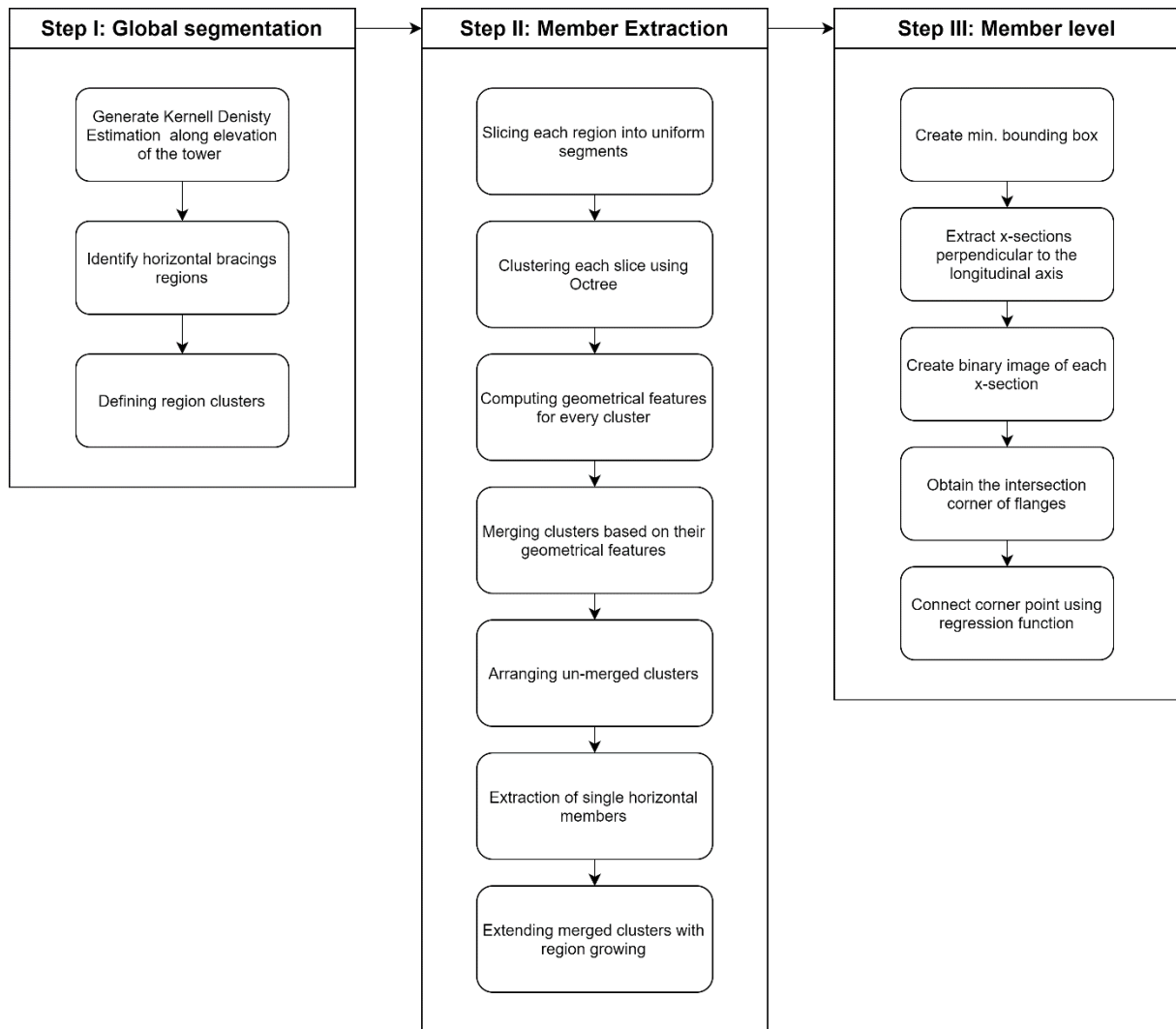
Figure 71 Geometrical model generating script algorithm

All the steps depicted in Fig. 71 were performed on the analyzed tower segment using the terrestrial LiDAR point cloud. Detailed description of the process carried in this thesis is presented below.

3.7.1 Step I: Global segmentation

The first step of the proposed method focuses on simplifying the analyzed problem by dividing the entire tower into segments which are easier to work with. The segments' size is defined by the distance between succeeding horizontal bracings. The result of the global segmentation step are two different types of point cloud clusters. The first one, representing all members within horizontal bracings Sections and the other one depicting all members of Sections in-between horizontal bracings. Fig. 72 illustrates two types of resulting clusters. The global segmentation consists of three sub-steps, in which Kernel density estimation (KDE) along the height of the tower is used to detect the locations of the horizontal bracings.
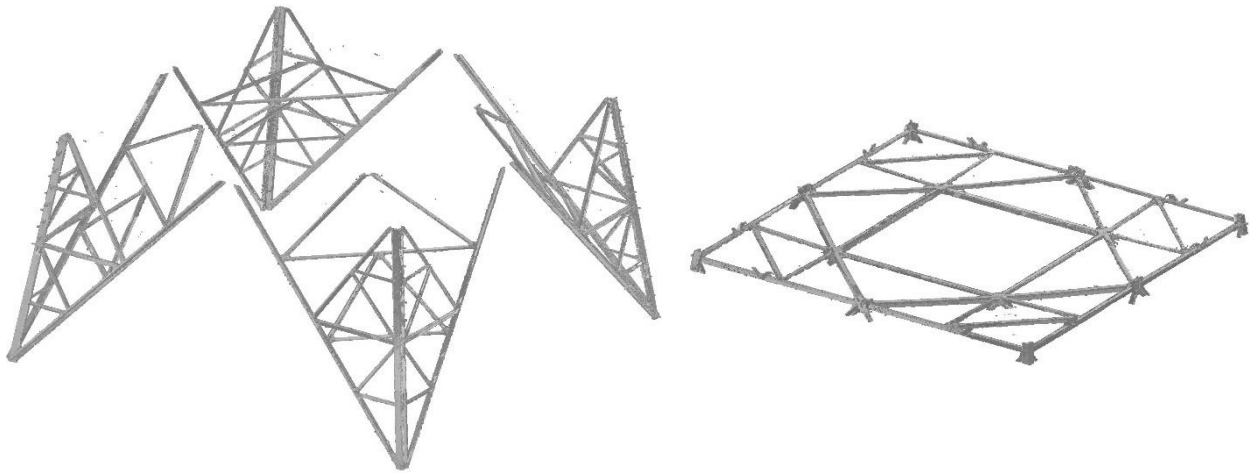
Figure 72 In-between bracings(left) and bracing(right) segments

Generating Kernel density estimation

A detailed explanation of the KDE algorithm was given in Section 2.2. In the scope of this study, KDE has been applied to the terrestrial LiDAR point cloud of the analyzed bottom part of the lattice tower along the global Z coordinate of the data which represents the height direction of the structure. The inputs for KDE algorithm includes z-coordinate of the point cloud and the bandwidth determining the smoothness of the density function. For the TLS data set analyzed in the thesis, the bandwidth has been set to 0.1m.

The resulting KDE function is presented in Fig. 73.
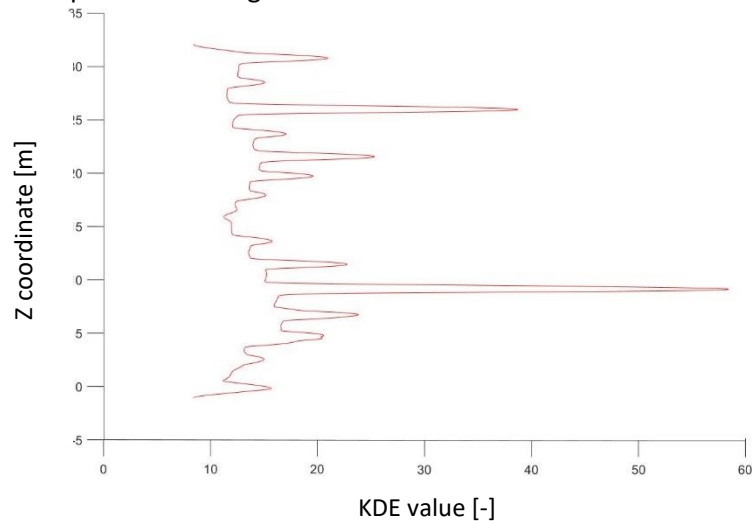
Figure 73 KDE function applied along the elevation coordinate

on the analyzed lattice tower segment

The peaks of KDE depict locations of horizontal bracings along Z coordinate. After generating KDE for the analyzed point cloud the extraction of horizontal bracings was performed.

Identify horizontal bracings sections

In order to show how the KDE function was used to extract the horizontal bracing the KDE graph is overlapped with the analyzed point cloud, Fig. 74.
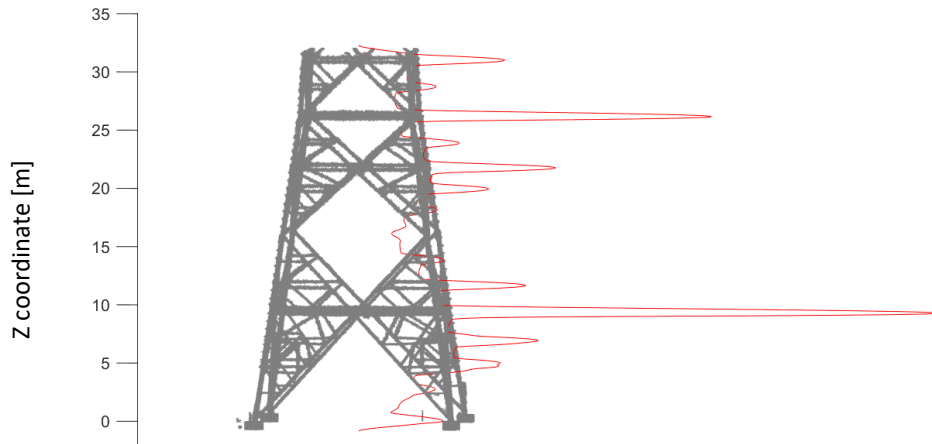
Figure 74 KDE function overlapped with the point cloud data

As it can be seen in Fig. 74, three horizontal bracing Sections are located at Z_1 = 9m, Z_2 = 21m, and Z_3 = 26m measured from the bottom of the tower, which corresponds to the three peaks.

The exact location of the peaks was determined based on the first and the second derivative of the KDE function, allowing to find local extremes where the function was changing the trend from ascending to descending, Fig. 75.
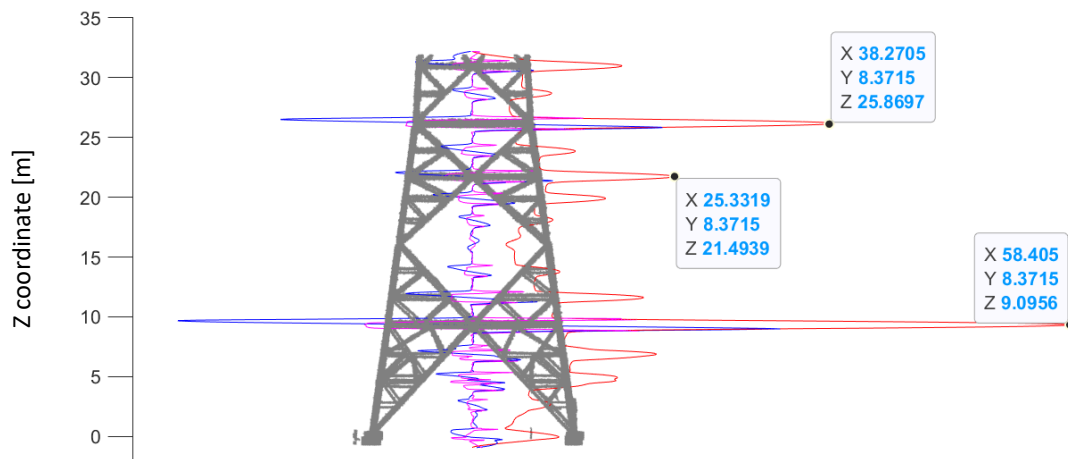
Figure 75 Exact location of the peaks in the KDE function

After detecting the important peak values of the KDE function, all points located on the elevations of Z_1, Z_2 and Z_3 coordinate could be segmented into separate clusters. The extraction regions were increased by the bandwidth, allowing for segmentation of an entire horizontal bracing.

The horizontal bracings' clusters were defined by searching for all points inside regions along Z coordinate, defined as:

$$< Z_i - bandwidth; \; Z_i + bandwidth >$$

Equation 5

The extracted sections are depicted in Fig. 76.
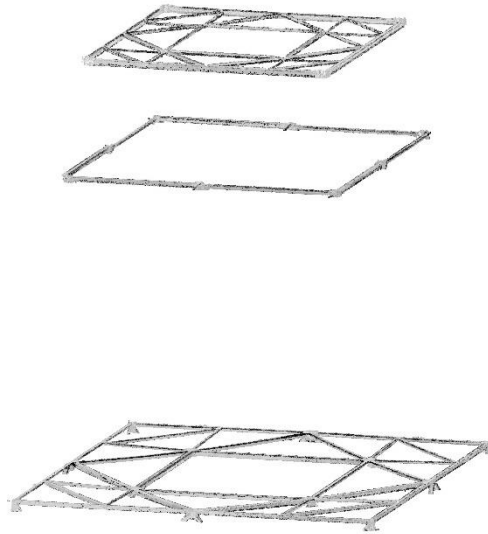
Figure 76 Isolated bracing regions in the analyzed lattice tower segment

After detecting the horizontal bracing regions the leftover points could be assigned to separate clusters depicting all diagonal and vertical members in-between the horizontal sections.

Defining in-between region clusters
In the final step of global segmentation the leftover points are divided into separate regions, defined as:

$$< Z_i + bandwidth; \ Z_{i+1} - bandwidth >$$

<div align="right">*Equation 6*</div>

The final result for all the segmented region clusters is depicted in Fig. 77. Each cluster is highlighted by a different color.
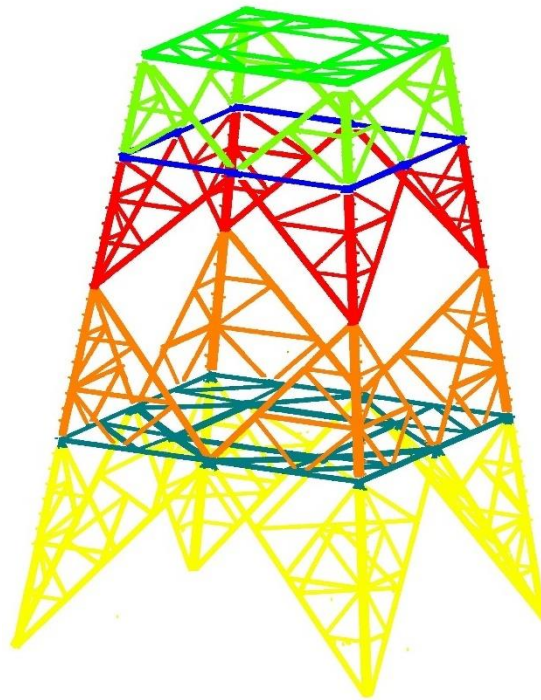
Figure 77 Final result of global segmentation

Although the application of the global segmentation in this thesis is limited to the analyzed lower part of the lattice tower, a similar procedure can be applied to the entire structure. Fig. 78 depicts application of KDE on the aerial LiDAR point cloud of the whole lattice tower, the peaks of the KDE function depict locations of horizontal bracings where the tower could be divided into regions accordingly to the method applied to the data analyzed in this work.
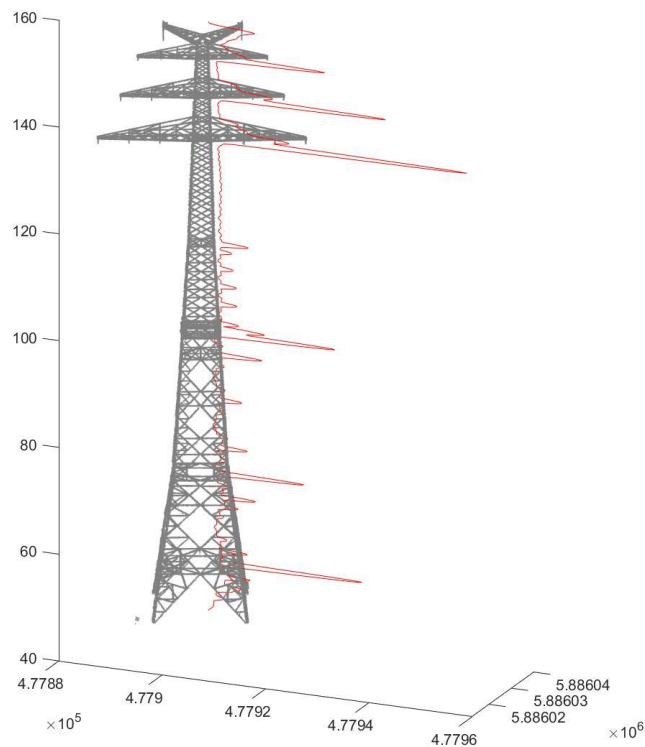
Figure 78 KDE function applied along elevation coordinate to the aerial point cloud of the entire lattice tower

In the next step, the proposed method will be continued on the segmented regions, where each member will be separated into an individual cluster.

3.7.2 Step II: Member extraction

This step focuses on extracting members from previously segmented clusters. The algorithm behind member extraction is explained on the examples of the middle cluster and a horizontal bracing cluster obtained in the previous step, Fig. 79.
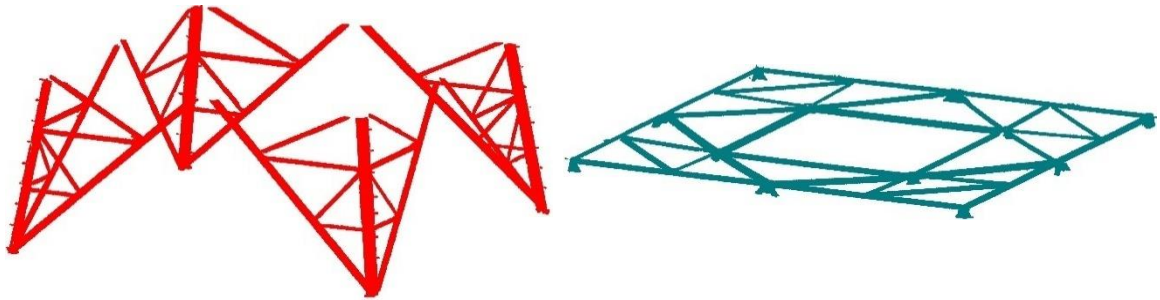
Figure 79 In-between bracings(left) and bracing(right) segments

The member extraction step is based on the region growing hypothesis combined with a slicing method. In this work, the slicing method is applied to the point cloud of the cluster to create sub-clusters representing sliced parts of members. The sub-clusters of an individual member are then combined into entire members by merging them together based on their geometrical features.

The member extraction is the most elaborate step in the proposed method, it is divided into 7 sub-steps due to the complexity of the task it is solving. The general approach is to simplify the point cloud of the analyzed structure to the point when the entire data set is divided into small clusters which are later combined into larger groups containing common geometrical features.

Slicing each region into uniform segments

The slicing method is applied to divide the point cloud data into sub-clusters representing parts of members.

Before applying the method, each region was transformed to its local coordinate system in a way allowing for the most efficient slice generation. As it has been defined in Step I, there are two types of clusters after the global segmentation step:

- horizontal bracing regions
- in-between bracings regions

For the horizontal bracing regions, the XZ plane of the local coordinate system is defined as the horizontal plane of the bracing with positive X and Z directions aligned with perpendicular directions of the bracings frame, Fig. 80.
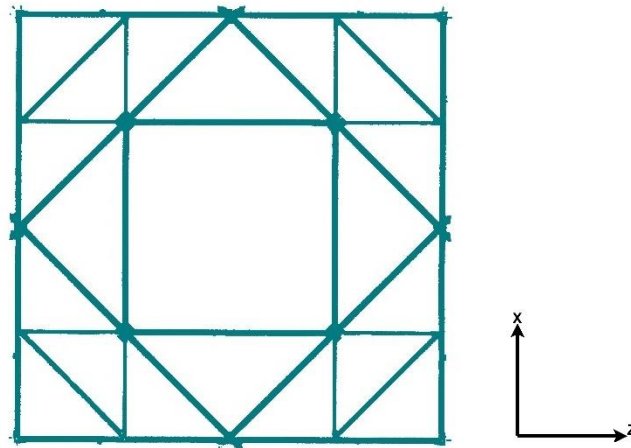
Figure 80 Local coordinate system of the bracing segment

The Y coordinate is defined as the normal vector of the XZ plane equal to the global Z+ coordinate of the structure.

For the in-between bracings regions, the local coordinate of the region equals to the global coordinate of the structure, Fig. 81.
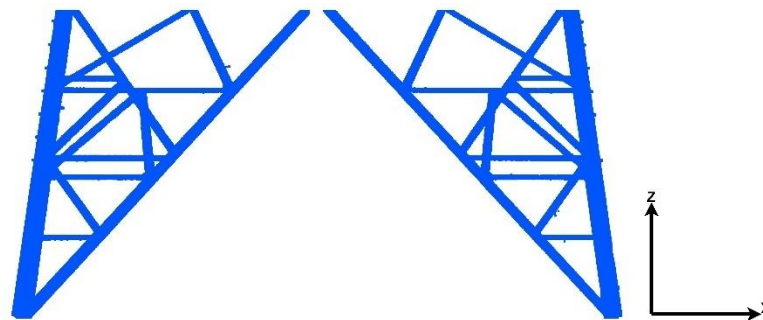
Figure 81 Local coordinate of the in-between bracing segment

After the local coordinate systems was established, every region has been divided into uniform slices along the local Z direction. The thickness of each slice was adopted as 60 cm. The number of slices generated depends on the dimension of the cluster in the Z direction.

The results of the slicing method are depicted in Fig. 82.
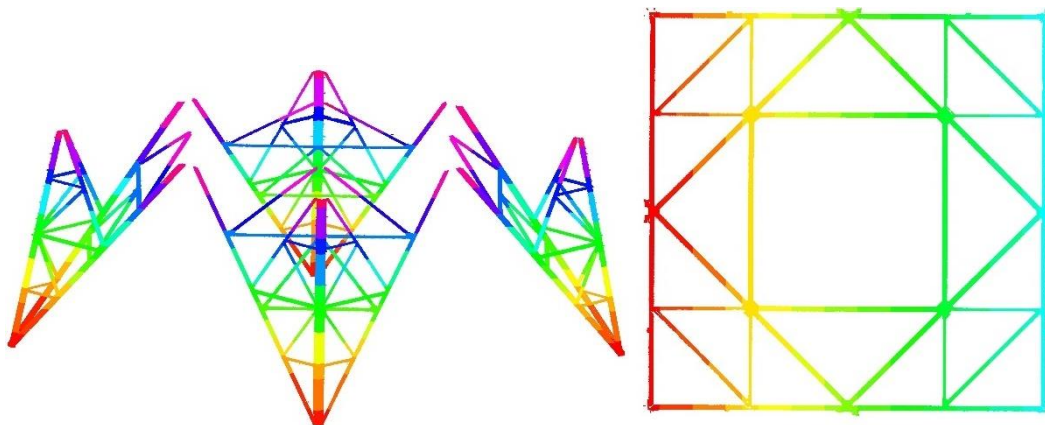
Figure 82 Slicing method results

Clustering each slice using Octree

After subdividing the region into uniform slices, the segmentation process starts at the slice level. Sub-clusters representing sliced member parts need to be extracted.

To sub-cluster members parts inside each slice, a Quadtree algorithm [23] has been utilized, enclosing all points in a cell tree structure. Quadtree is a two dimensional version of the Octree algorithm explained in Section 2.2. The algorithm is identical to the three dimensional version but allows for faster computations when the desired tree structure of the analyzed data can be considered as a planar case, as with generated slices, Fig. 83.
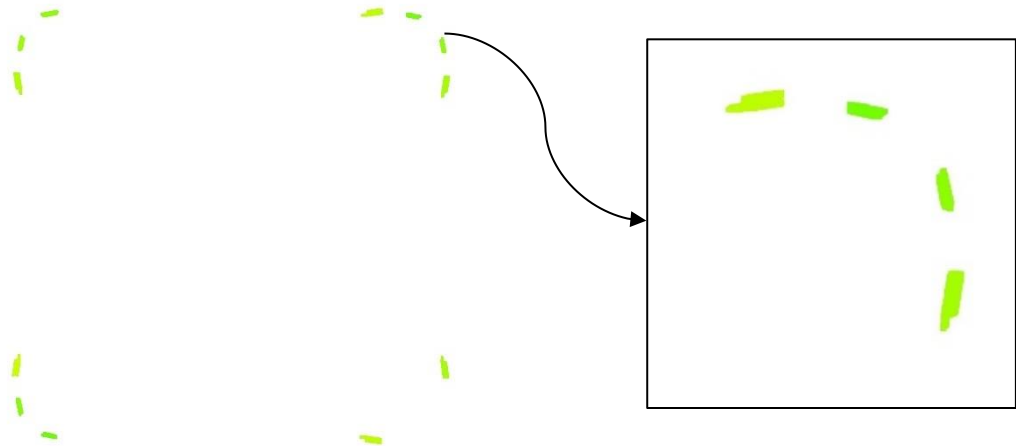
Figure 83 Isolated slice for the in-between segment

The Quadtree has been generated for the XY plane of the local coordinate system of each region. The input parameter of the Quadtree algorithm was the minimum size of the cell, which has been set to 5x5 cm^2. Fig. 84 illustrates the data of an exemplary slice.
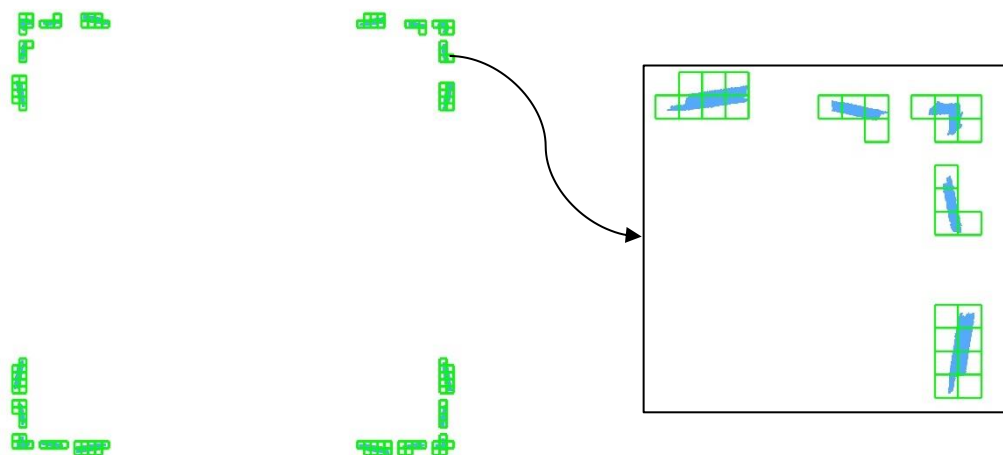
Figure 84 Quadtree applied to a slice

Afterwards, all cells of the member are connected with their neighbors to create the sliced members parts clusters. The sub-clusters are achieved by grouping neighboring voxels connected with each other, Fig. 85.
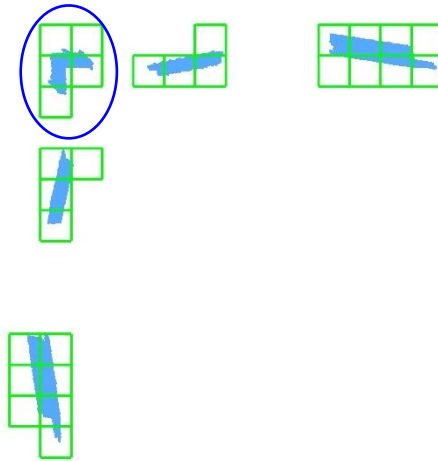
Figure 85 Members parts clusters generation, a single cluster circled in blue

The procedure is applied to every slice in every region of the analyzed data enabling to generate sliced members parts, Fig. 86.
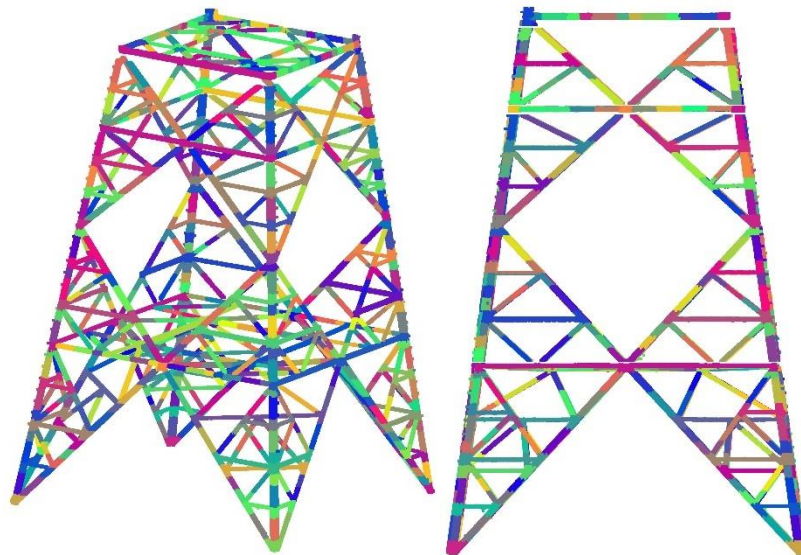
Figure 86 Sliced members parts clusters

At this stage the data is subdivided to the smallest sub-cluster level utilized in this method, succeeding steps focus on merging those sub-clusters in order to assign given points to a specific member of the analyzed lattice tower.

Computing geometrical features for every sub-cluster
The sub-clusters of members parts is merged with each other based on their geometrical features. All parameters are computed from a minimum bounding volume enclosing all points of the cluster. The following geometrical features have been computed:

- Geometrical center, C_{geom}
- Minimum bounding box dimensions
- Cross-sectional area, $A_{x-section}$
- Normalized longitudinal direction vector, $\overrightarrow{V_{N3}}$
- Cross-sectional direction vectors, $\overrightarrow{V_1}$, $\overrightarrow{V_2}$

A visualization of measured geometrical features is depicted in Fig. 87 on the example of an isolated cluster.
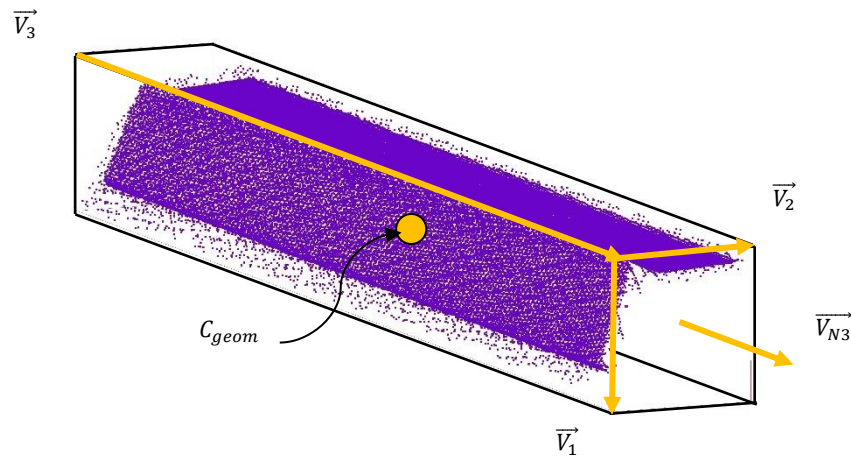
Figure 87 Geometrical features of a member's part cluster

Geometrical center
The geometrical center has been defined as the mean value of eight corner points of the minimum bounding box:

$$C_{geom} = \frac{\Sigma P_m[i, j, k]}{8}$$

Equation 7

,where
ΣP_m- is the sum of coordinates of all eight points

Minimum bounding box dimensions
The minimum bounding box dimensions have been computed based on lengths of three directional vectors of the enclosing volume $\overrightarrow{V_1}$, $\overrightarrow{V_2}$ and $\overrightarrow{V_3}$.

Cross-sectional area
The cross-sectional area is defined as a plane between the two smallest directional vectors, knowing the vectors are orthogonal the computed area is given by equation:

$$A_{x-section} = V_{L1} * V_{L2}$$

Equation 8

Normalized longitudinal direction vector
The normalized longitudinal vector $\overrightarrow{V_{N3}}$ is the longest directional vector of the box $\overrightarrow{V_3}$ divided by its length.
The geometrical features have been computed for every cluster in the analyzed data set, which allowed to generate a matrix containing all the information required to begin the merging process. Fig. 88 depicts the structure of the resulting database.

	Pts_clustered	Geom_center	A_x_section	MBB_dimensions	V_N3	V_N1	V_N2
1	110959x3 double	[25.9628,8.4197,3.8541]	0.1693	[0.2823;0.5998;9.8715]	[-1.1273e-05,1.0000,6.9893e-05]	[1.0000,1.1298e-05,-3.5103e-04]	[-1.1273e-05,1.0000,6.9893e-05]
2	7987x3 double	[25.9787,7.6058,4.4489]	0.0233	[0.1454;0.1601;0.9837]	[0.0248,0.7130,-0.7007]	[0.9964,0.0389,0.0749]	[0.0248,0.7130,-0.7007]
3	9197x3 double	[25.9608,9.2765,4.4548]	0.0186	[0.1253;0.1487;0.9668]	[-7.3789e-04,0.7036,0.7106]	[0.9916,0.0925,-0.0905]	[-0.1294,0.7046,-0.6977]
4	5651x3 double	[25.9498,5.1776,4.4566]	0.0115	[0.0832;0.1377;0.9310]	[-0.0105,0.7183,-0.6957]	[0.8487,-0.3614,-0.3860]	[-0.0105,0.7183,-0.6957]
5	5602x3 double	[25.9531,11.6927,4.4566]	0.0097	[0.0843;0.1151;0.9227]	[-0.0095,0.6988,0.7153]	[0.9336,0.2625,-0.2440]	[-0.0095,0.6988,0.7153]
6	5131x3 double	[25.9589,3.5981,4.4539]	0.0242	[0.0965;0.2512;0.6000]	[-2.2513e-04,-0.0012,1.0000]	[0.9925,0.1220,3.7341e-04]	[-0.1220,0.9925,0.0012]
7	4492x3 double	[25.9466,13.2821,4.4538]	0.0237	[0.0961;0.2469;0.6009]	[-0.0050,-0.0034,1.0000]	[0.9979,-0.0647,0.0047]	[0.0647,0.9979,0.0037]
8	3099x3 double	[25.9038,6.0067,4.4538]	0.0075	[0.0759;0.0990;0.5996]	[-0.0040,0.0018,1.0000]	[0.9520,0.3061,0.0032]	[-0.3061,0.9520,-0.0029]
9	2690x3 double	[25.9074,10.8702,4.4540]	0.0061	[0.0519;0.1176;0.5992]	[-0.0104,0.0048,0.9999]	[0.8436,-0.5368,0.0114]	[0.5368,0.8437,0.0015]
10	12886x3 double	[25.9589,10.5298,5.6451]	0.1094	[0.1830;0.5979;0.9042]	[-0.1914,0.9811,0.0278]	[0.9652,0.1933,-0.1763]	[-0.1914,0.9811,0.0278]
11	10350x3 double	[25.9436,6.3370,5.6515]	0.0727	[0.1209;0.6016;0.8963]	[0.1230,0.9924,-0.0079]	[0.9869,-0.1232,-0.1041]	[0.1230,0.9924,-0.0079]
12	10956x3 double	[25.9913,3.9261,5.6535]	0.1405	[0.2327;0.6037;0.8104]	[0.1353,0.9908,-4.1688e-04]	[0.9905,-0.1353,0.0253]	[0.1353,0.9908,-4.1688e-04]
13	12651x3 double	[25.9826,12.9380,5.6535]	0.1426	[0.2376;0.6003;0.8210]	[-0.1298,0.9915,5.8079e-04]	[0.9915,0.1298,0.0063]	[-0.1298,0.9915,5.8079e-04]
14	110763x3 double	[25.9443,8.4301,6.2538]	0.1473	[0.2454;0.6002;9.8047]	[-1.9256e-04,1.0000,4.4359e-05]	[1.0000,1.9274e-04,-0.0041]	[-1.9256e-04,1.0000,4.4359e-05]
15	8575x3 double	[25.9543,11.6510,6.8503]	0.0187	[0.1348;0.1385;0.9530]	[0.0328,0.7057,0.7078]	[0.9974,0.0224,-0.0686]	[-0.0643,0.7082,-0.7031]
16	6960x3 double	[25.9522,5.2029,6.8653]	0.0163	[0.0919;0.1772;0.9798]	[-0.0070,0.7216,-0.6923]	[0.8455,-0.3654,-0.3894]	[-0.0070,0.7216,-0.6923]
17	5437x3 double	[25.9437,3.5845,6.8538]	0.0271	[0.1105;0.2453;0.5996]	[1.1585e-04,-0.0039,1.0000]	[0.9989,0.0459,6.3726e-05]	[-0.0459,0.9989,0.0039]
18	5480x3 double	[25.9466,10.8620,6.8542]	0.0186	[0.1310;0.1417;0.6016]	[-0.0253,-0.0214,0.9995]	[0.9858,0.1654,0.0285]	[-0.1660,0.9860,0.0169]
19	5197x3 double	[25.9442,13.2787,6.8538]	0.0247	[0.1001;0.2464;0.5999]	[-0.0015,6.4514e-05,1.0000]	[0.9991,-0.0430,0.0015]	[0.0430,0.9991,1.2773e-06]
20	6120x3 double	[25.9418,6.0054,6.8538]	0.0133	[0.0879;0.1510;0.6002]	[-3.9538e-04,0.0050,1.0000]	[0.9146,-0.4043,0.0024]	[0.4043,0.9146,-0.0044]
21	13580x3 double	[25.9849,3.9387,8.0539]	0.1352	[0.2252;0.6002;0.8635]	[0.1270,0.9919,2.4156e-04]	[0.9919,-0.1270,0.0022]	[0.1270,0.9919,2.4156e-04]
22	16606x3 double	[25.9763,12.8946,8.0539]	0.1366	[0.2276;0.6002;0.8849]	[-0.1142,0.9935,-7.9979e-05]	[0.9935,0.1142,-0.0015]	[-0.1142,0.9935,-7.9979e-05]
23	7303x3 double	[25.9373,5.9971,8.0539]	0.0159	[0.1017;0.1568;0.6000]	[-0.0024,2.4300e-04,1.0000]	[0.9371,-0.3489,0.0024]	[0.3489,0.9371,6.2261e-04]
24	6472x3 double	[25.9267,10.8458,8.0538]	0.0148	[0.0998;0.1480;6.6005]	[-0.0380,0.0062,0.9993]	[0.9106,0.4121,0.0321]	[-0.4116,0.9111,-0.0214]
25	11435x3 double	[25.9738,3.8104,8.6540]	0.1318	[0.2198;0.5999;0.6040]	[0.1576,0.9875,0.0017]	[0.9875,-0.1576,-8.5022e-04]	[0.1576,0.9875,0.0017]
26	15048x3 double	[25.9293,13.0391,8.6539]	0.1306	[0.2356;0.5544;0.5999]	[0,-1.4901e-08,1.0000]	[0.9988,-0.0485,-7.2301e-10]	[0.0485,0.9988,1.4884e-08]
27	10086x3 double	[25.9730,12.5437,9.2509]	0.0204	[0.1385;0.1471;0.9826]	[0.0144,0.7123,-0.7017]	[0.9950,-0.0799,-0.0606]	[0.0144,0.7123,-0.7017]

All_members

Figure 88 Members' part cluster geometrical features database

Merging clusters based on their geometrical features

The merging step uses the information gathered in the geometrical features matrix (Fig. 88) to locate clusters belonging to the same member.

The merging algorithm behind the merging process works on the basis of search criteria applied to each cluster in the analyzed data set. For every cluster C_i in a given slice S_j, the nearest neighboring clusters C_a and C_b are found in the neighboring slices above and below(S_{j+1}, S_{j-1}) slice S_j. The neighboring clusters are found based on the distance of clusters C_i center and centers of clusters in slices S_{j+1}, S_{j-1} using KNN algorithm, as shown in Fig. 89].
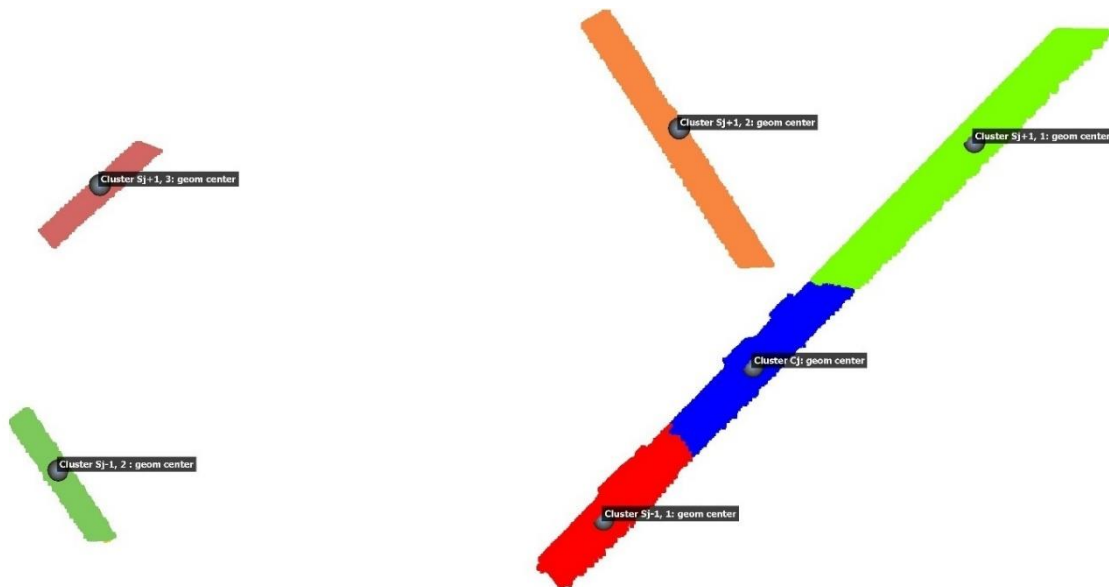
Figure 89 KNN algorithm applied to members' part clusters

Additionally, geometrical filtering criteria are implemented to assure the merged cluster belong to the same member. Two geometrical conditions are defined:

- Cross-sectional area difference
- Point to vector distance

Cross-sectional area difference

For the first geometrical criteria, the absolute difference between cross-sectional areas of the current cluster C_i and searched clusters, either C_a or C_b, is calculated and compared to a predefined condition as follows:

$$\left| A_{x-section,Ci} - A_{x-section,Ca\ or\ Cb} \right| < 0.25 * A_{x-section,Ci}$$

Equation 9

Indicating a relative difference has to be smaller than 25% of the cross-sectional area of the current cluster.

Point to vector distance

The second geometrical criteria detects if the searched clusters C_a or C_b centers lays in a close distance of the longitudinal direction vector $\overrightarrow{V_{N3}}$ of the current cluster C_j, enabling to confirm if the searched clusters belong to the same member.
The computation of the point to vector distance is based on the cross product of two vectors, Fig. 90.
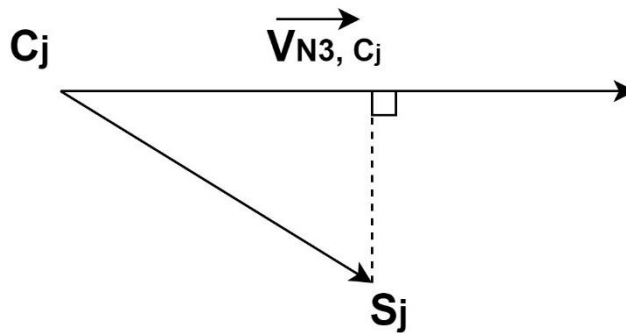
Figure 90 Point to vector distance

The geometrical condition for the distance of the center point of searched clusters to direction vector of the current cluster is given below:

$$\frac{\left| \overrightarrow{V_{N3,Ci}} \times \overrightarrow{C_i C_{a\ or\ b}} \right|}{\left| V_{N3,Ci} \right|} < 0.1 * Slice\ thickness$$

Equation 10

The condition filters out searched clusters with their center distant from the direction vector further than 10% of the slice thickness. The slice thickness has been assumed in the region slicing sub-step as 60cm.

The output of the merging sub-step is a point cloud with combined member parts clusters and leftover clusters, which were filtered out during the process and did not succeed to join any member cluster. Fig. 91 depicts the data set after the merging sub step.
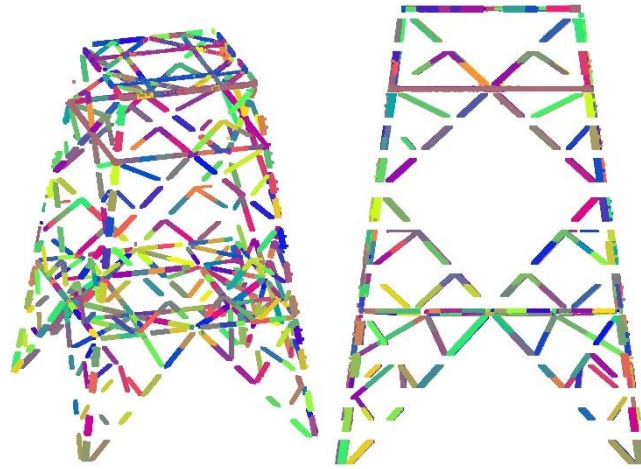
Figure 91 Results of the members merging step

Arranging un-merged clusters

Among the remaining clusters resulting from the previous sub-step two different types can be identified and divided into groups. The majority of the un-merged clusters are the ones representing connection regions of the steel structure, where multiple members intersect and their computed geometrical features did not fit to any of the connected members. Fig. 92 depicts an un-merged connection region cluster.
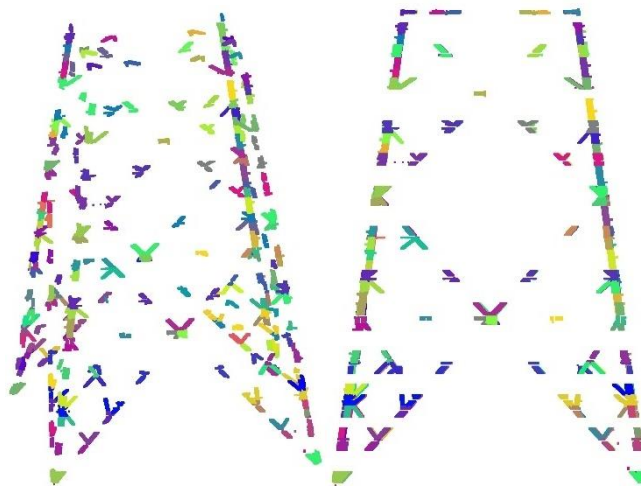
Figure 92 Un-merged connection region clusters

The other type of un-merged clusters occurs only in the in-between horizontal bracing regions where entire horizontal members were clustered in a single slice, as shown in Fig. 93.
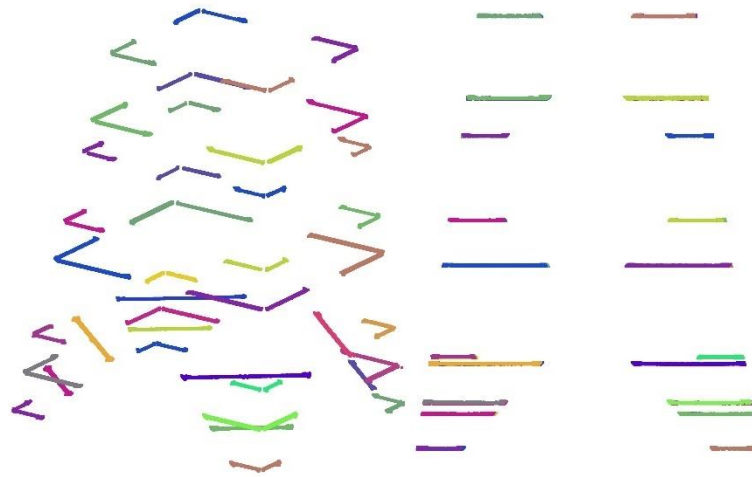
Figure 93 un-merged horizontal bracings

Those un-merged clusters represent two perpendicular horizontal members and not a part of a member therefore they were not combined with other clusters in the previous step.

The two types of occurring un-merged clusters can be easily distinguished based on their geometrical features. Dimensions for the connection clusters bounding box resemble an even edge length cuboid when the horizontal clusters bounding box have dominant edges length in the horizontal plane. Using given characteristics, all un-merged clusters were defined in one of the two groups, Fig. 94.
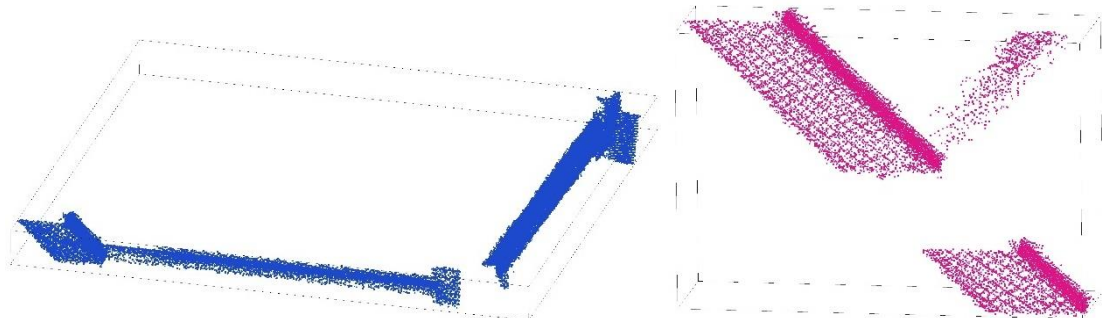
Figure 94 Minimum bounding box of the two types of un-merged clusters

Extraction of single horizontal members
The un-merged horizontal cluster require further segmentation to isolate each horizontal member. The approach for separating the horizontal members inside the cluster is based on KDE applied for X and Y coordinate of the clusters local coordinate system defined as follows, given in Fig. 95.
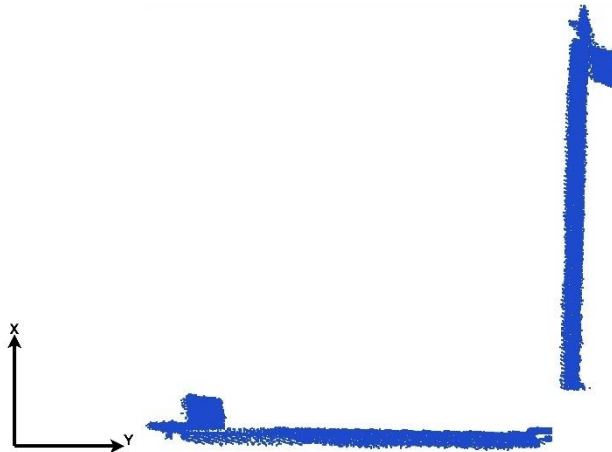
Figure 95 Local coordinate for un-merged bracing clusters

Generating KDE along the two vertical directions of the bounding box allows to detect two peaks representing the location of the members along the predefined coordinates. A visual representation is given in Fig. 96. The horizontal member extraction is analogical to the method applied for horizontal bracing regions extraction in step I (3.6.1) of the script.
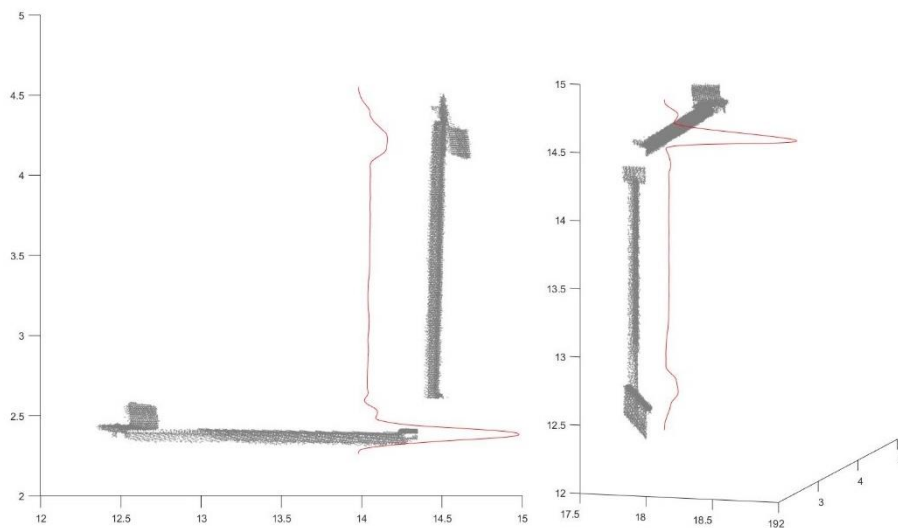
Figure 96 KDE function applied along X and Y local coordinate of the un-merged cluster bracing

The segmentation result is depicted in Fig. 97.
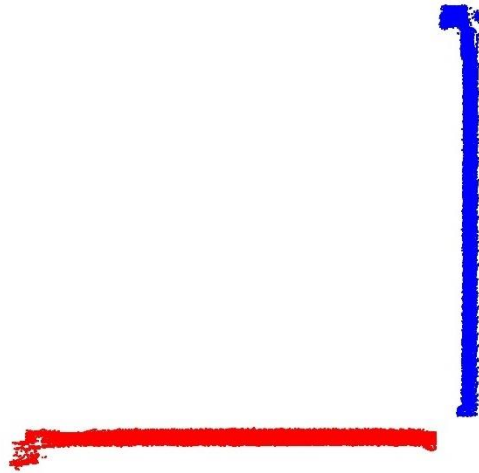
Figure 97 Segmented bracing members

The remaining points from the un-merged horizontal clusters are re-defined as connection region cluster and will be utilized in the following steps.

Extending merged clusters with region growing

The extracted point cloud data for each member, segmented in the previous steps does not depict the joint to joint length of the member. At the current stage, the extracted members parts depict the Section in between the connections, excluding the joint region where members meet. Fig. 98 depicts the extracted member at the current stage.
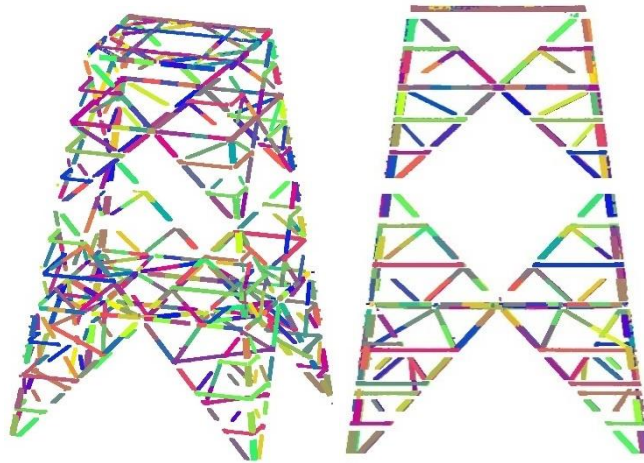
Figure 98 Extracted members prior to the extension step

To obtain the full length member from the data set, an additional step is applied during the member extraction. In this step, the region of the clustered point cloud data is extended along its longitudinal direction, Fig. 99.
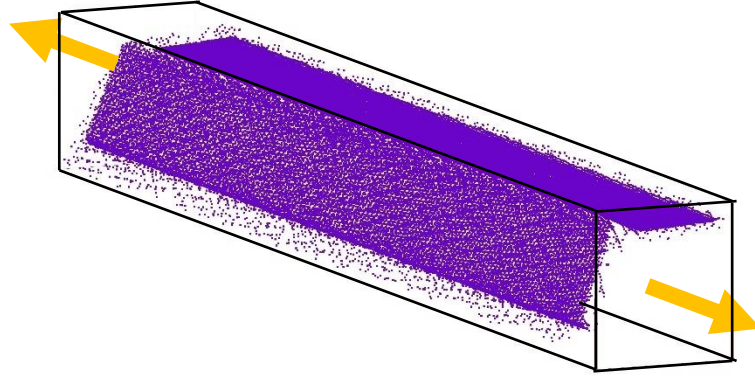
Figure 99. Members extension direction

The region extension method applied in the script is based on the region growing algorithm described in Section 2.3.2. Member regions are iteratively extended. After every extension step, members geometrical properties are re-computed and compared with members properties before the extension. Every member is extended until no substantial increase in the cross-Sectional area $A_{x-section}$ is present. Additionally, the point to vector distance between the new geometrical center C_i and the directional vector $\overrightarrow{V_{N3,\ i-1}}$ of the previous iteration bounding box is checked. The boundary conditions for both checks are defined below:

- $abs\big(A_{x-section,Ci} - A_{x-section,Ci-1}\big) < 0.15 * A_{x-section,Ci-1}$

Equation 11

- $\dfrac{\left|\overrightarrow{V_{N3,Ci-1}} \times \overrightarrow{C_iC_{i-1}}\right|}{\left|\overrightarrow{V_{N3,Ci-1}}\right|} < 0.05 * Slice\ thickness$

Equation 12

Applying the region growing algorithm allows to extract the full joint to joint length of the member. A comparison of a member cluster before and after region growing is depicted in Fig. 100.
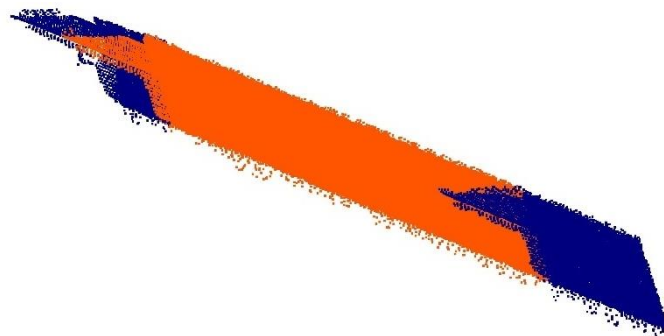
Figure 100 Extended member0(blue part) compared to initial member cluster(orange)

The region growing based members extension was applied to all segmented members. The final results of member extraction is presented in Fig. 101.
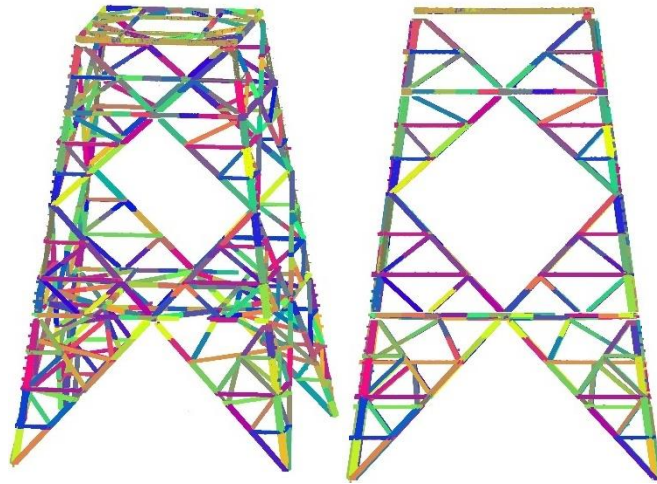
Figure 101 Results of member extension step

3.7.3   Step III: Member level

In the final step of the model generation script extracted members point clouds were processed in order to define the system lines for each member using the line generating script described in (3.2.2).

For the generated geometrical model, the regression curve used to fit a polyline to the discretized points was a fourth order polynomial. The order of the regression function is following the order of the deformation equation of a beam under uniformly distributed load allowing to depict the flexural buckling behavior of the member.

$$w(x) = \frac{5L^4}{384EI}$$

Equation 13

Fig. 103 presents polylines fitted to the corner points of segmented members.
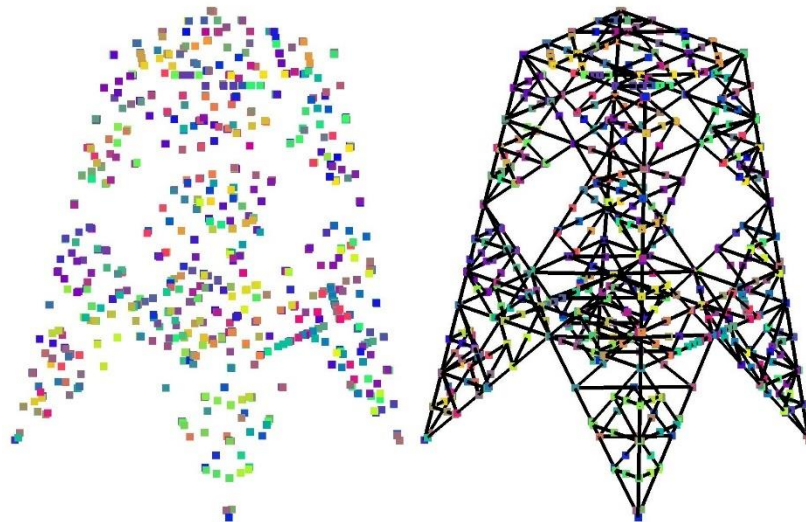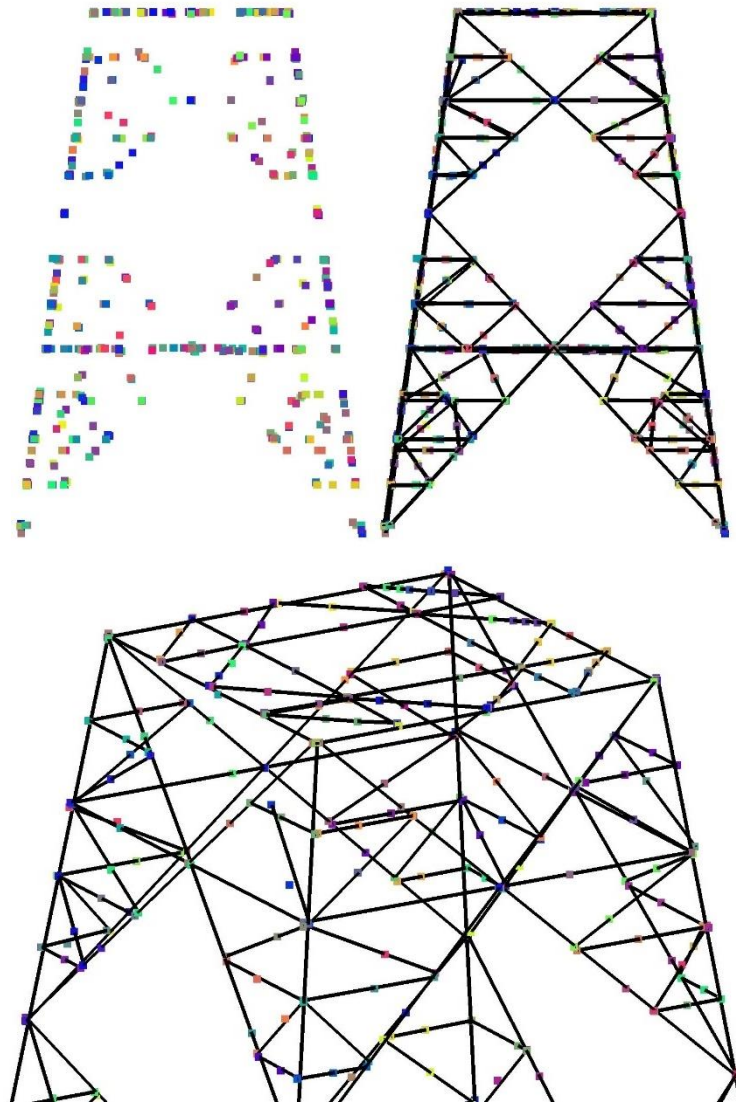
Figure 102 Results of member polyline generation script

The geometrical information extracted from the point cloud data using the script allows to capture the deformation shape along the longitudinal dimension of a member, depicting global behavior caused by bending. Cross-sectional features like torsion or local imperfections of flanges are not captured during the model generation, therefore were not included in the final geometrical model based on the in-situ state of the tower.

The final model generated using the model generating script is presented in Fig. 103.
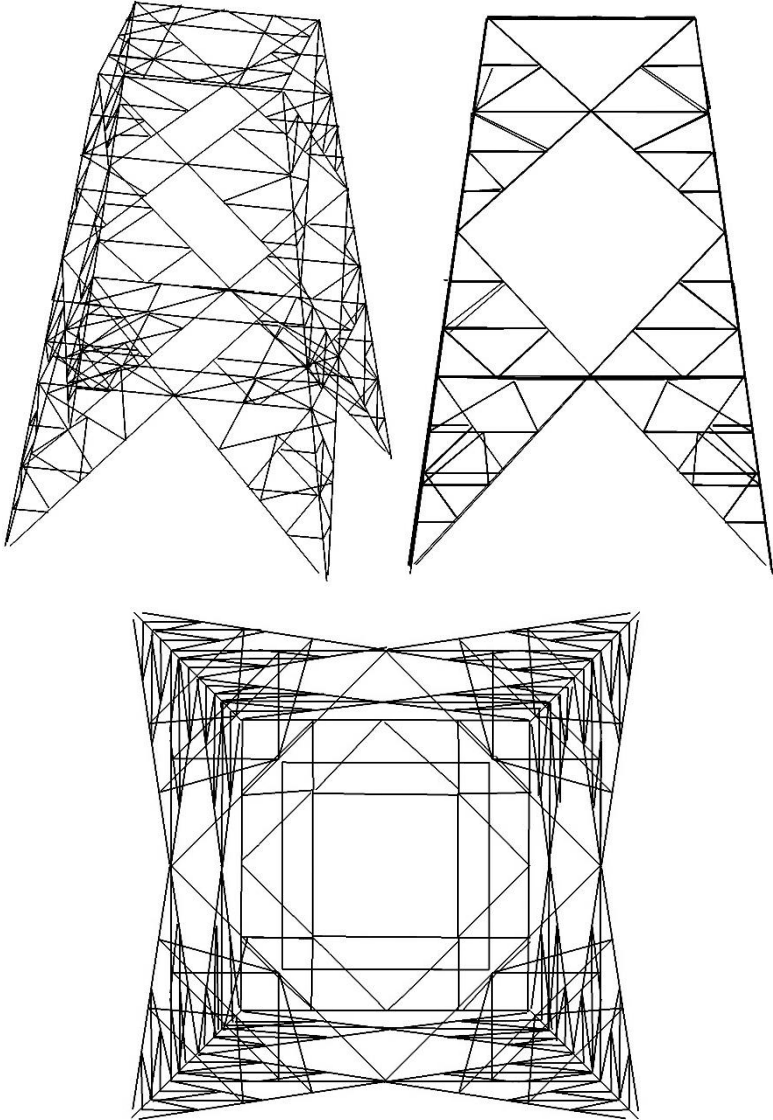
Figure 103 Final polyline model of the analyzed lattice tower segment

created using model generation script based on the terrestrial LiDAR point cloud

3.8   Comparison of point cloud based geometric models with the idealized model based on design documentation

In order to better understand the differences between all the geometrical models generated in the thesis, a geometrical comparison between the idealized reference line model and both point cloud based line models was carried out. All models are defined by end-points and system lines. For the purpose of the geometrical comparison, the end-points are referred to as nodes. For the three generated line models different complexity levels of deformation inclusion have been introduced:

Idealized line model:

The idealized reference model based on design documentation has no geometrical imperfections and deformations included. Members in the analyzed model are discretized as first order polynomials with 2 nodes defined at both ends. Fig. 104 depicts the member discretization for the idealized model.
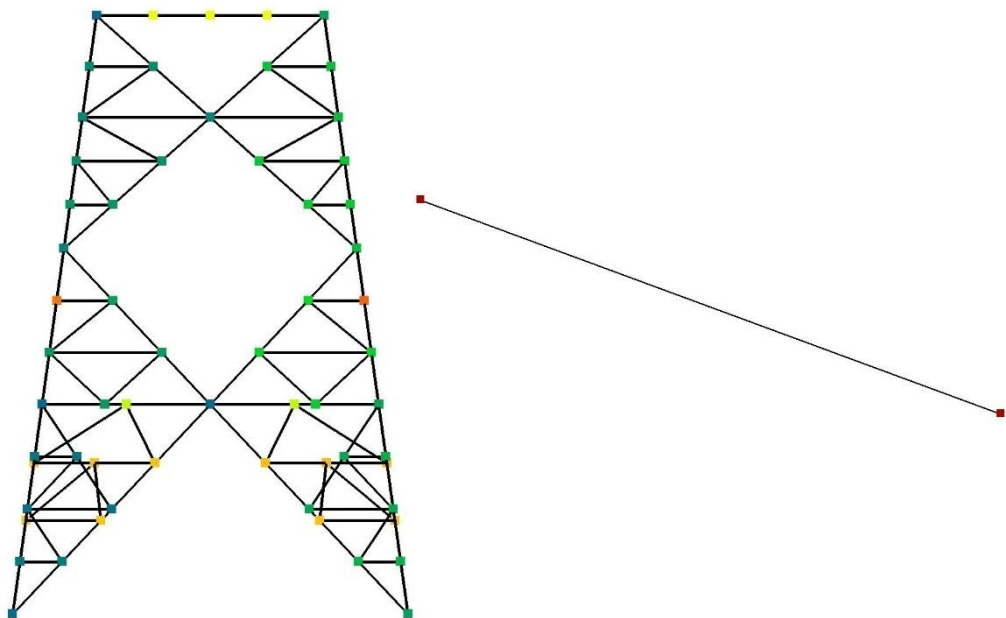
Figure 104 Idealized model discretization

The connections are defined as a single node. This type of a connection definition is an approximation commonly utilized in the current state of the art FEA modelling methods used for lattice structures. The idealized model is presented in Fig. 105.
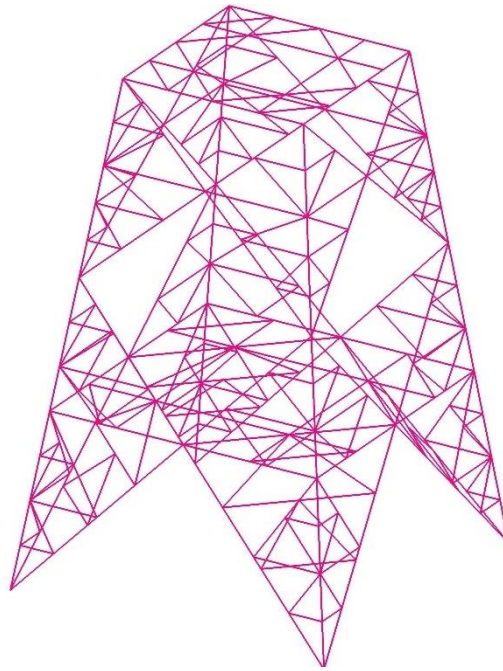
Figure 105 Idealized model

Aerial LiDAR point cloud based line model:

The aerial LiDAR point cloud based line model was generated using the vectorization method described in Section 3.5. The aerial point cloud based model includes real life global deviations of the structure. Lengths and the positioning of a member in the in-situ structure is included in the model contrary to the idealized model for which those are based on the design documentation. An example of a real life global deviations compared with the idealized model is depicted in Fig. 106.
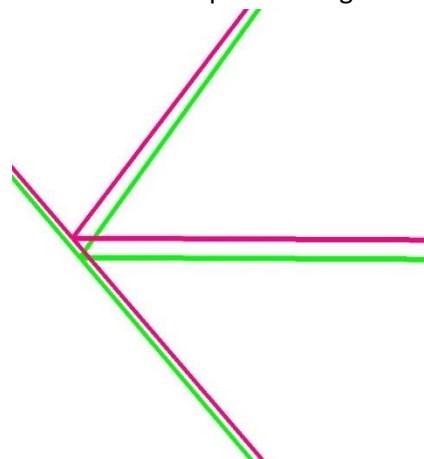
Figure 106 Difference between aerial point cloud based model

and idealized model

On the member level, identical definition as for the idealized model has been assumed. All members are defined as first order polynomials, connected with other members in a single node connection.

Due to the simplification of the node connection the real lengths and positioning of members is less accurate than in the following line model generated using the script. The approximated node definition forces the members to be extruded and the end points of each member repositioned to a single node for each connection. The node approximation phenomena is depicted in Fig. 107.
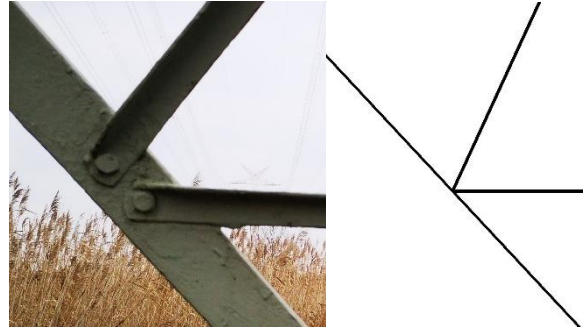
Figure 107 Node approximation phenomena

The Aerial LiDAR point cloud based model is depicted in Fig. 108.
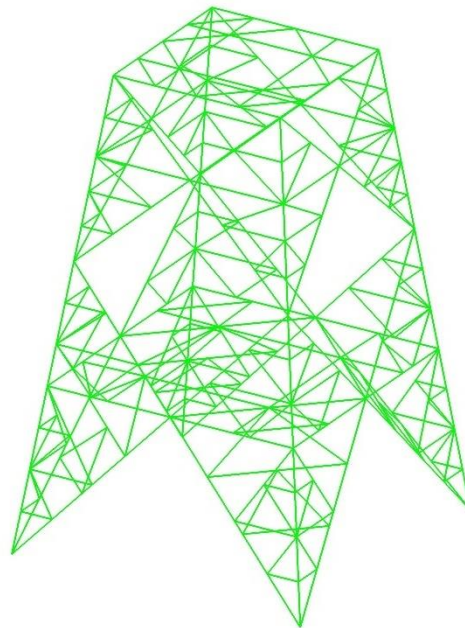
Figure 108 Aerial LiDAR point cloud based line model

Terrestrial point cloud based line model:

The terrestrial LiDAR point cloud based line model was created using the script developed for the purpose of this work and defined in point 3.6. The model depicts deformations present in the in-situ structure in the most reliable way compared with the previously described line models.

The real life global geometry of the analyzed tower segment, captured in the aerial point cloud based model, is also included in the this model. What is more, the in-situ based length and positioning for all members is captured more accurately than in the previous model due to higher point cloud quality and a more refined model generation procedure based on point cloud segmentation and processing rather than the manual point picking method of the vectorization approach.

The next difference of the model generated with the script compared with the other two models is the system line definition for the members. In order to capture the deformed shape of a member, a fourth order polynomial curve is used for members' system line definition. A comparison of a deformed and idealized system line is depicted in Fig. 109.
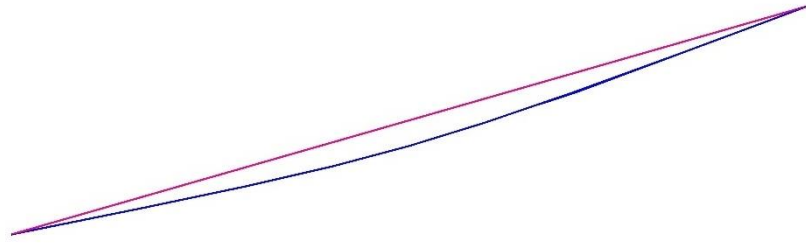
Figure 109 Deformed polyline(blue) and idealized line model(pink)

The final alteration to the geometrical model is the connection definition. Extracting the accurate joint to joint lengths and positioning of members allows to include the eccentricity of the connection. Fig. 110 depicts the in-situ connection example from the analyzed tower segment.
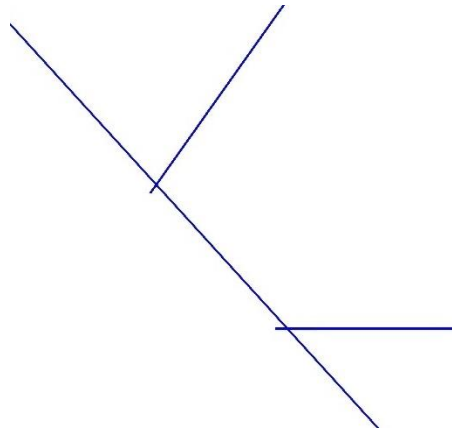
Figure 110 In-situ based eccentricity included

in the terrestrial LiDAR point cloud based model

Due to the inclusion of in-situ eccentricity to connections, no additional approximations in the connection areas are required in the geometrical line model. The definition for the connections will be defined during the FEA model generation step described in chapter 4.

The Terrestrial LiDAR point cloud based model is depicted in Fig. 111.
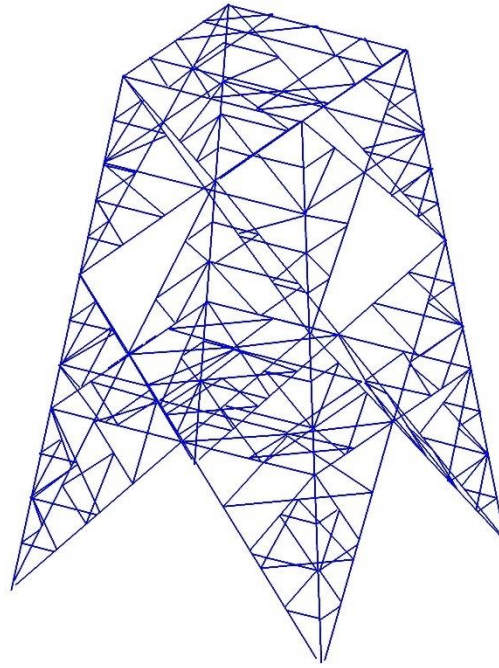
Figure 111 Terrestrial LiDAR point cloud based polyline model

The geometrical comparison process

The geometrical comparison has been conducted on two levels. A global comparison of the entire analyzed tower segment and a local comparison of each member.

The global comparison enabled to capture deviations of the entire analyzed tower segment. Allowing to investigate the global deformation shape of the in-situ tower which will help to interpret the finite element analysis results.

The main purpose of the local comparisons was to identify members with large deviations from the design documentation by measuring the differences in lengths and deformation magnitudes of the point cloud based models compared to the idealized model.

In order to allow for a controlled measurement setup, all line models were discretized by a set of reference points per member. For idealized and aerial data based models, where members were defined as first order polynomials the reference points are located at the ends of each member. For the terrestrial point cloud based model generated using the script, an additional reference point at the position of the local extreme point of the curve has been added. By defining the third point at the extreme value of the polynomial information regarding maximum members deformation could be captured.

The line models discretized with the reference points are presented in Fig. 112.
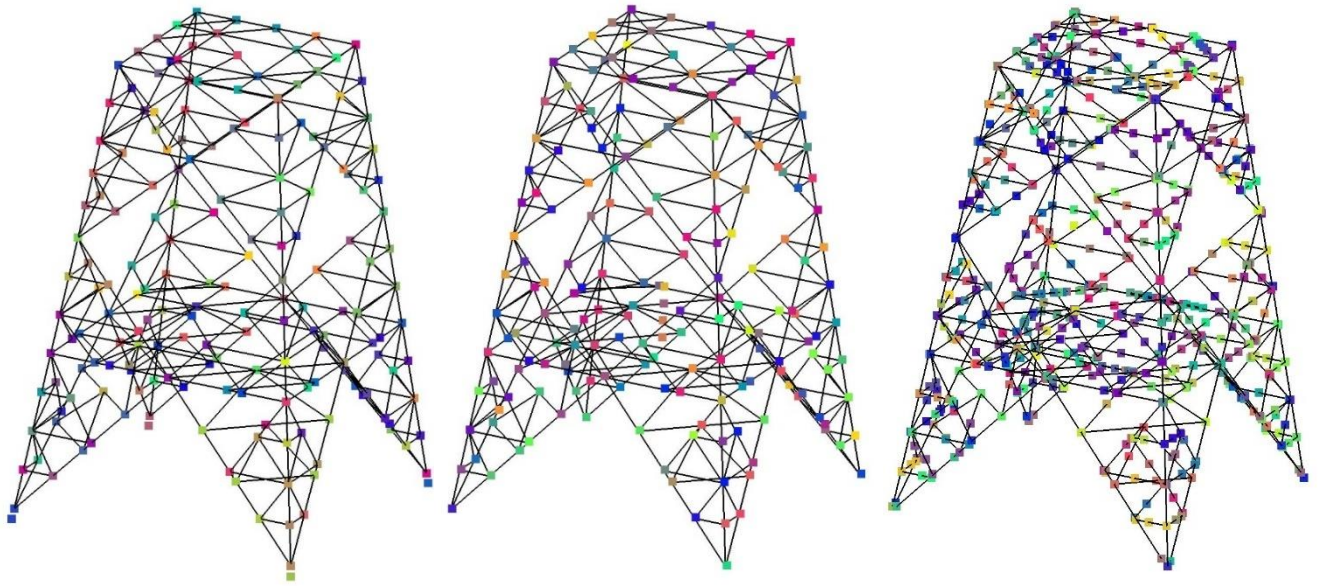
Figure 112 All discretized line models. Idealized(left), Aerial point cloud(middle) and Terrestrial point cloud(right)

Global comparison

After all models have been discretized by the reference points, the point cloud based models are compared with the idealized model. The comparison at global level is conducted by computing the node deviations between the point cloud based models and the idealized model. For every reference point of each member, the deviation is calculated as the distance between two corresponding points of the compared models.

The deviation analysis was carried for the two pair of models:

- Terrestrial point cloud based model to idealized model
- Aerial point cloud based model to idealized model

Fig. 113 presents the graphical interpretation of global comparison on an example.
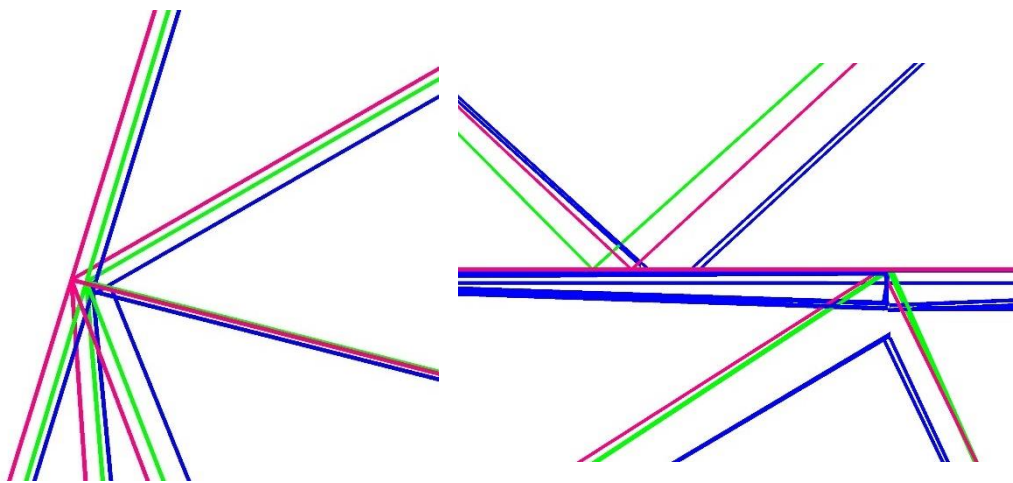
Figure 113 Graphical comparison between all line models. Idealized(pink), Aerial point cloud(green) and Terrestrial point cloud(blue)

For the global comparison, the deformed point cloud based models and the idealized model are defined at the same cartesian coordinate system. All models are aligned based on the centroidal axis running through the geometrical center of the analyzed tower segment.

Considering the lack of symmetry of the point cloud based models caused by the included deformations and imperfections, the location of the centroidal axis was defined based on the normal vector of the mid-plane of the lowest horizontal bracing. The vector is running through the geometrical center of the horizontal bracing as depicted in Fig. 114.
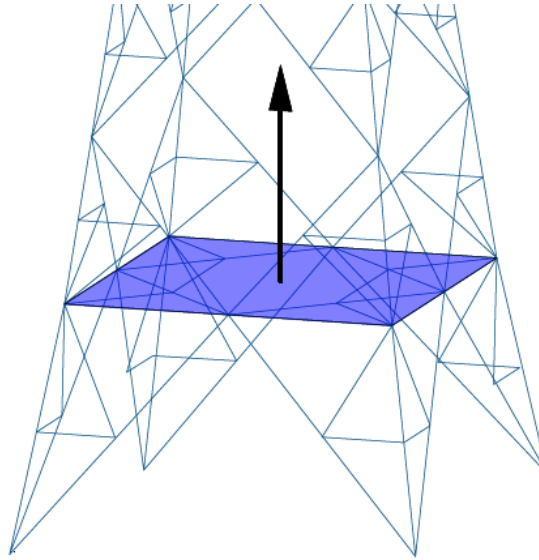
Figure 114 Local coordinate alignment vector

Defining reference vectors based on the bottom bracing allowed to minimize the impact of deviations on the alignment, considering negligible tilt of the bottom bracing of the in-situ structure (tilting of the bottom bracing is less then $\alpha=0.2°$, were α is the angle between plane normal to Z+ global vector and the bottom bracing plane of the in-situ structure).After alignment, the nodal deviation between all models was computed.

The results of the comparison will be presented in chapter 5.

Local comparison

For the local comparison, each system line of a member for both point cloud based models have been compared with the corresponding system line of the member from the idealized model. Taking into account that the aerial point cloud based model's and the idealized model's system lines are defined as first order polynomials the local comparison allowed to compute only the differences in members' lengths. When it comes to the terrestrial point cloud based model, for which a fourth order polynomial has been assumed to represent system lines, additionally to the differences in lengths the maximum deformation of each member was computed. Fig. 115 depicts members' maximum deformation definition in the terrestrial point cloud based model.
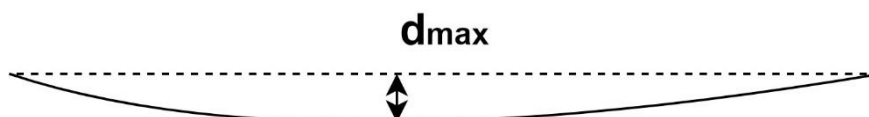
Figure 115 Maximum deformation definition

The length comparison has been normalized and computed by the following equation:

$$\Delta L_{Normalized} = \frac{L_{member, \ point \ cloud \ based \ model} - L_{member, \ idealzied \ model}}{L_{member, \ idealzied \ model}}$$

<div align="right">*Equation 14*</div>

The maximum deformation for each member of the terrestrial point cloud based model has been computed as a point to line distance d_{max}, depicted in Fig. 115.

The results of the comparison will be presented in chapter 5.

3.9 CAD to FEA CAD model preparation for FEA analysis

In order to conduct the finite element analysis, the polyline CAD models required a cross-section assignment before being imported to the FEA software. The types of cross-sections utilized for the analyzed tower are identical for both, the idealized model based on design documentation and the model representing the in-situ structure based on the point cloud data.

The cross-section dimensions are based on design documentation provided by the company [25]. Fig. 116 presents the assigned cross-section depicted in the documentation.
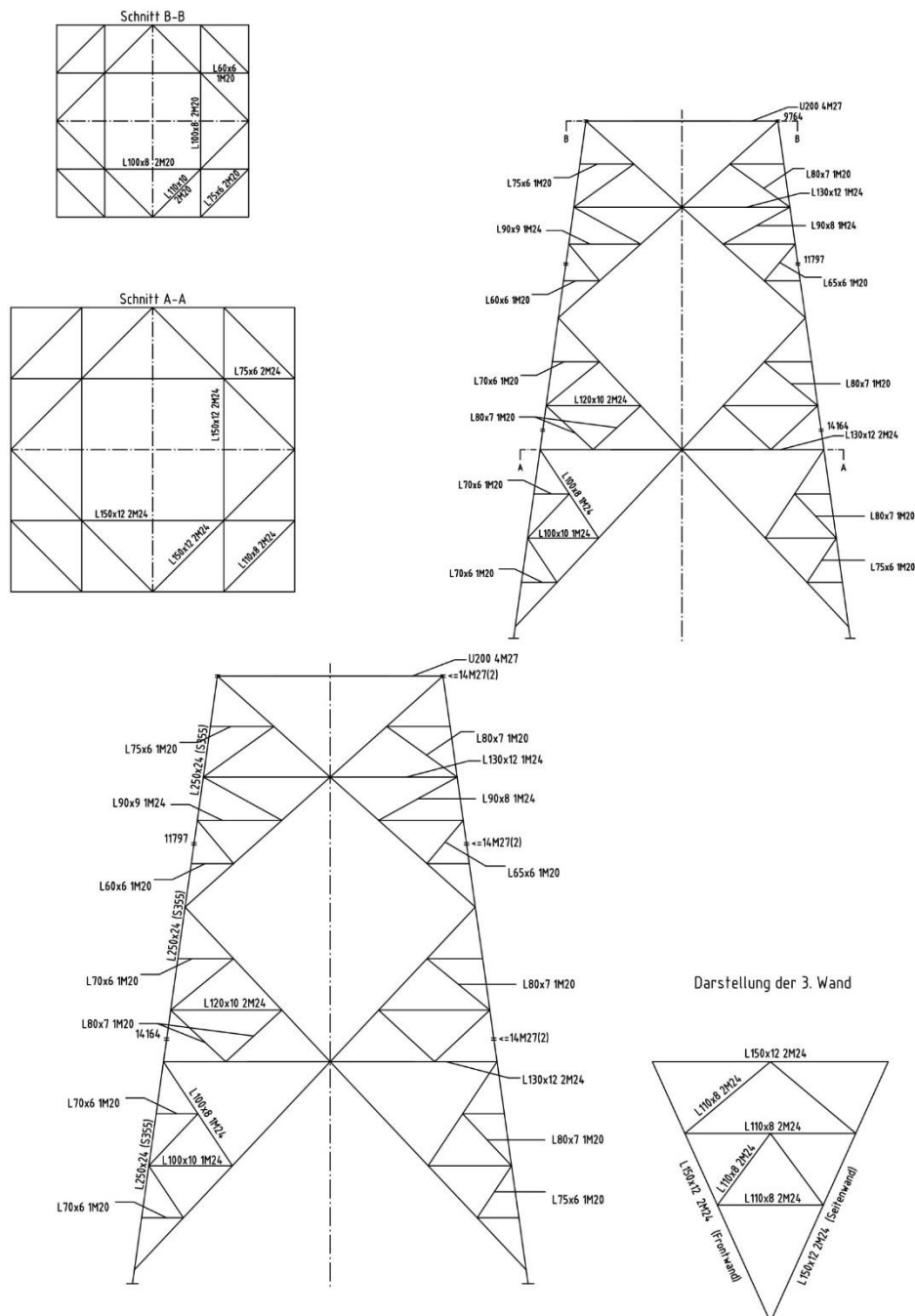
Figure 116 Cross-sections used on the analyzed lattice tower segment based on design documentation

The assignment of cross-sections was conducted using sweep function in AutoCAD. The cross-section orientation chosen for the assignment is based on the deformation direction captured with the fitted

polylines. The Z - Z minor axis of the L-shaped profile follows the deformation direction as follows Fig. 117.
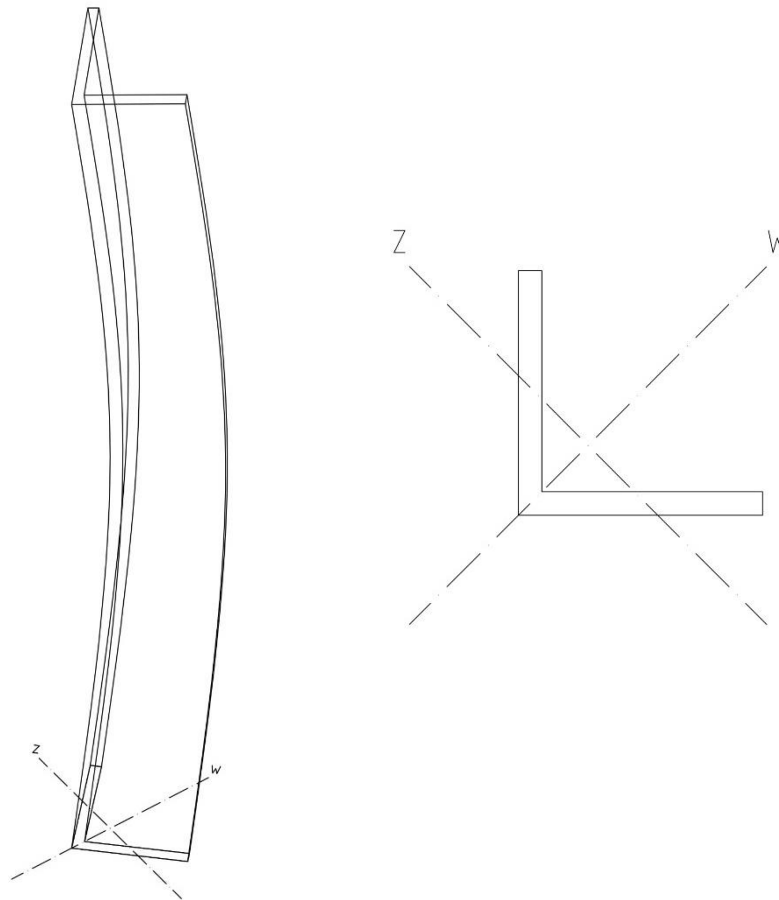
Figure 117 Deformation direction applied to the deformed model

After assigning cross-sections to all the members, the model generating process in finalized. In the next chapter the finite element analysis process carried for both models will be described.

4 Finite Element Analysis

This chapter focuses on the finite element analysis carried out for two different models. The first model is based on the idealized geometrical model for which the initial imperfections will be added during the analysis. The second model uses the geometrical model generated with the script developed for the purpose of this work. Imperfections in the second model are included in the geometrical model and are based on the in-situ state of the analyzed lattice tower segment.

Section 4.1 introduces the reader to the FEA procedure carried in this study. Boundary conditions and material properties are presented in Section 4.2 and 4.3 accordingly. Section 4.4 described the mesh fitting procedure. Section 4.5 focuses on geometrical imperfections included in both idealized and point cloud based models. Loads applied to all analyzed models are presented in Section 4.6. In the last Section the type of the finite element analysis and all its parameters are defined.

4.1 Finite Element Analysis

Conducting the finite element analysis allows to answer the research questions by investigating the impact of included in-situ imperfections in the point cloud based model. The differences between the FEA results for both the idealized model based on design documentation and the model with in-situ based deformations will be analyzed and presented in chapter 5.

For the analysis, a second order non-linear approach was chosen, allowing to define the ultimate resistance for both models and evaluate the impact of in-situ imperfections included in the model based on the real structure on the resistance of the analyzed steel lattice tower segment.

To understand the problem in depth, the analysis has been divided into two levels- a member analysis and a global analysis. The global analysis focuses on the response of the analyzed tower segment to a load case based on an ultimate limit state critical load combination defined in the design documentation[25]. The member analysis was carried out on isolated members picked during the geometrical comparison in Section 3.7. The isolated members were loaded by axial load to study the L shaped profiles buckling resistance under the given load.

For both models only geometrical non-linear effects have been included in the analysis, no material non-linear effects were used. By limiting the sources of non-linearity to pure geometrical non-linear effects, the results of the analysis are easier to interpret and capture the difference between both imperfections' application methods.

The FEA has been computed in Abaqus FEA 2019 software.

In the next Sections a detailed description on the FEA assumptions and definitions utilized during the analysis will be explained.

4.2 Boundary conditions

The applied boundary conditions are representing the members connections in the analyzed structure in a approximated way. The decision on the boundary conditions was based on the level of detail in the previously generated geometrical model and modelling restrictions limiting the choice of applicable constraints. In the analyzed model no connection details like end plates, bolts or welds were modeled during the geometrical model generation. Therefore, the boundary conditions for members are defined as mechanical constraints along the edges at the member's ends. For both member and global analysis the same type of boundary condition has been utilized.

4.2.1 Member analysis

During the member analysis all analyzed specimens were constrained as a simply supported beam, fixing the translation in x, y at both ends, z direction at one end and allowing for rotation. The mechanical scheme depicting the boundary conditions is given in Fig. 118.
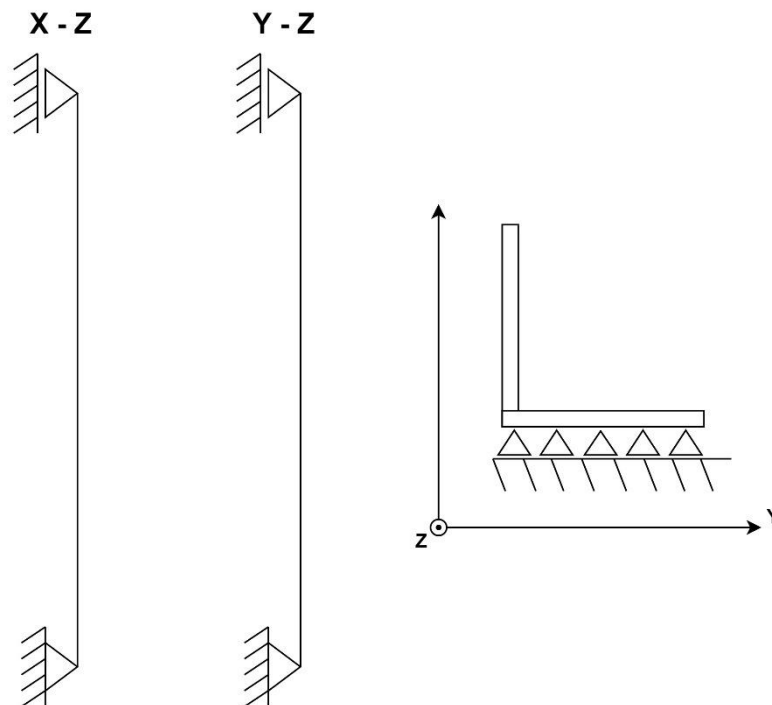
Figure 118 Mechanical scheme for the local analysis

For the in-situ structure, every L shaped member in the analyzed tower segment is joined with other members by a single leg bolted connection. The example of such a connection is provided in Fig. 119.

Figure 119 Single leg bolted connection

This type of connection is frequently utilized for steel lattice structures with L-shaped profiles. To simulate such a connection, a one leg's constraint along the edge has been assumed. The defined boundary condition is constraining translation at both ends in directions perpendicular to the cross-section and along longitudinal direction at a single end. No rotation constraints were utilized. Fig. 120 depicts the boundary conditions utilized for the member analysis.
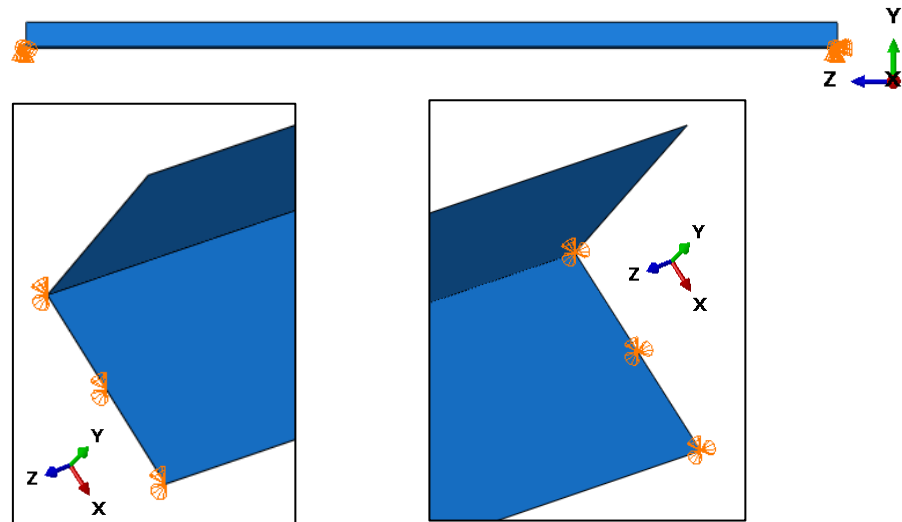
Figure 120 Boundary conditions- member analysis

4.2.2 Global analysis

Following the member analysis, the boundary conditions for the entire analyzed tower segment depict the one leg's connection. The boundary conditions used in the FEA model are a simplification of the real connection encountered in the analyzed lattice tower. The approximated connection type, applied in the FEA model, commonly appears in the structural engineering practice [26] therefore the decision to apply this type of constraint was made.

For the members' connection a hinge constraint has been utilized. All members are connected along one leg's edge using pin type multi-point constraint (MPC) from Abaqus. The connection constraints translation in all directions allowing for free rotation. Fig. 121 presents applied MPC in the global analysis model.
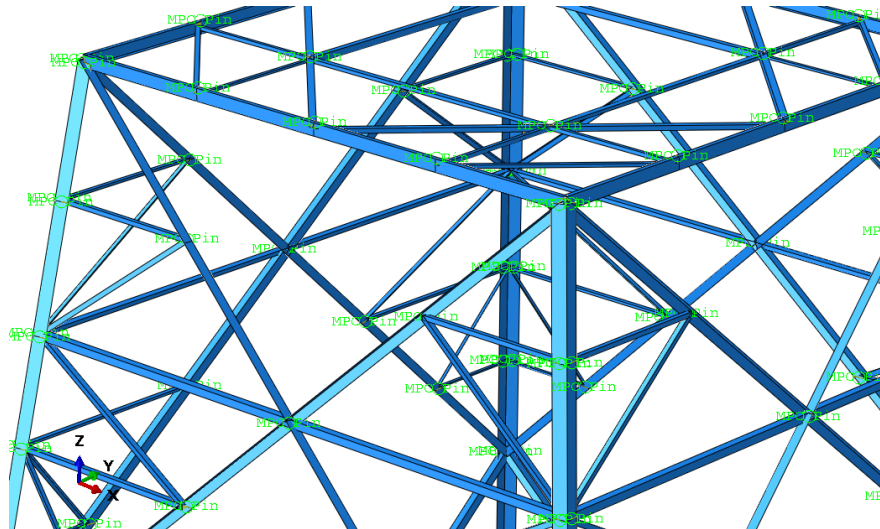
Figure 121 MPCs utilized in the global analysis model

For the purpose of the study, the support conditions have been assumed as fully fixed with no rotation and translation allowance in all directions. The assumption on fixed support conditions is based on the in-situ examination of the analyzed tower segment for which the main corners are embedded in concrete foundation heads. Fig. 122 depicts the foundation conditions of the in-situ tower.

Figure 122 Foundation condition of the in-situ tower

The support conditions were applied to the main corner members edges at the foundation level as depicted in Fig. 123.
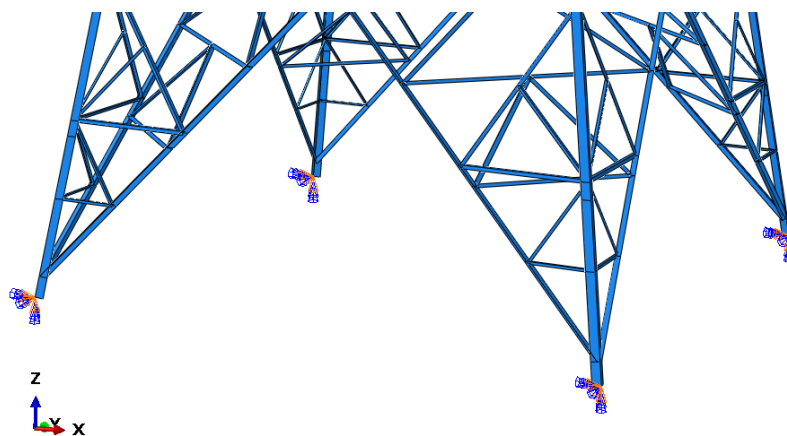
Figure 123 Support conditions in the global analysis model

4.3   Material properties

Considering the design documentation provided by the company [25] was prepared based on the Eurocode standard and the material non-linear effects will not be included in the FEA. The material properties defined in the models are based on the Eurocode EN 1993-1-1 norm [27].

The nominal values of the yield strength f_y and the ultimate strength f_u for structural steel are based on table 3.1 from EN 1993-1-1 [27].

Material coefficients to be adopted in FEA:

- Modulus of elasticity: E =21000 kN/cm^2

- Shear modulus: G = 8100 kN/cm^2

- Poisson's ratio in elastic stage: v=0.3 [-]

4.4   Mesh

4.4.1   Element type

Taking into account that all profiles used in the analyzed structure are thin walled L shaped Sections, the use of shell elements was a preferred approach. Shell elements suit well for thin walled plated structures with one dimension significantly thinner [28]. The use of shell elements allows to analyze members behavior under the influence of the second order analysis with a limited number of elements required. To compare, if solid elements were to be applied for any of the members at least 3 elements along plate thickness had to be applied to obtain similar results compared to a single shell elements. The reason lays behind the degrees of freedom(DOF) defined in the nodes for each element type. When for the solid elements, only 3 displacement DOF's are used, the shell elements used in the finite element model have 6 DOF's with 3 rotations and 3 displacements. The DOF's for the shell elements used in this work are depicted in Fig. 124.
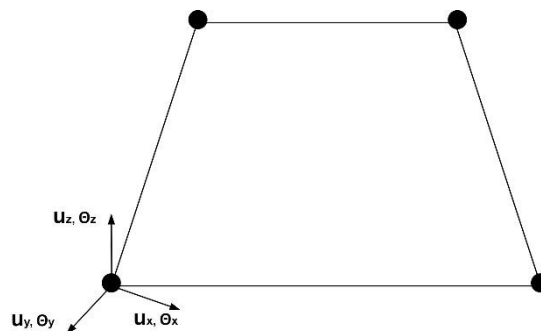
Figure 124 DOF's in shell elements used in the analysis

Considering the amount of elements required to properly model each member of the analyzed structure, the use of solid elements compared to shell elements was not efficient. Solid model would require more computational power with no significant gain on the results of the analysis.

The elements type used in the analysis was a 4-node doubly curved shell element with 4 integration points per element. The elements are labeled as S4 elements in Abaqus FEA software. In order to

prevent the hourglass effect occurrence, no reduced integration elements were used. The hourglass effect causes finite elements to experience an unrealistic deformation mode caused by the excitation of zero-energy degrees of freedom [28]. The visual representation of the phenomena is depicted in [Fig. 125].
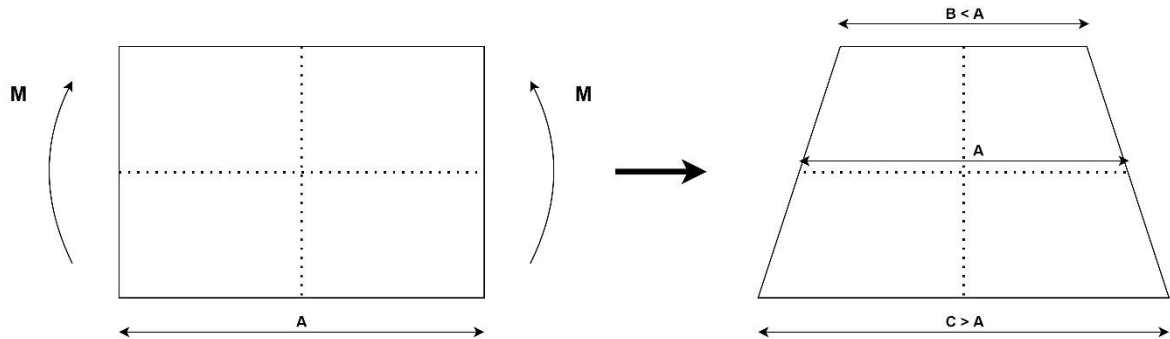
Figure 125 Hourglass effect

4.4.2   Mesh size

The mesh size assigned for the FEA models was based on convergence of the bifurcation analysis results for selected isolated members. The members picked for the bifurcation analysis were the idealized members which later would have been used in the member analysis. For the buckling analysis, fixed boundary conditions along both legs' edges were assumed. Fig. 126 highlight the members for which the analysis has been carried out.
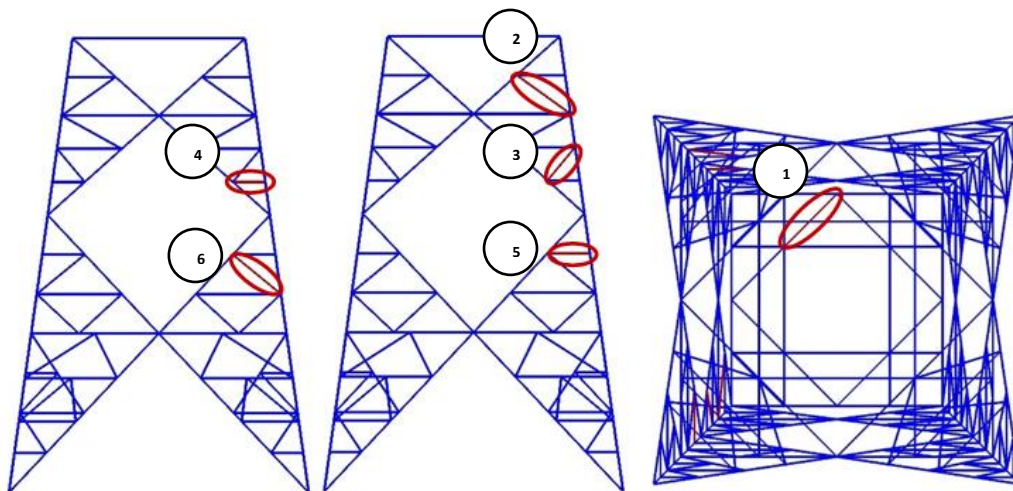
Figure 126 Members(red) used for mesh convergence

For the mesh convergence check performed during the buckling analysis different mesh sizes were tested. The initial mesh size for all the analyzed members was set to 80mm. In the following convergence iterations the size of the elements was divided by half. At each iteration the buckling analysis was performed and the buckling force P_{cr} of the first buckling mode was computed and compared with the results for the previous mesh size. The shape of the first buckling mode for all members under every analyzed mesh size was depicting a torsional-flexural buckling. The example of the buckling shape present for the mesh convergence analysis is depicted in Fig. 127.
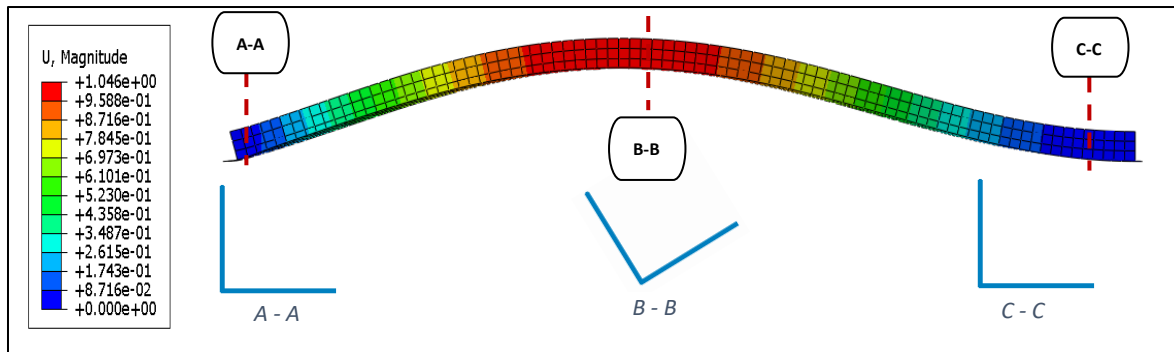
Figure 127 First eigenmode of the bifurcation analysis, mesh convergence

Based on common engineering practice, the convergence criteria for the analysis was assumed to be reached at a level below of 5% difference between the results of subsequent mesh sizes. The relative difference was computed with the following equation:

$$\frac{\text{Pcr}_{i+1} - \text{Pcr}_i}{\text{Pcr}_i} * 100\%$$

Equation 15

Tab. 6 depicts the convergence analysis results for all the analyzed members.

	Member	1		2		3	
		Pcr [kN]	Convergence [%]	Pcr [kN]	Convergence [%]	Pcr [kN]	Convergence [%]
Mesh size [mm]	80	423,42	-	105,32	-	110,34	-
	60	448,19	5,85	111,43	5,80	116,44	5,53
	40	451,71	0,78	112,32	0,80	117,64	1,03
	20	454,59	0,64	112,83	0,45	118,69	0,90
	Member	4		5		6	
		Pcr [kN]	Convergence [%]	Pcr [kN]	Convergence [%]	Pcr [kN]	Convergence [%]
Mesh size [mm]	80	149,53	-	139,89	-	116,96	-
	60	161,40	7,94	146,19	4,51	125,35	7,17
	40	163,44	1,26	147,75	1,07	126,39	0,83
	20	165,02	0,97	148,94	0,81	126,98	0,47

Table 6 Mesh convergence results

As depicted in Tab. 6, for all the analyzed members for the mesh size of 40mm the buckling force P_{cr} is converged. Therefore, the final mesh size for the FEA analysis of all analyzed models was set to 40mm. Fig. 128 depicts the finial mesh size depicted in the analyzed FEA models.
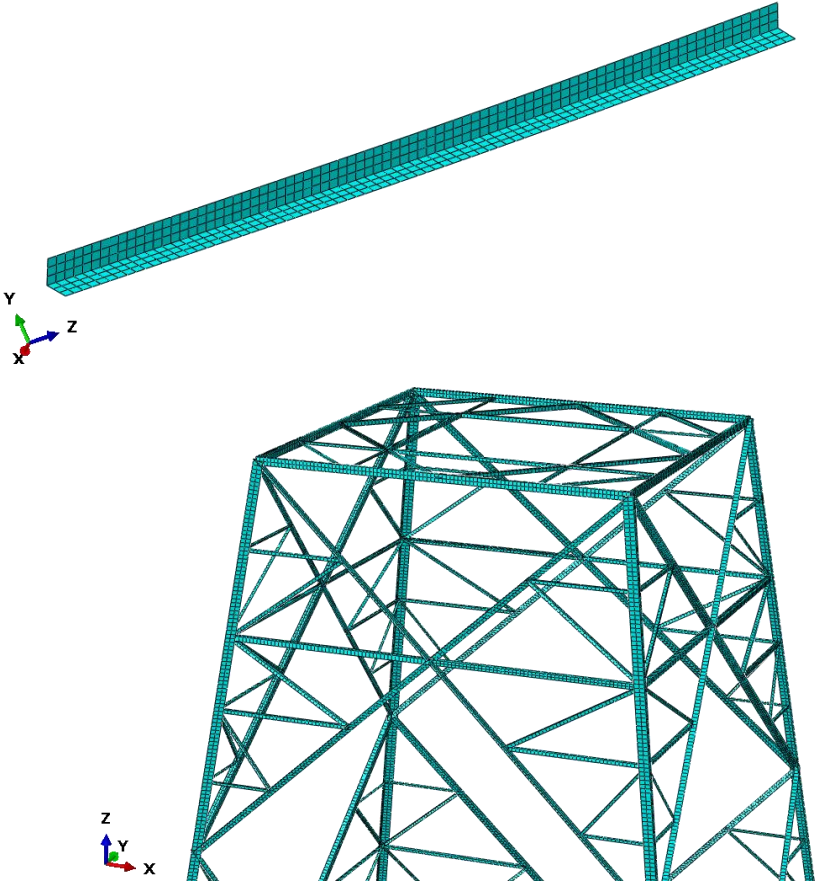
Figure 128 Final mesh applied to both global and local cases

4.5   Geometrical imperfections

For the second order finite element analysis, all analyzed models require an initial imperfection to initiate the non-linear deformation. As described at the beginning of this chapter. The initial imperfection for the model based on the LiDAR point cloud data is included in the geometrical model and represents the in-situ imperfections of the scanned lattice tower. Fig. 129 depicts the deformed FEA model.
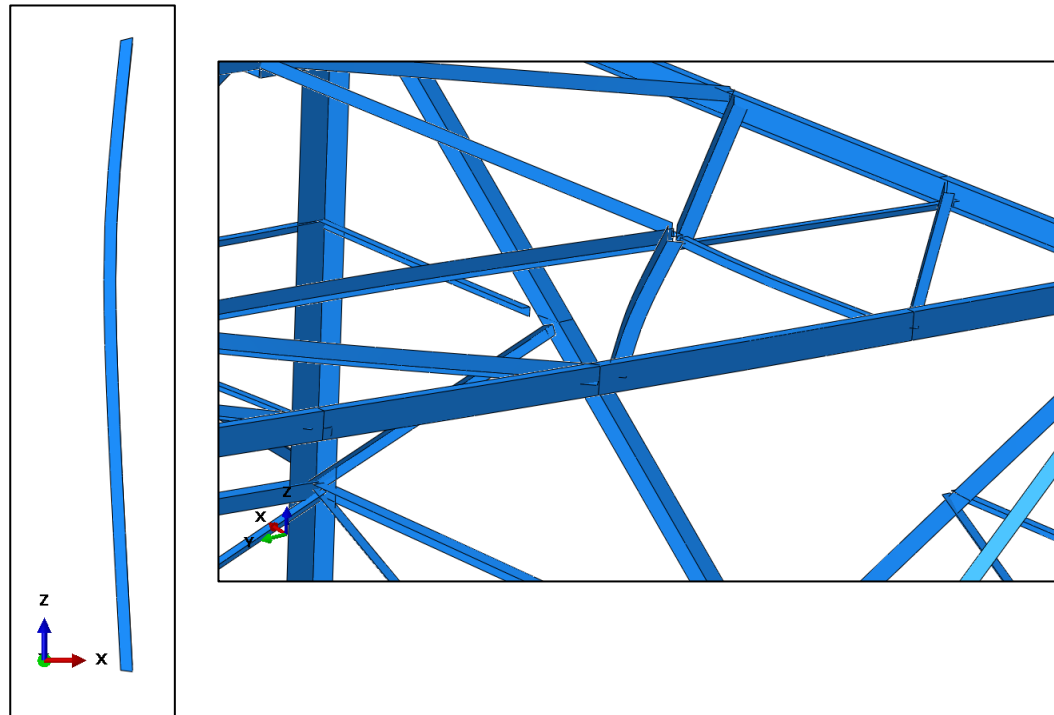
Figure 129 Deformed FEA model based on in-situ captured data

In the idealized model based on design documentation no imperfections were included while generating the geometrical model. Thus, the shape of initial imperfections used in the FEA is based on the first eigenmode of the bifurcation analysis performed on the models. Fig. 130 depicts the 1st eigenmode of the buckling analysis for the idealized model. The magnitude for the imperfection was set to 1mm, allowing to initiate the imperfection without exceeding the elastic deformation range.
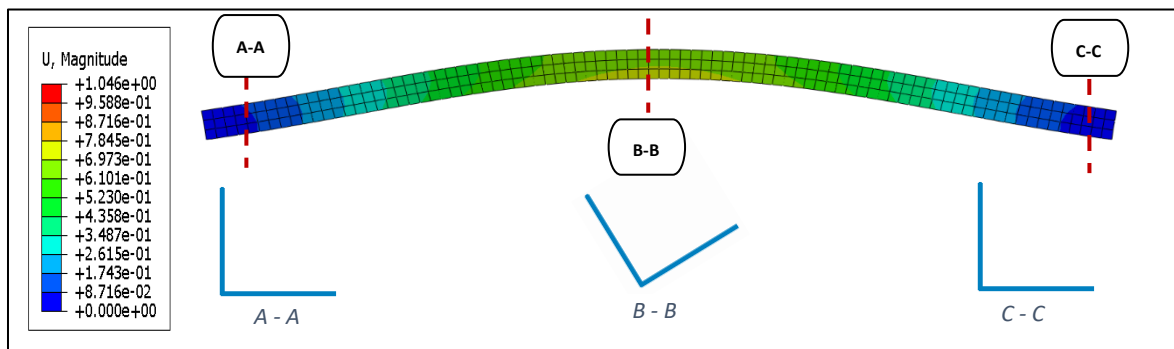
Figure 130 First eigenmode of the buckling analysis of an idealized member. Side view (top), cross-sectional views(bottom)

Depending on geometrical properties, steel members can undergo different buckling phenomena. The L-shaped profiles used in the analyzed tower belong to a opened thin-walled cross-section type which are characterized by a low torsional stiffness, leading to high twisting deformations under torsional loads. Additionally, due to high slenderness ratio many analyzed members are susceptible to flexural buckling [29].

According to [30] the two main failure modes for L-shaped profiles are usually related to a flexural or a torsional-flexural buckling in the ultimate limit state. Fig. 131 depicts the two failure modes for equal leg L-shaped profiles.
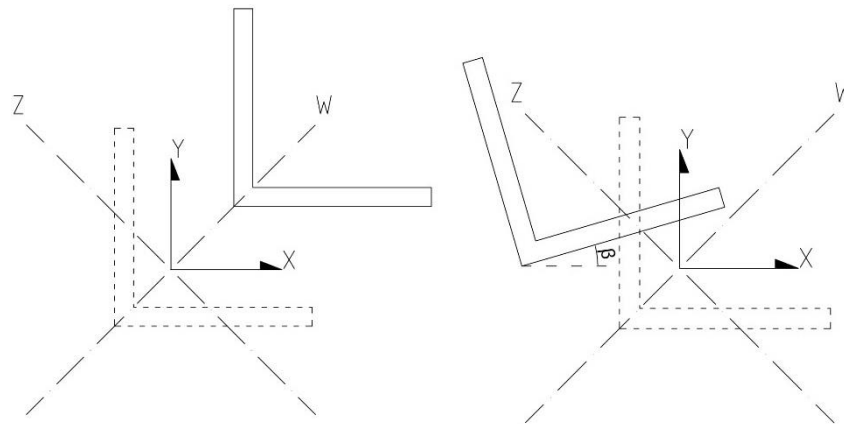
Figure 131 Pure flexural(left) and torsional-flexural(right) buckling failure modes

The pure flexural buckling mode occurs as a rigid-body displacement $\vec{w}$ along the cross-sectional major axis, see Fig. 131, left. The flexural-torsional buckling mode is a combination of a rigid body motion and a rotational displacement around the cross-sectional shear center of the L-shaped profile, see Fig. 131, right.

Referring to previous scientific works on the topic of buckling phenomena of steel L-shaped profiles [29, 30, 31] the two most common failure modes occur at different slenderness ratios. For members with the same cross-section size at a certain length a transition between the torsional-flexural and flexural buckling occurs, this length is often referred as transition length. A transition length indicated on the critical buckling curve of an exemplary L shaped member analyzed in a compression test is depicted in Fig. 132, the graph is based on experimental results of hot-rolled fixed ended angles in compression given in [30]. What is more, a clear dependency of members' cross-sectional dimension and effective length on the resulting failure mode is presented in the study [30]. The slenderer members are more vulnerable to pure-flexural buckling failure mode. Meaning, smaller cross-sectional members have smaller transition lengths.
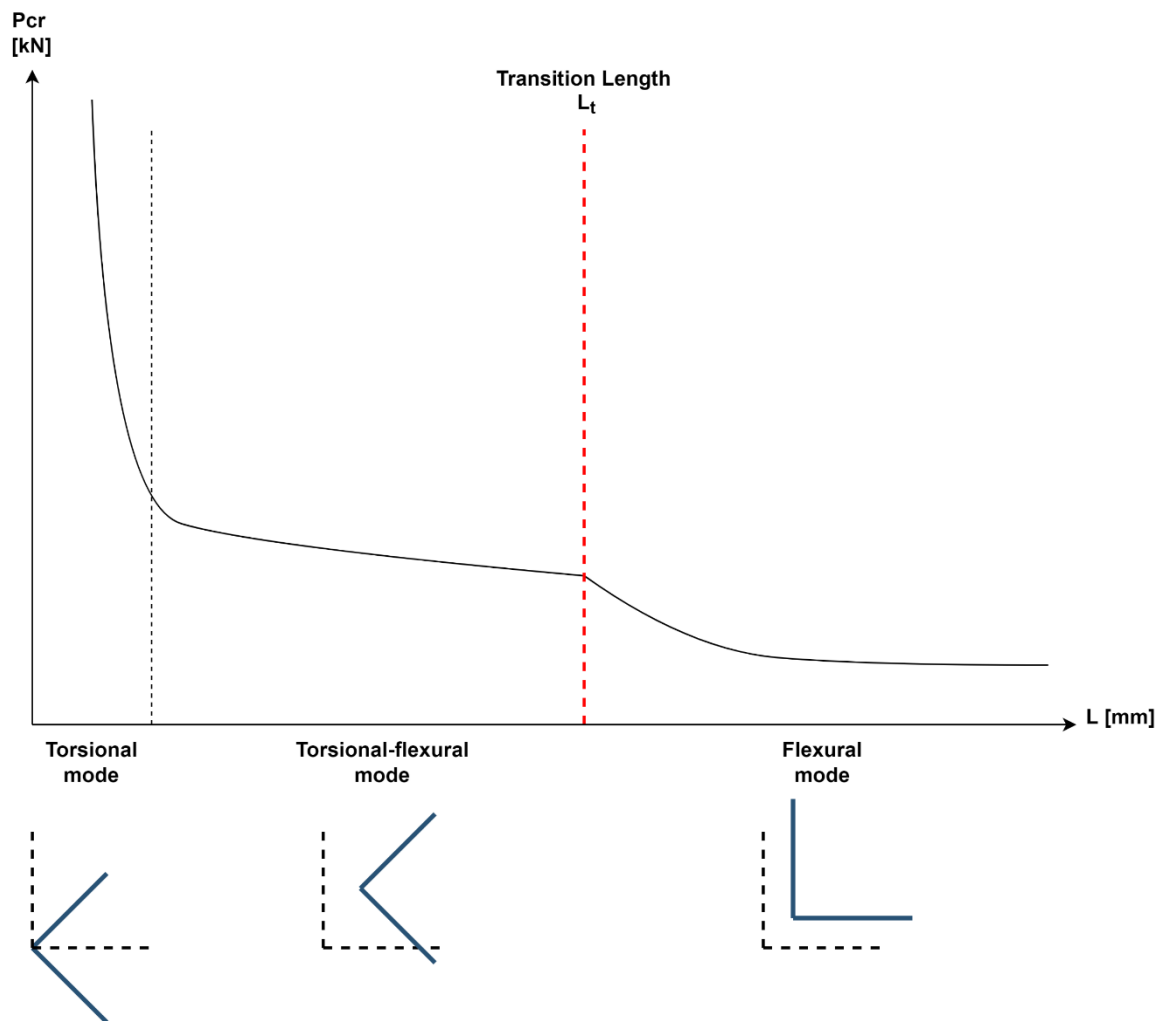
Figure 132 Critical buckling load versus member length curves based on [30, Fig. 2]

Figure 132 depicts the occurrence of three buckling failure modes of an L-shaped member at three different length ranges. Torsional and flexural buckling modes appear at low and high slenderness ratios respectively. The torsional-flexural buckling is an intermediate mode, where the higher the slenderness ratio the more flexural mode is present in the buckling response. The experimental results for L-shaped members ranging from L 60 to L 100 presented in [30] showcase a pure torsional mode appearing for members of length L < 300mm. For the largest analyzed cross-section L 100x6, a slenderness ratio $\lambda = \frac{L_{cr}}{i}$ equals $\lambda = \frac{300}{19,7} = 15,22 \: [-]$. In the lattice tower segment analyzed in this thesis none of the L shaped profiles up to size L 100x6 have a buckling length smaller than 600mm. Additionally, the smallest length of profiles larger than L 100x6 equals to L = 1200mm. Considering the largest profiles L 150x12 minimum radius of gyration i = 29,4mm, the required buckling length to expect a pure torsional mode to occur would equal to: $L_{cr} = \lambda * i = 15,22 * 29,4 = 477mm$ which is almost three times smaller than the value appearing in the analyzed lattice tower segment. Based on that knowledge, it can be stated that the buckling failure modes for all members of the analyzed structure should appear as either pure flexural or torsional-flexural mode. In the analyzed models, imperfections were introduced in two different ways.

4.5.1 Imperfections in the point cloud based model

As mentioned at the beginning of the chapter, imperfections for the model based on the LiDAR point cloud data were included during the geometrical model generation stage using the script developed for the thesis.

Considering the geometrical model consisted of system lines with no cross-sectional orientation included in the model, the imperfections introduced to the model represent only the flexural buckling element of the possible failure modes. This assumption is a simplification limited by the point cloud data and model generation approach proposed in this work.

4.5.2 Imperfections in the idealized model

Initial imperfections introduced to the idealized model are based on the shape of the first eigenmode of the bifurcation analysis. This method is a common structural engineering practice utilized for second order FEA. Depending on members geometrical properties, the initial imperfections introduced to the model may represent a pure flexural or a combined torsional-flexural buckling shape.

By applying the imperfections in such a way, it is possible to investigate the differences between the approach proposed in the thesis for the point cloud based model and a traditional approach used for the idealized model.

4.6 Loads

For all analyzed models a displacement method has been utilized. By applying a displacement controlled loading a divergence at the peak force could be prevented, allowing for more accurate results.

Member analysis

For all analyzed members, a normal compressive displacement has been applied. The displacement was attached at one leg's edge simulating an eccentric load due to the unsymmetric bolted connection in the real structure. Fig. 133 depicts the connection of an in-situ member of the analyzed lattice tower segment.

Figure 133 Unsymmetric bolted connection in the in-situ structure

The static scheme of analyzed cases is depicted in Fig. 134.
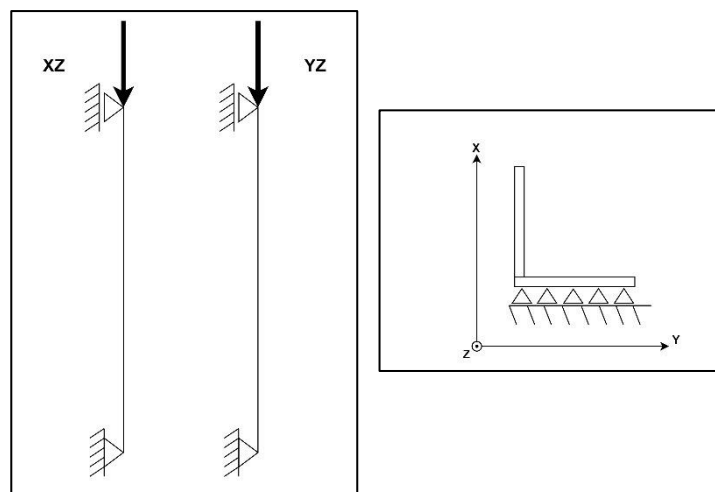
Figure 134 Static scheme for the member analysis

An example of a member analyzed in the Abaqus FEA software is depicted in Fig. 135.
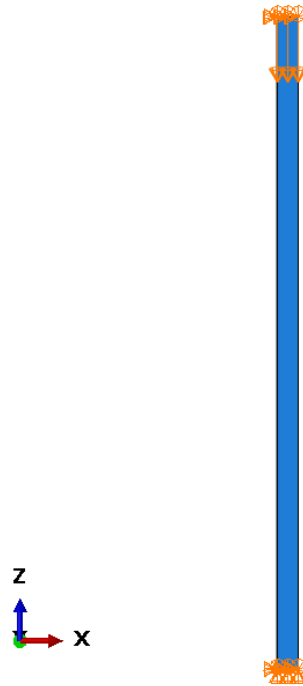
Figure 135 Displacement applied in the member analysis

Global analysis

For the analyzed lattice tower segment during the global analysis, a set of vertical displacements at four main corner legs have been applied. The applied load case is based on an ultimate limit state(ULS) critical load combination extracted from the design documentation provided by the company [25]. The displacements were set as a ratio of the load combination, see Tab. 7.

Load ratio	
A	-1
B	-1
C	0.66
D	0.66

Table 7 Load ratio

The load applied at the corner legs represents an eccentric compressive force, which is a combination of the self-weight of the structure above and a horizontal wind force acting on the tower. The mechanical model of the entire tower is presented in Fig. 136, the tower has been modeled as a cantilever beam.
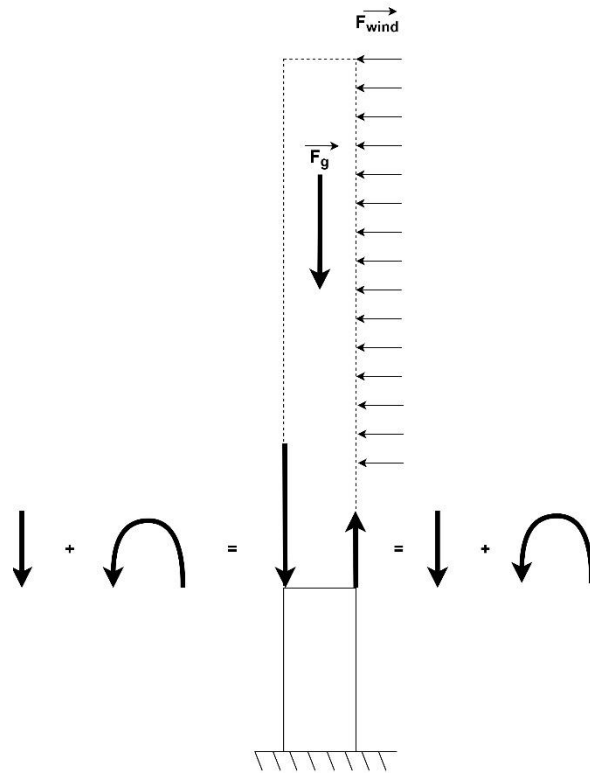
Figure 136 The mechanical model of the analyzed lattice tower

The loads applied at the top of the analyzed tower segment are introduced as a set of four eccentric loads compressing one side of the tower and tensioning the other half.
The analyzed tower segment model in the Abaqus FEA software is depicted in Fig. 137.

Load ratio	
A	-1
B	-1
C	0.66
D	0.66
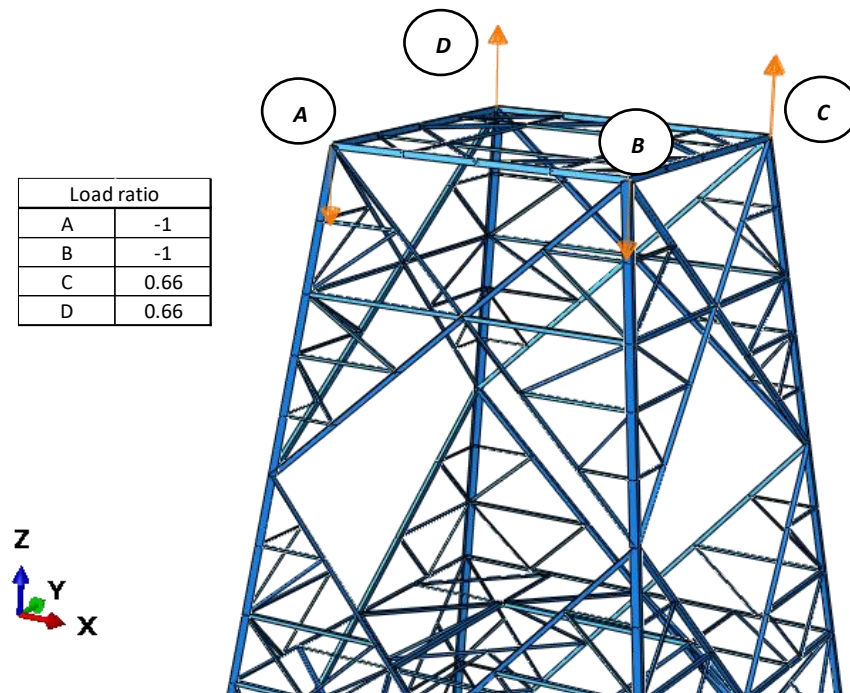
Figure 137 Load applied to the analyzed lattice tower segment

Considering the symmetry of the idealized FEA model, only a single load case needed to be applied during the analysis to depict the most critical load setup.

On the contrary, by introducing the imperfections to the point cloud based FEA model during the geometrical model generation step an asymmetry coming from the real life imperfections of the structure has been added to the entire analyzed tower segment. In order to make sure the set of four vertical displacements has been applied critically, four load cases needed to be applied in the following pattern, see Tab. 8.

Load case 1		Load case 2	
A	-1	A	-1
B	-1	B	0.66
C	0.66	C	0.66
D	0.66	D	-1
Load case 3		Load case 4	
A	0.66	A	0.66
B	0.66	B	-1
C	-1	C	-1
D	-1	D	0.66

Table 8 Load cases applied to the point cloud based FEA model

4.7   Finite Element Analysis type

The analysis carried out for both local member and global cases allowed to investigate the geometrically non-linear response of the lattice tower segment on two different levels. During the analysis, the impact of different initial imperfections inclusion methods for idealized and in-situ based models was studied.

The geometrically non-linear finite element analysis performed in Abaqus FEA software was carried using the Riks method. According to Abaqus manual [28], *Riks procedure is recommended for problems where instability occurs and the succeeding behavior wants to be captured*. Considering the initial imperfections included in the point cloud based models might exceed the buckling deformation, an unstable response is suspected. Additionally, using the Riks method will allow to depict the structures response after the critical buckling load has been reached. Based on given assumptions the decision to choose the Riks method was made.

The applied Riks procedure is defined with the following parameters:

- The non-linear geometry option was switched on, to account for the geometric non-linearity,
- No maximum load or displacement criteria was defined, the analysis would terminate after the defined number of increments was meet,
- To solve the nonlinear equilibrium equations Full Newton Raphson solution method was applied,
- Maximum number of increments was set to 100,
- The analysis was controlled using the Arc-length method,
- The size of the arc length increments was computed automatically by the software based on computational efficiency,
- The initial arc length $\Delta l_{in} = 0.01$
- The minimum arc length $\Delta l_{min} = 10^{-5}$
- The maximum arc length $\Delta l_{min} = 10^{36}$
- The estimated total arc length $l_{period} = 1.0$
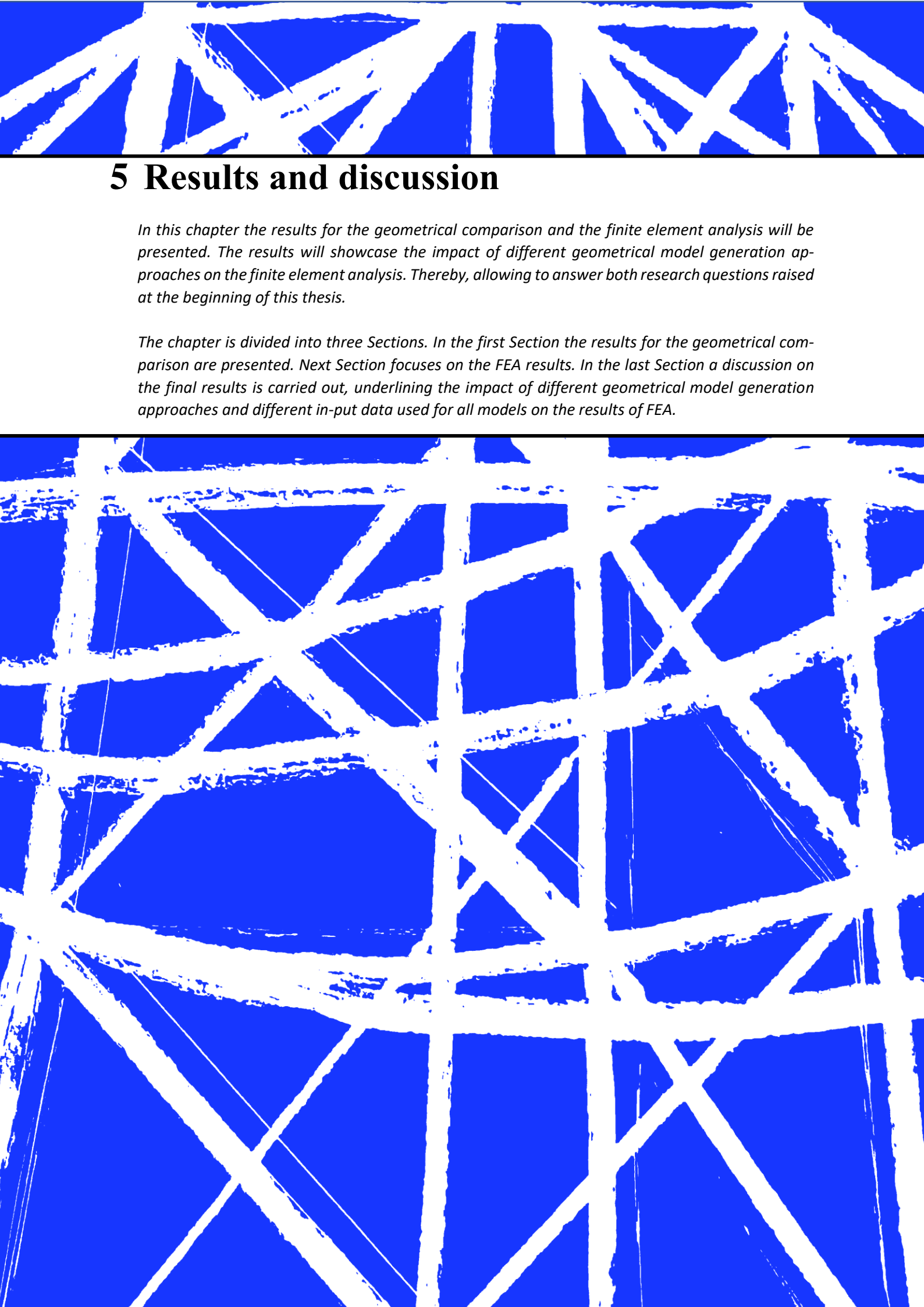
5 Results and discussion

In this chapter the results for the geometrical comparison and the finite element analysis will be presented. The results will showcase the impact of different geometrical model generation approaches on the finite element analysis. Thereby, allowing to answer both research questions raised at the beginning of this thesis.

The chapter is divided into three Sections. In the first Section the results for the geometrical comparison are presented. Next Section focuses on the FEA results. In the last Section a discussion on the final results is carried out, underlining the impact of different geometrical model generation approaches and different in-put data used for all models on the results of FEA.

5.1 Geometrical deviation analysis

The first Section focuses on the results of the geometrical comparison between all the line models generated for the purpose of the FEA. The detailed explanation on the modeling procedure and methodology behind geometrical comparison was presented in chapter 3. Each member is defined by a system line and two end-points, referred as nodes during the geometrical deviation analysis.

The geometrical deviation analysis allows to outline the differences in geometrical models which will help to understand the differences in the finite element analysis results.

The results of the geometrical comparison are divided into a global comparison of the entire analyzed lattice tower segment and a local comparison performed on a member level.

Global deviation analysis

For the global comparison, the absolute nodal deviation between corresponding member nodes of the idealized and both point cloud based line models have been computed. Two comparisons have been performed:

- Terrestrial point cloud based model to idealized model
- Aerial point cloud based model to idealized model

Table below summarizes the results of the global deviation for the two cases:

Node deviations				
[mm]	mean value	std. σ	max	min
Terrestrial vs Idealized model	120	80	607	9
Aerial vs Idealized model	100	33	188	21
Probability associated with Student's t-Test for two independent groups [%]:				3,5E-05

Table 9 Global absolute nodal deviation

On the basis of the probability associated with Student's t-Test (<< 5%) for two independent groups conducted for the global deviation analysis results, it can be stated that the difference of mean values for the final comparison results gathered in Tab. 9 is statistically significant.

The results of the deviation analysis are presented in two graphs, Fig. 138, 139.
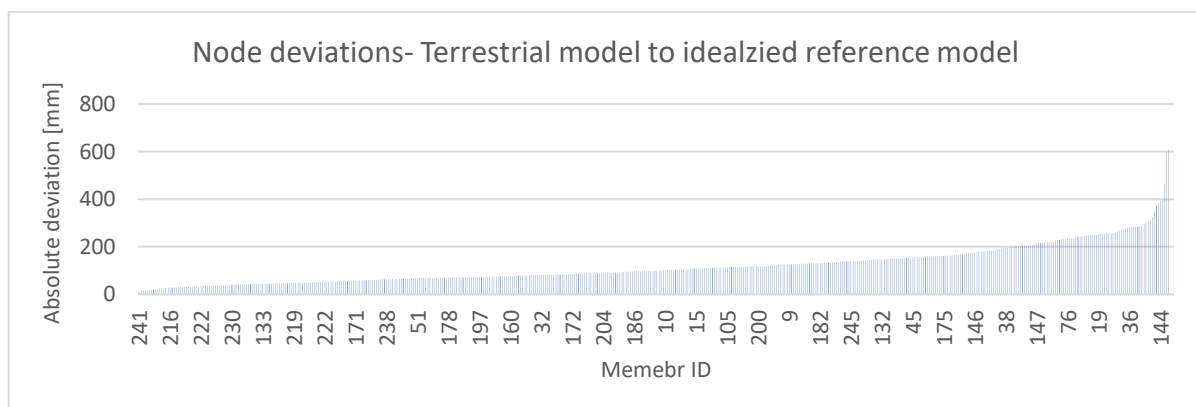
Figure 138 Node deviations- Terrestrial model to idealized reference model

Node deviations- Aerial model to idealzied reference model
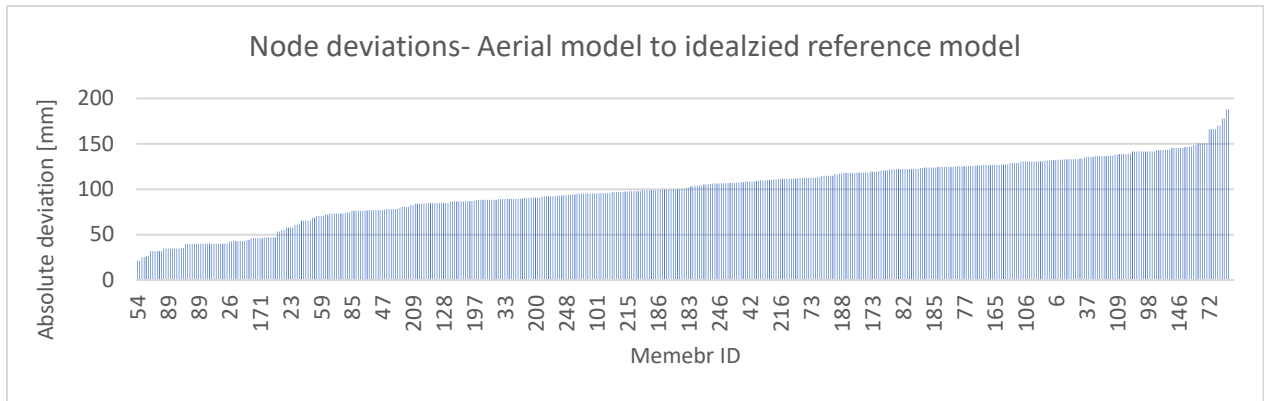
Figure 139 Node deviations- Aerial model to idealized reference model

The graphs depict the absolute nodal deviation of every node for every member in the analyzed lattice tower segment for both cases.

Additionally for every global geometrical comparison graph, a corresponding visual representation is depicted in Fig. 140, 141 accordingly.
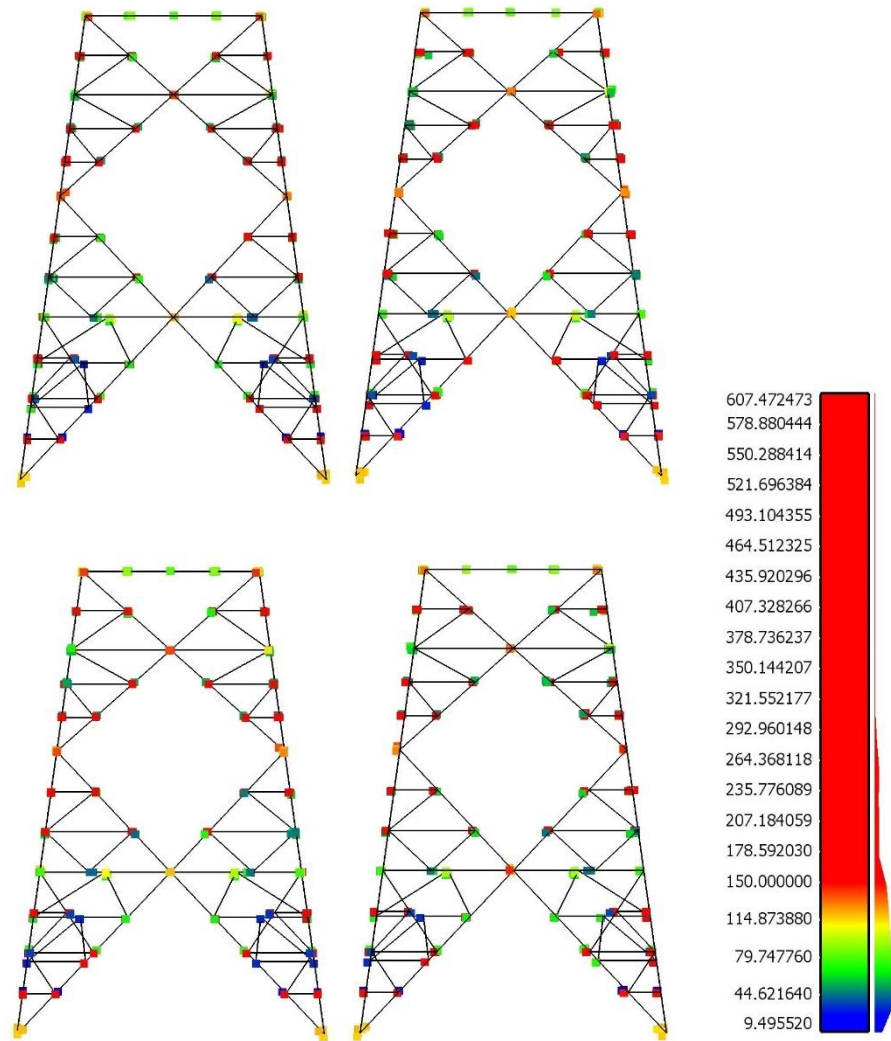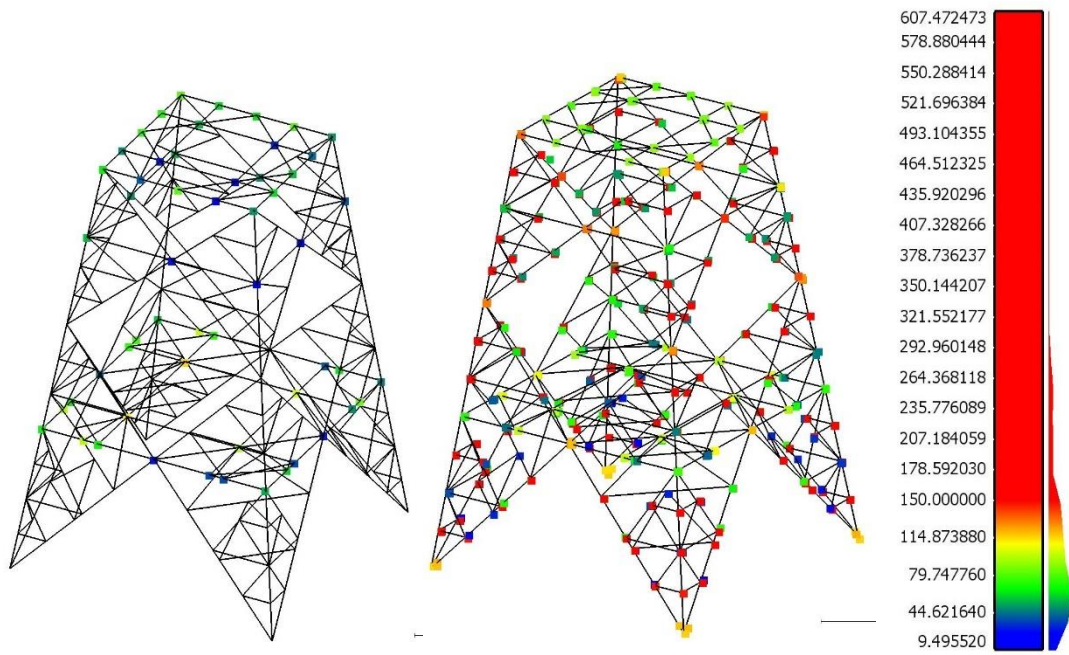
Figure 140 Visual representation of nodal deviation of the terrestrial model compared to the idealized model
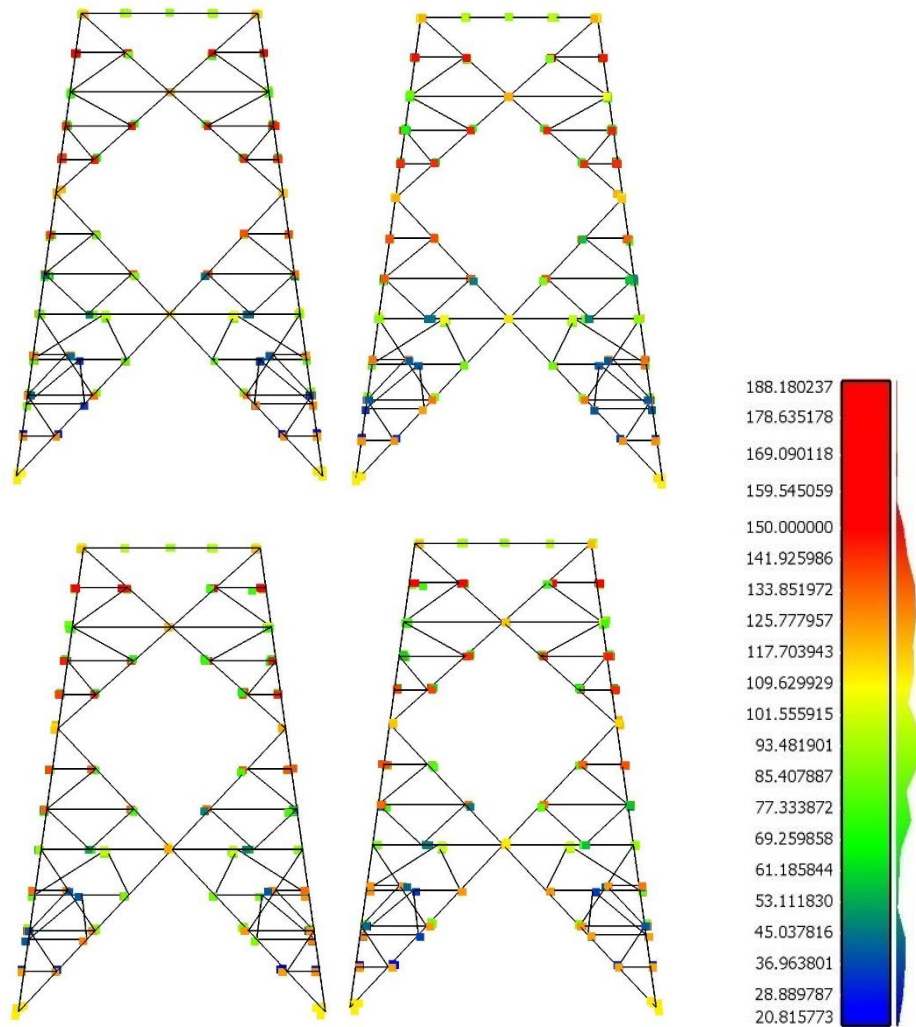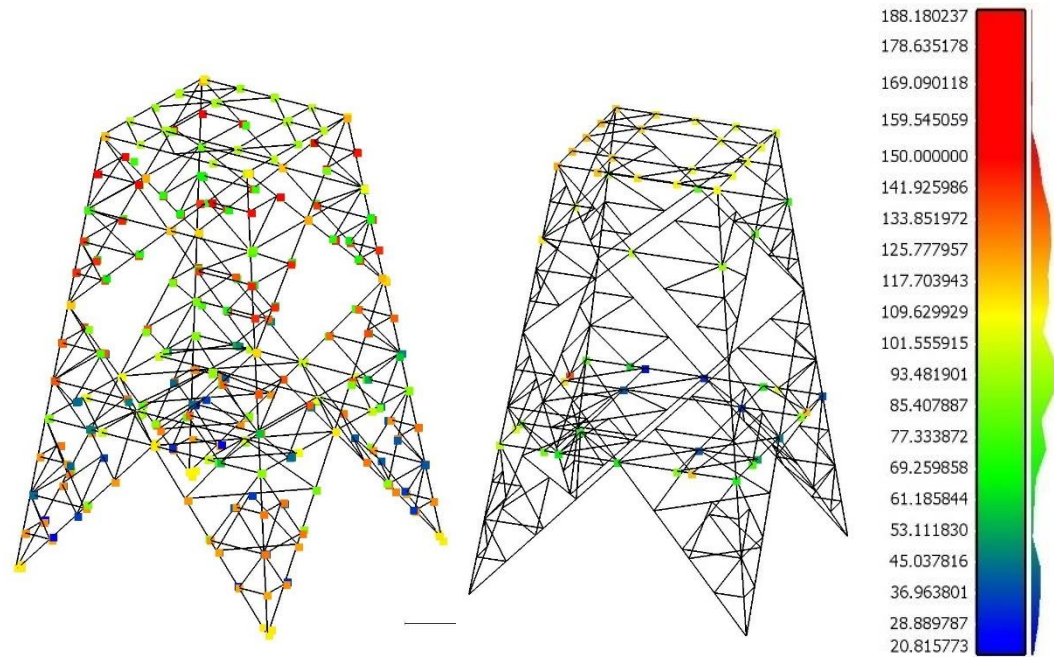
Figure 141 Visual representation of nodal deviation of the aerial model compared to the idealized model

The visual representation showcases the nodal deviations at the discretized reference points. Values for absolute nodal deviations are depicted in scalar fields, presented on the right side of each figure (Fig. 140, 141). The gradient range for the scalar fields has been normalized for both data sets- blue and red colors have been set for 0mm and 150mm values of absolute nodal deviations accordingly.

In the view of the global deviation results, the point cloud based model which geometrically diverges the most from the idealized reference model is the model based on the terrestrial LiDAR point cloud generated with the script proposed in this study. The absolute nodal deviations computed at the reference points are significantly larger for vast majority of the nodes.

The larger nodal deviations of the terrestrial data based model are caused by the level of detail included in this geometrical model. All connections are defined with the inclusion of real life eccentricities which causes the nodes of each member to be displaced to their in-situ position rather the an approximated one, as in the two other cases, a close-up of the phenomena is depicted in Fig. 142.
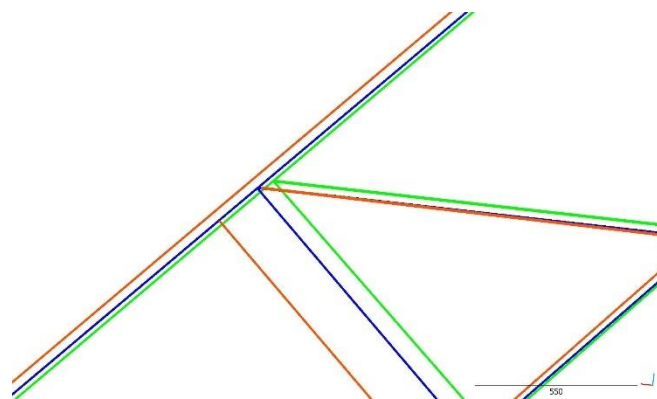
Figure 142 Difference in connection definition between all line models.

Blue(design), green(aerial), orange(terrestrial)

Additionally the position of every members system line is much more precise compared to the aerial point cloud based model for which a manual line fitting was utilized.

The average nodal deviation for both point cloud based models compared to the idealized reference model is in the range of 100 mm. Nonetheless, the standard deviation for the terrestrial based model is much higher compared to the aerial one, being 80mm and 33mm accordingly. The high standard deviation for the terrestrial model indicates large scattering of measurements, resulting from diversity of eccentricities included in the model.

Looking at the visual representation of nodal deviations (Fig. 140, 141), it can be noted that largest differences in nodal deviations between both point cloud based models occur in connection regions where end-plates are located. Considering the fact that the aerial based model uses approximated single node connections, the differences in nodal positioning of members in those connection regions can deviate up to 150mm between the two point cloud based models. An example of a connection region with an end-plate is depicted in Fig. 143.
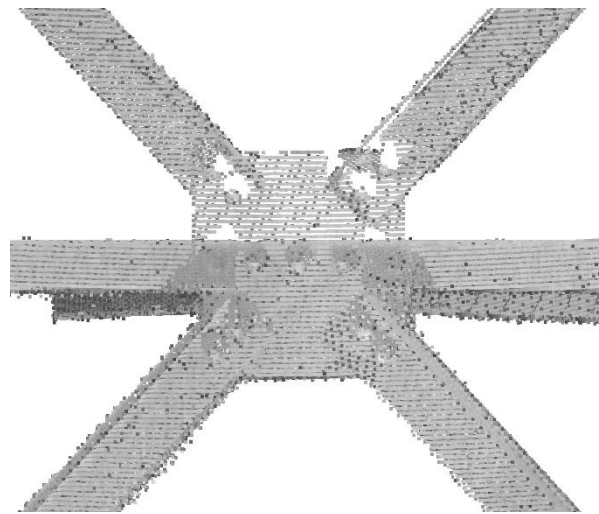
Figure 143 TLS data of an end-plate connection

What is more, the largest nodal deviation for the terrestrial model is four times larger than it's corresponding deviation in the aerial model being as follows 607mm and 137mm.

The member with largest nodal deviation is depicted in Fig. 144.
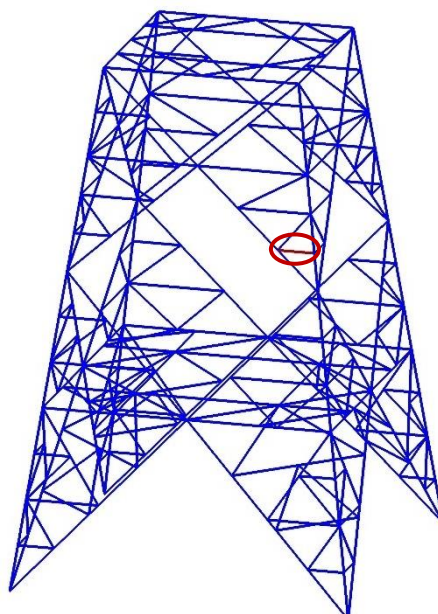
Figure 144 Member with largest nodal deviation(red)

The global deviation allowed to depict the difference between the idealized geometrical model and the imperfect models based on the in-situ tower. Moreover, the impact of the eccentricities included in the terrestrial data based model was exhibited.

Local comparison

After conducting the global deviation analysis, a local analysis was performed allowing to identify members in the point cloud based models with largest discrepancies compared to the idealized model.

The local comparison results are presented in two parts. First, the lengths deviations for all members in both models are presented. Afterwards, the maximum deformations of each member in the terrestrial point cloud based model are summarized.

Length comparison

For the local comparison the length difference between corresponding members of the idealized model and both point cloud based line models have been computed. Two comparisons have been performed:

- Terrestrial point cloud based model to idealized model,
- Aerial point cloud based model to idealized model,

Table below summarizes the results of the length comparison for the two cases:

Relative normalized length difference				
[%]	mean value	std. σ	max	min
Terrestrial vs Idealized model	1,85	1,33	7,55	-13,74
Aerial vs Idealized model	0,80	0,49	3,20	-3,14
Probability associated with Student's t-Test for two independent groups [%]:				0,14

Table 10 Relative normalized length difference

On the basis of the probability associated with Student's t-Test (< 5%) for two independent groups conducted for the length comparison results, it can be stated that the difference of mean values for the final comparison results gathered in Tab. 10 are statistically significant.

The results of the length comparison are presented in two graphs, Fig. 145, 146.
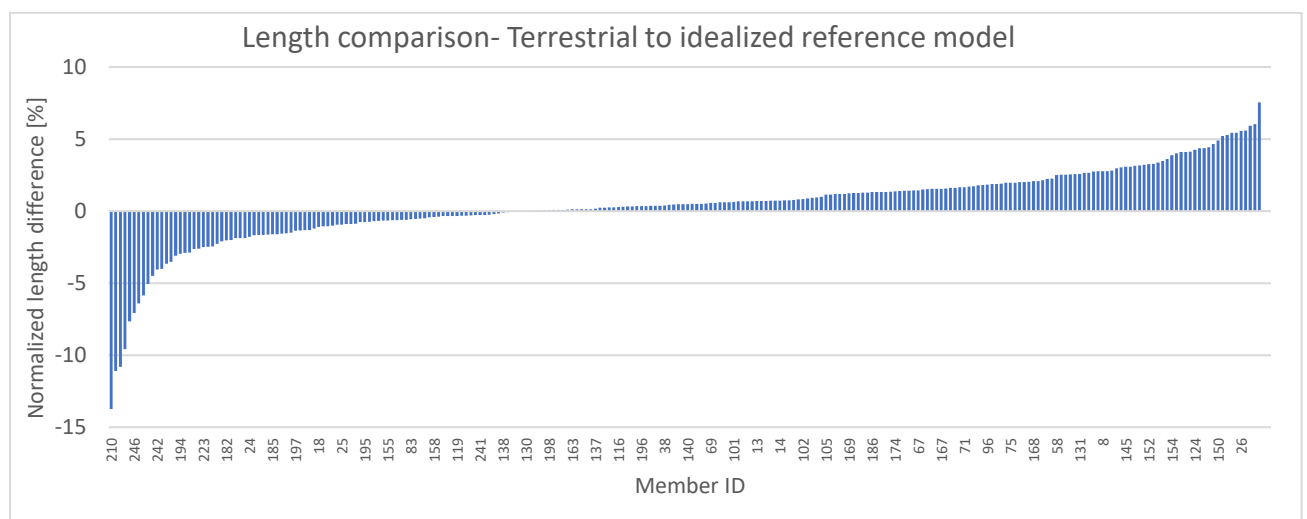
Figure 145 Length comparison- Terrestrial to idealized reference model
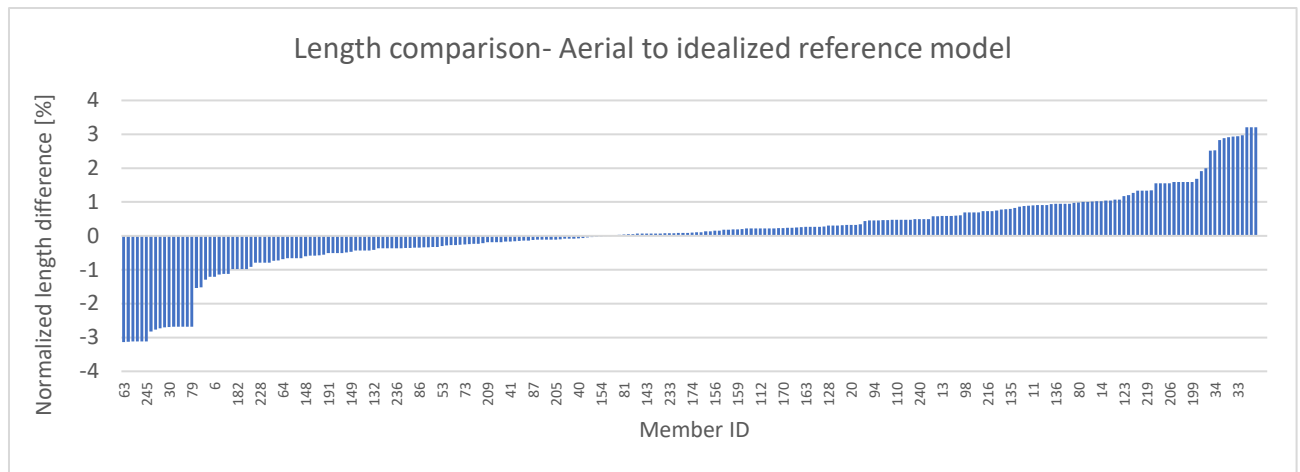
Figure 146 Length comparison- Aerial to idealized reference model

The graphs depict the normalized length difference of every member in the analyzed lattice tower segment for both cases.

Similarly to the global comparison, members in the terrestrial data based model deviate more. The introduction of imperfections to the model leads to an increase in members length. On the other hand, the inclusion of eccentricities in the model shortens the final TLS data based members. The added outcome of both geometrical imperfections is a mean members normalized relative length difference of 1,85% and 0,80% for the TLS and ALS data based models accordingly. The average length difference seems like a minor deviation but for isolated extreme cases the results are more significant. The maximum and minimum percentile length differences for both terrestrial and aerial data based models are consequently 7,55%, -13,74% and -3,14% and 3,20%. For the terrestrial based model the normalized length difference for 9 members exceeds 5%. What is more, for other 9 members in the same model the length is shorter by more than 5%. The extreme cases for which length differences are larger than 5% are depicted in Fig. 147.
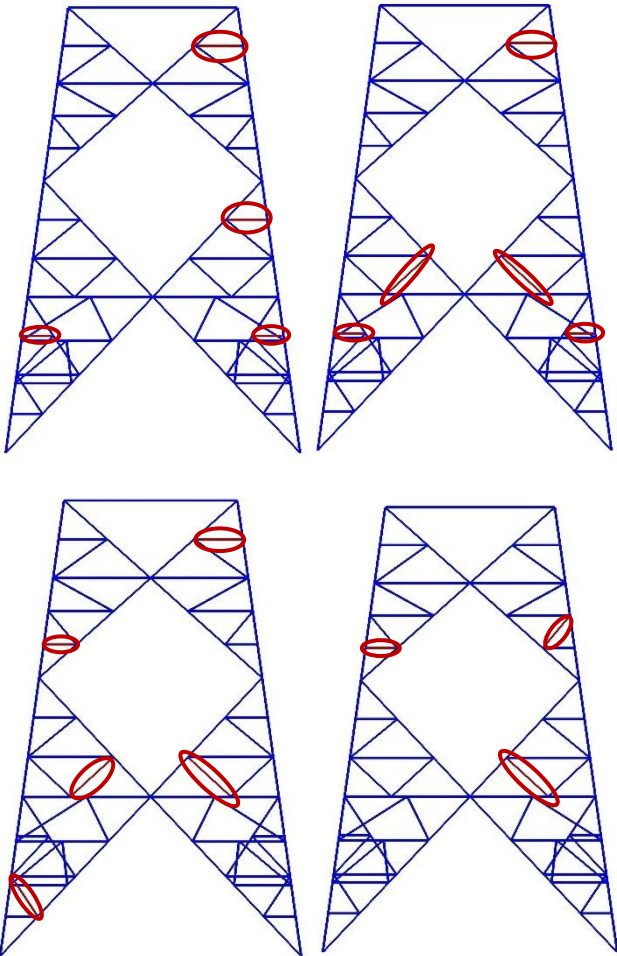
Figure 147 Members with length difference larger than 5%.

Terrestrial to idealized models comparison

Geometrical imperfections of the terrestrial point cloud based model

In the final step of the geometrical comparison, imperfections included in the terrestrial data based geometrical model were computed. The summarized results are displayed in the following graph, Fig. 148:
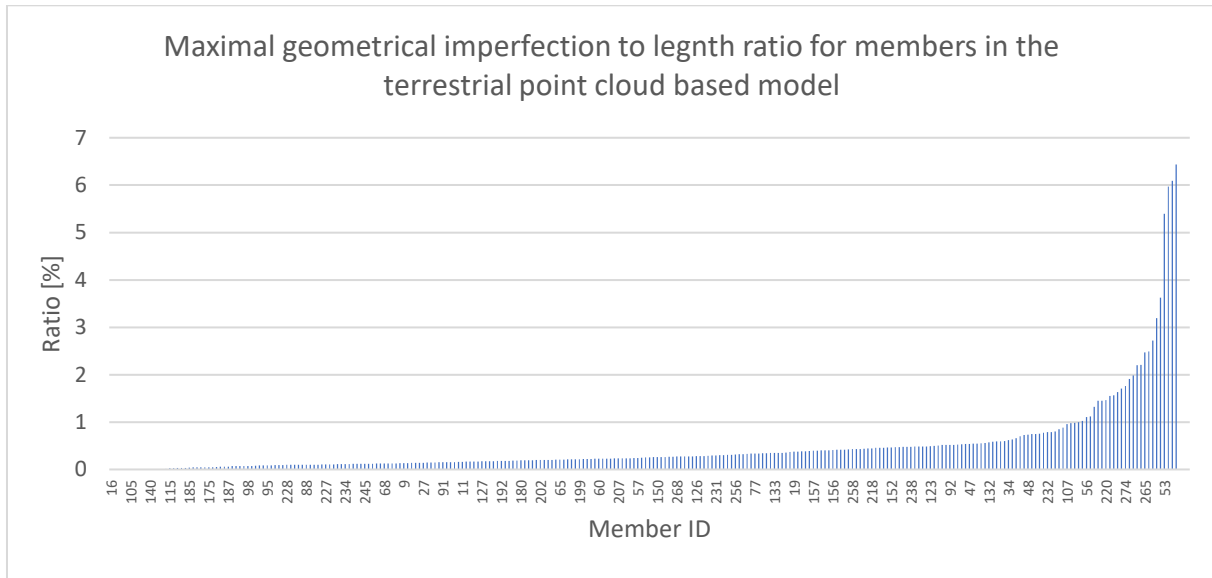
Figure 148 Maximal geometrical imperfection to length ratio-

terrestrial point cloud based model

Final values for members' imperfections in graph (Fig. 148) are presented as the extreme imperfection to length ratio computed as:

$$ratio = \frac{d_{max}}{L_{member}} * 100\%$$

Showcasing the imperfections relatively to the members length normalizes the results allowing to locate members for which the imperfection might have a big impact on the FEA results. The average ratio and corresponding standard deviation for all analyzed members was 0,49% and 0,84% accordingly. The maximum ratio of 6,43% in the given data set occurred for member 248, depicted in Fig. 149.
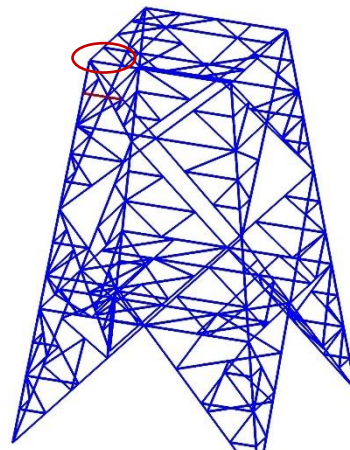
Figure 149 Member(red), with highest im-
perfection ratio

Based on the geometrical comparison, for further analysis purposes 6 members with highest ratios were chosen for the FEA, Fig. 150.
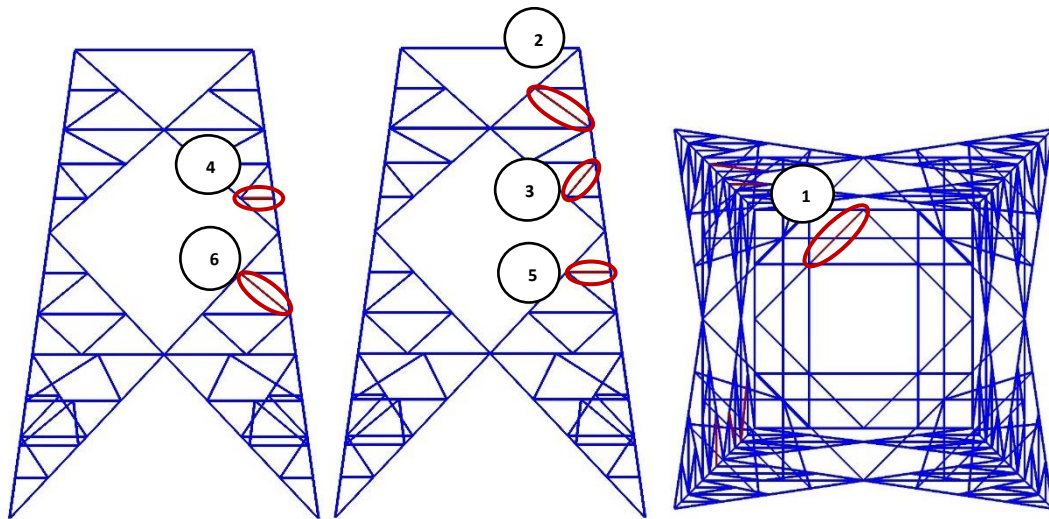
Figure 150 Members(red) with highest geometrical deviations chosen for FEA of isolated members,

in the analyzed lattice tower segment

The results of the geometrical comparison clearly show that the models based on the point cloud data deviate from the idealized model based on design documentation. Deviations in the range of 100mm, as exhibited in the global comparison results (Tab. 9) might not only have an impact on the FEA results but could be an important information during maintenance of the structure in cases where reinforcements or members replacement is required.

What is more, increasing the level of geometrical details in the terrestrial point cloud based model by the inclusion of eccentricities and imperfections and comparing the deformed structure with the idealized model allows to identify members with localized deviations. Later on, the deformed members could be verified, if deflections are lower than the allowable limit by checking them for e.g. under an Eurocode stability limit state(SLS) criteria. In the analyzed case, the lattice tower structure does not require a SLS check [32] therefore this step was not performed.

After understanding the geometrical difference between the idealized and terrestrial point cloud based line models, results for the finite element analysis will be presented.

5.2   Finite element analysis

The results for the finite element analysis carried for both the idealized and LiDAR point cloud based models will be divided into two parts:

- Analysis of members selected during the geometrical deviation analysis
  (see Fig. 150)
- Global analysis of the entire analyzed lattice tower segment

Member analysis

During the member analysis all results for both idealized and LiDAR point cloud based models are com-pared to the buckling forces of given members. Two referential buckling forces were computed. The first one, have been computed analytically using EN 1993 standard [27] and 'Theory of Elastic Stability' [33]. The other one, obtained from FEA results by multiplying the critical factor extracted from the Linear Buckling Analysis(LBA) and the load applied during the LBA. The detailed description for both buckling force computation methods is provided in Annex A and Annex B accordingly.

The results of the member FEA for all analyzed members are depicted in the force-displacement graphs below, Fig. 151.
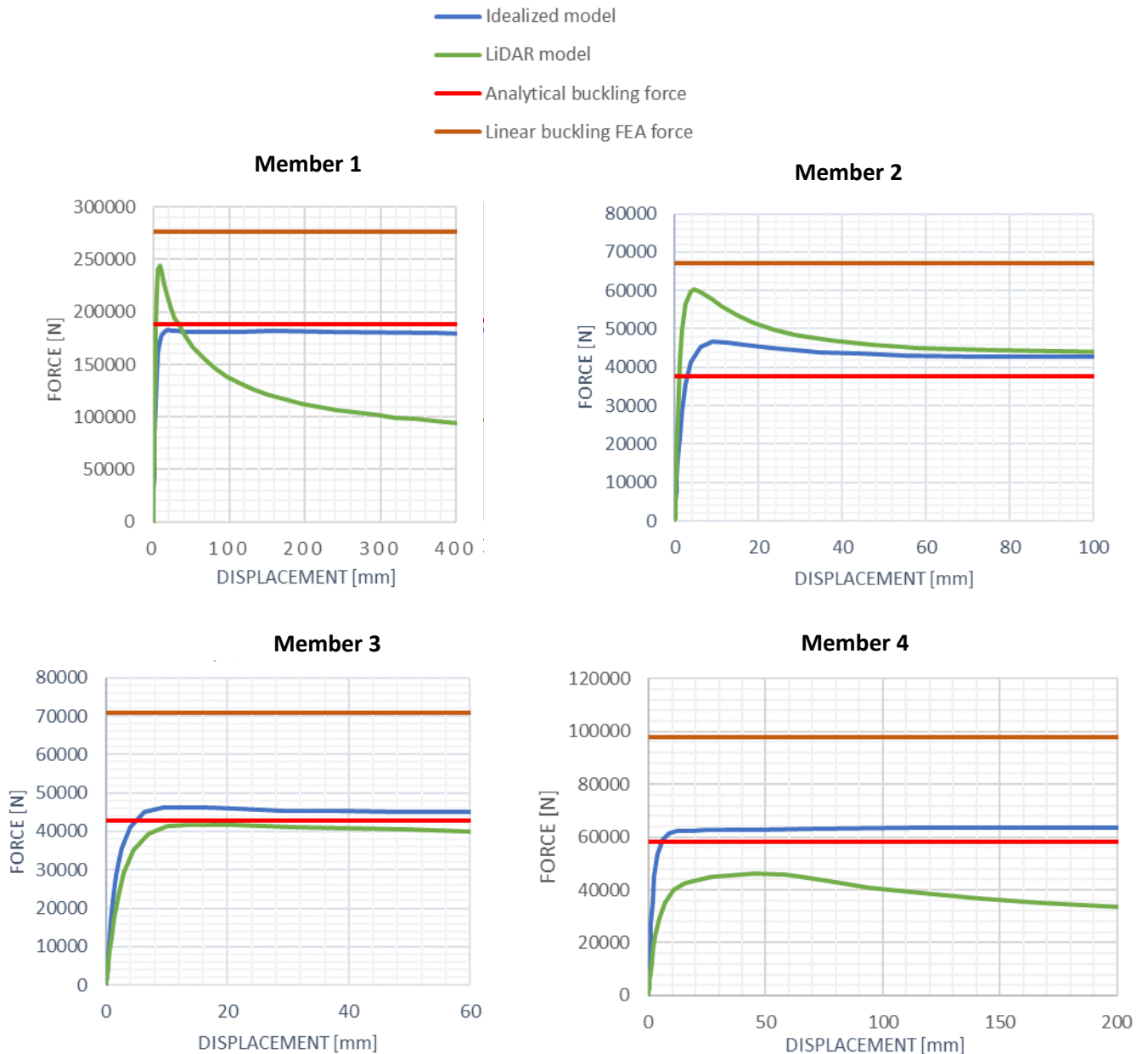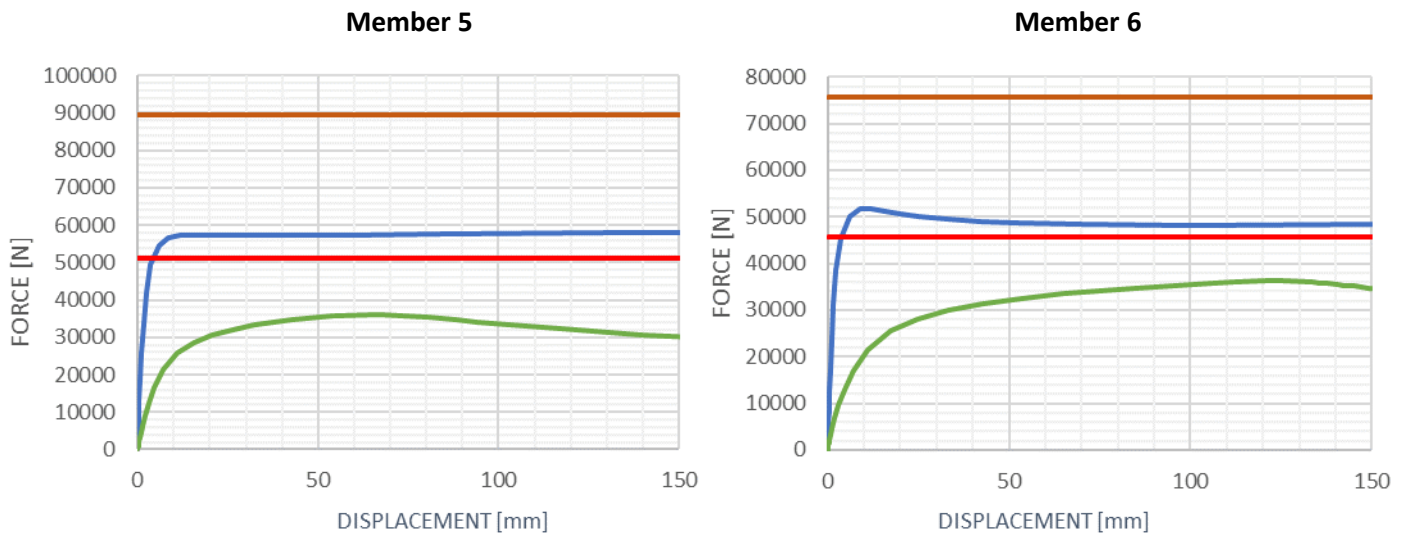
Member 5

Member 6

Figure 151 Force-displacement graphs for local analysis

Additionally the results for all members have been collected in Tab. 11:

	Idealzied model	Analytical buckling force	Relative difference	Linear buckling FEA force	Relative difference	LiDAR model	Relative difference
	[kN]	[kN]	[%]	[kN]	[%]	[kN]	[%]
Member 1	182,66	196,71	3,29	276,87	51,57	244,67	33,95
Member 2	46,60	38,45	-19,08	67,16	44,10	60,20	29,18
Member 3	46,28	43,66	-7,47	70,92	53,23	41,80	-9,69
Member 4	63,63	59,18	-8,67	98,00	54,02	46,22	-27,36
Member 5	57,97	51,56	-11,78	89,64	54,65	36,23	-37,50
Member 6	51,73	46,77	-11,69	75,74	46,42	36,38	-29,67
Relative difference- the relative difference between given buckling/ ultimate force and the force value of the idealized reference model							

Table 11 Member analysis results

Member FEA discussion:

Comparing the resulting forces for isolated members allows to understand the impact of different computational approaches and modelling assumptions on the final results of the analysis. Assuming the idealized models' results (Fig. 151, blue color) as the reference, the following reflections can be drawn:

For all analyzed cases, the buckling force of the idealized model gives the closest result to the analytical approach (detailed derivation given in Annex A), for which the minimal critical load between flexural, torsional and flexural-torsional buckling modes have been presented in graphs (Fig. 151, red color). Nonetheless, the results deviate. The buckling force for the idealized model is larger for all members excluding member 1, for which a relative difference of 3,29% is depicted (Tab. 11). The comparison between idealized model FEA results and analytical buckling forces indicates a conservative solution of the analytical response. In the analytical solution, the buckling length has a big impact on the resulting buckling force. The larger buckling length implies a smaller buckling force. The conservative result of the analytical solution might be caused by the inability to define boundary conditions accurately using the EN 1993-1-1 guidelines. According to [33] for simply supported pinned conditions, where no

torsional and warping restraint is present, the buckling length for torsional-flexural mode can be assumed equal to the system length. For all analyzed members, a single leg pinned conditions along the angle edge have been assumed. Approximating this more complex boundary condition to a simply supported case might lead to non-precise results caused by inaccurate buckling length definition.

Looking at the linear buckling analysis(LBA) buckling forces (Fig. 151, brown color), we can notice an overestimation of results for the linear analysis compared to the non-linear approach applied to the idealized models by approximately 50% for all analyzed cases. Although, for both linear and non-linear cases the deformation modes are alike, depicting a torsional-flexural buckling phenomena. An overestimation of results of the linear response is to be expected. The Euler method related to the LBA is very sensitive to boundary conditions definition, for complex connections like the one in the analyzed lattice tower, the method might lead to inaccurate results.

Finally, a juxtaposition between the idealized models' critical forces and the ultimate forces of the LiDAR point cloud based models is carried. It is worth to remind that for the point cloud based model the initial imperfection follows a pure flexural deformation, whereas for the idealized model the deformation shape is a combination of torsional and flexural mode. Looking at the analytical solution and the linear buckling analysis of the analyzed members, the pure flexural buckling mode is less critical than the torsional-flexural one. For the analytical solution in all analyzed cases, the critical forces for torsional-flexural buckling were lower than the pure flexural ones. What is more, the eigenmodes with the lowest eigenvalues for the LBA depicted a combination of flexural and torsional deformation for all analyzed cases, confirming the critical buckling mode to originate from a torsional-flexural deformation. Looking at analyzed members in the LiDAR point cloud based model two trends are present. For members 1 and 2, an expected buckling response is depicted with a linear elastic step until the critical load is reached and a non-linear behavior afterwards. For both members, the ultimate force for the point cloud based model is greater than the critical force of the idealized reference model (Fig. 151, Tab. 11). For members 3 to 6, the ultimate force is lower than the corresponding critical force of the idealized model. Greater ultimate force values for members 1 and 2 of the point cloud based model might be caused by the introduction of a less critical initial imperfection shape with the reference to the buckling phenomena. Additionally, the ratio of the initial imperfection to members length for the first two members is significantly smaller compared with the ratios for the rest of the members in the point cloud based model. Meaning its effect on the reached ultimate force is less impactful. For members 4 to 6 the initial imperfection exceeds the linear elastic deformation range leading to large eccentric loading of the member and a non-linear response from the beginning of the applied load (Fig. 151, green color). The large initial imperfections introduced for members 3 to 6 in the point cloud based model have a great impact on the ultimate members resistance leading to a 30% reduction of the maximum applicable load compared to the idealized model. The response of the third member to the applied load for the idealized and point cloud based model is comparable, although different initial imperfections were implemented.

Global analysis
During the global analysis the ultimate members resistance under the eccentric horizontal compressive force applied to the main corner legs of the analyzed lattice tower segment (defined in Section 4.5) was investigated. Five analysis were carried out, one for the idealized model and four for the LiDAR point cloud based model to cover all the possible critical load cases considering point cloud based model's geometrical asymmetry caused by the introduction of real life imperfections.

In all analyzed cases the collapse behavior was equate. The members which reached their structural resistance first were the main diagonal members located on the upper part of the analyzed tower

segment. All results for the analyzed cases are presented below. Fig. 152 to 154 depict the deformed state of the models under the applied loading which caused the main diagonals to fail.

Deformed state at the ultimate load step:
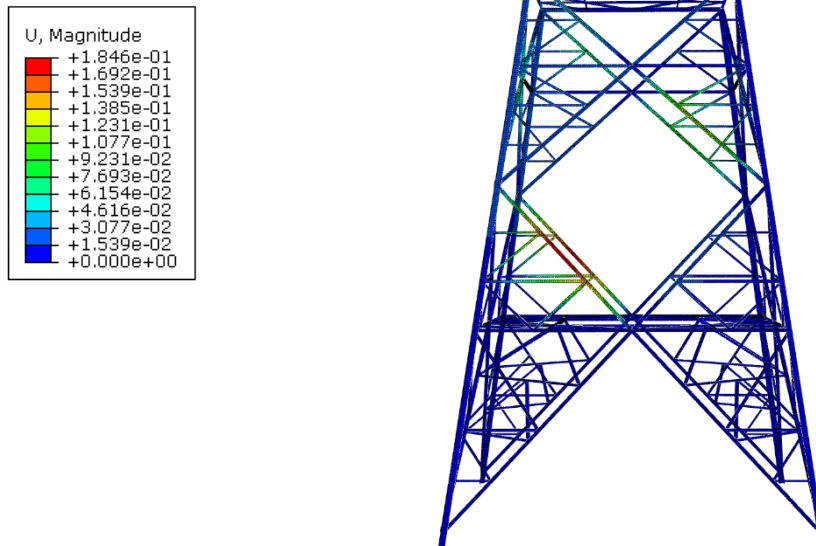
Figure 152 Idealized reference model. Deformed state at the ultimate load step
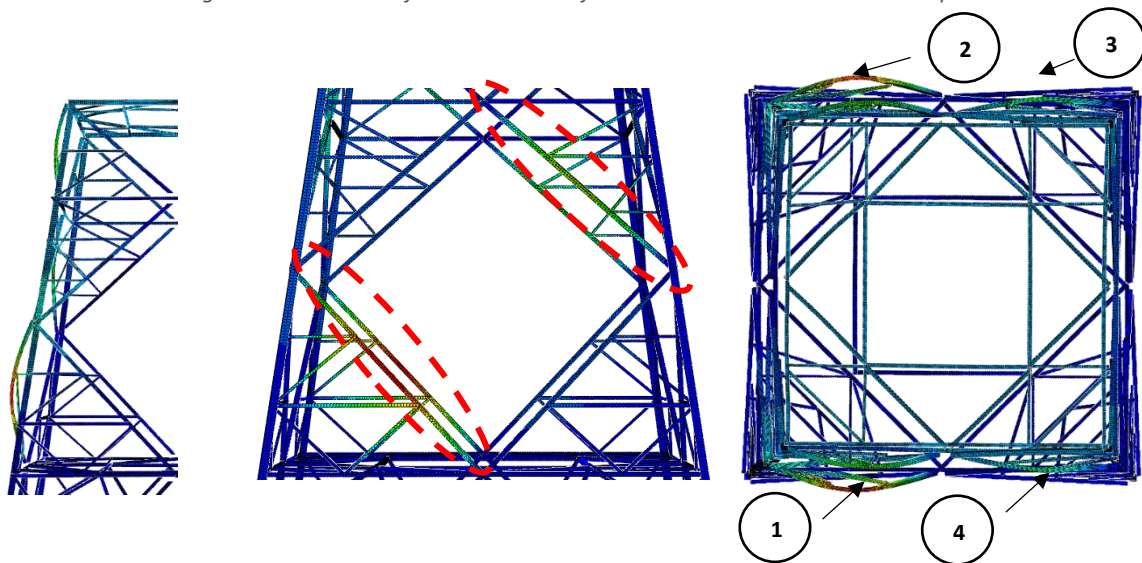
Figure 153 Failing diagonal members after reaching the ultimate load step. Member ID(right)
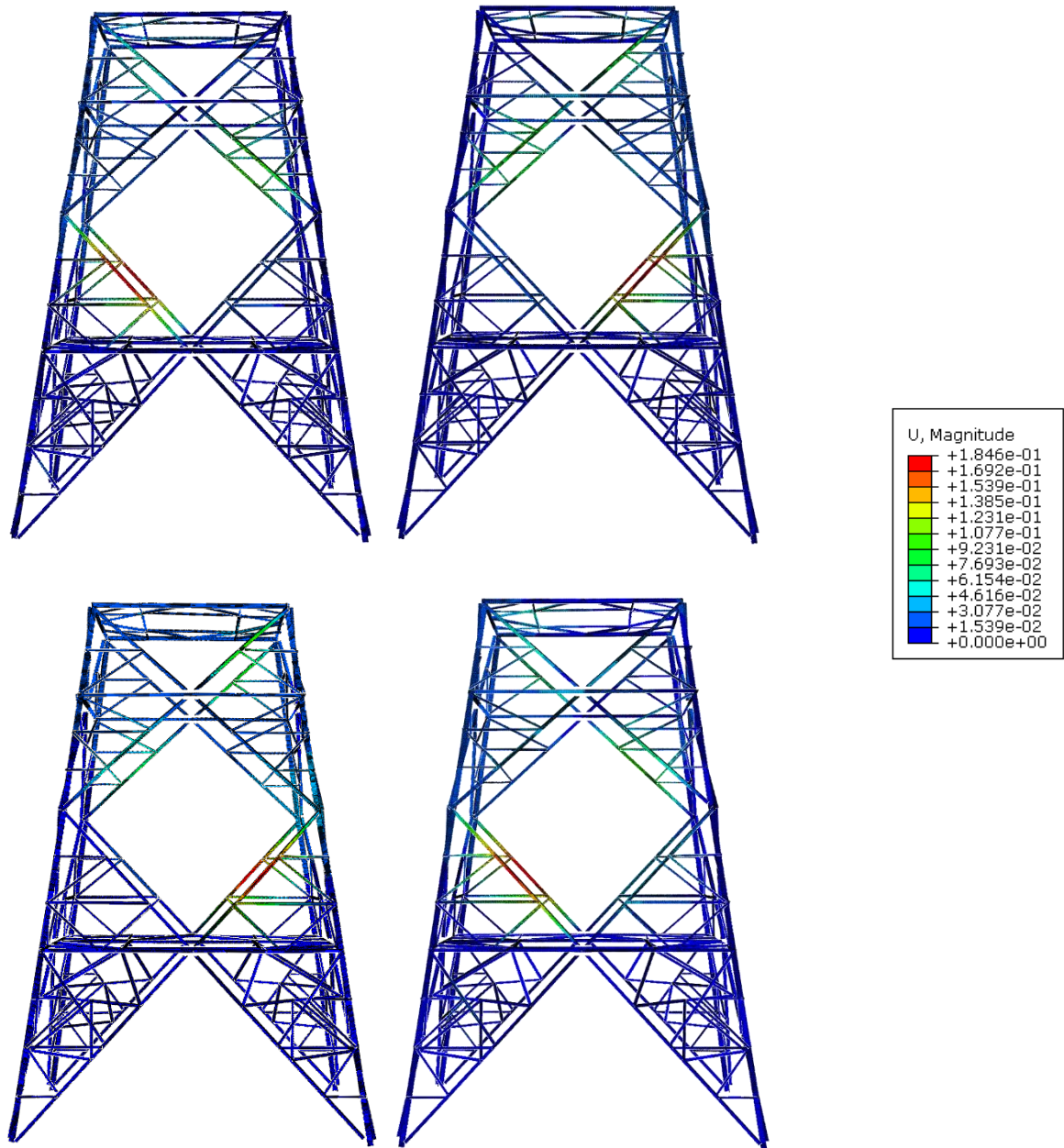
Figure 154 LiDAR model, Deformed state at the ultimate load step.

Load cases: 1(top-left), 2(top-right), 3(bottom-left), 4(bottom-right)

To compare the results of the global analysis for each analyzed case the applied loads at which any of the diagonal members outlined in Fig. 153 reached their structural resistance were collected in a Tab. 13. For the record, the eccentric compressive vertical load was a set of two pairs of loads, compressive and tension normal forces applied with the following ratio to the main corner legs (negative sign indicates compression):

Load ratio	
A	-1
B	-1
C	0.66
D	0.66

Table 12 Applied load ratio

The ultimate applied loadings with corresponding load proportionality factors(LPF) for every global analysis are presented in Tab. 13.

FEA	LPF	Applied load [kN]	
		Compression	Tension
Reference	14,74	-1665,28	1099,08
LC1	13,67	-1848,47	1219,99
LC2	13,34	-1776,42	1172,43
LC3	24,88	-2533,15	1671,88
LC4	14,24	-1681,06	1109,50

Table 13 Resulting reaction forces for all analyzed cases

What is more, for every analyzed case the corresponding maximum von misses stress in every diagonal member outlined in Fig. 153 was collected in Tab. 14. The following table presents the maximum stresses captured at the critical load step for all four main diagonal members in all five performed analysis.

Resulting maximum stress and displacement for failing diagonal members at the ultimate load step									
FEA	Reference		LC1		LC2		LC3		LC4	
LPF	14,74		13,67		13,34		24,88		14,24	
ID\result	σ [MPa]	U [mm]	σ [MPa]	U [mm]	σ [MPa]	U [mm]	σ [MPa]	U [mm]	σ [MPa]	U [mm]
Member 1	235,00	103,38	235,00	110,24	235,00	98,39	134,71	298,63	235,00	102,42
Member 2	220,87	97,98	94,10	58,91	230,54	94,69	123,67	291,90	223,95	98,05
Member 3	136,42	60,56	154,34	57,38	128,65	56,22	235,00	155,75	159,53	58,49
Member 4	214,08	75,19	140,37	99,65	89,09	52,23	232,27	115,29	156,57	35,45

Table 14 Resulting maximum stress and absolute displacement for critical diagonal members at the ultimate load step

Global FEA discussion:

When member FEA results allowed to understand the impact of boundary conditions, and initial imperfections on the analysis of isolated L shaped profiles. The global analysis results showcase the difference of the global response of the analyzed lattice tower segment between the idealized and point cloud based models. As stated in chapter 4, for both models identical analysis assumptions were defined. This way, the effect of different modelling approaches on the FEA results could be studied. The point cloud based model geometrically diverges from the idealized reference one in terms of members length, eccentricity introduced to the connections and initial imperfections included in the geometrical line model.

Looking at the deformed states of the structure at the ultimate load step (Fig. 152, 154) analogical failing mechanisms are depicted. For both models one of the main diagonals of the mid-section reaches its yielding strength. Although the applied load is axially symmetrical, the load is not distributed evenly across symmetrically corresponding members (Tab. 14). This phenomenon is caused by the introduction of asymmetry to the model geometry. As for the point cloud based model, the source of asymmetry is clear and comes from the imperfect state of the in-situ structure. In the idealized model, the geometrical line model is bisymmetrical, therefore the only possible source of asymmetry originates from the initial imperfections introduced during the FEA. Similarly to the member analysis, initial imperfections introduced to the idealized model are based on the first eigenmode of the linear buckling analysis and correspond to a torsional-flexural mode. Under a visual inspection, the global results look almost identical (Fig. 152, 154) but upon a closer investigation the differences are quite significant.

Comparing results of the analyzed lattice tower segment for both models, no good match can be found between any of the assumed load cases of the in-situ based model and the one based on design documentation. Although the results for the failing member in load cases 1,2 and 4 resemble the reference result (Tab. 14, member 1), the remaining members results do not. The load applied at the ultimate load step for load cases 1,2 and 4 differ by 11%, 7% and 1% respectively which indicates a comparable ultimate resistance of the analyzed lattice tower segment was reached. Results for load case 3 significantly diverge from the rest, the applied load is 52% larger than the reference result for the idealized model. What is more, contrary to the other load cases the diagonal member which failed first was the upper diagonal member (member 3) and not the lower one (member 1). The large scatter between results for the different load cases for the point cloud based model highlights the impact of introduced imperfections on final results of the analysis. Even tough, for load cases 1,2 and 4 the applied load at which the ultimate resistance of the analyzed tower is met is comparable, the resulting stresses for the chosen members depict the difference in redistribution of forces across the structure caused by varying imperfection setup. Every analyzed load case presents an unique outcome. For Load case 1, the majority of the applied load is concentrated at the critical member (member 1), leading to a uneven force redistribution across corresponding members. Load cases 2 and 4 depict a more balanced force allocation, where both lower diagonal members are equally stressed. A symmetrical force redistribution is also present for load case 3, for which in both pairs of upper and lower main diagonals stresses are distributed evenly. Although for this load case, the failing member and applied ultimate loading are different.
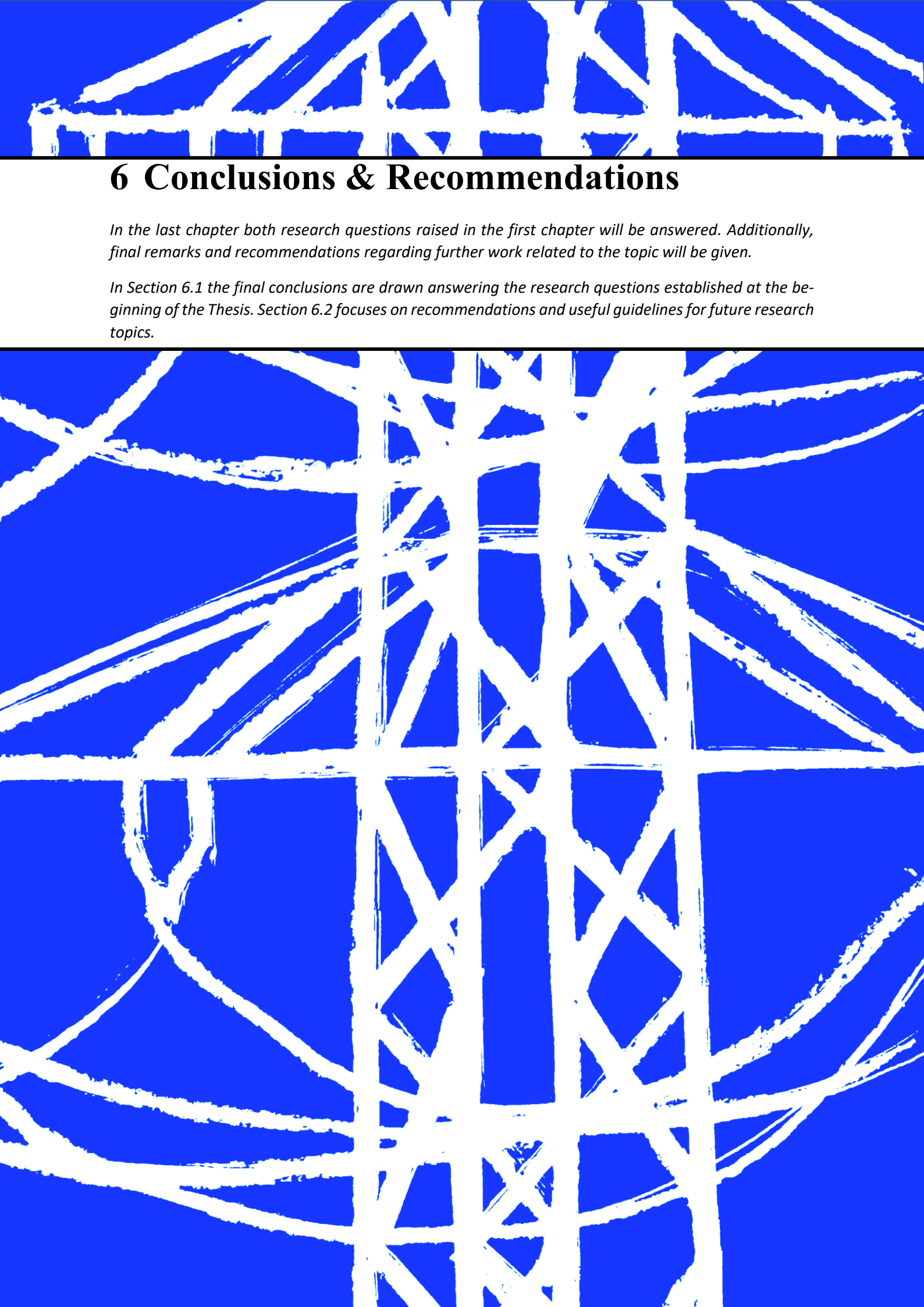
6 Conclusions & Recommendations

In the last chapter both research questions raised in the first chapter will be answered. Additionally, final remarks and recommendations regarding further work related to the topic will be given.

In Section 6.1 the final conclusions are drawn answering the research questions established at the beginning of the Thesis. Section 6.2 focuses on recommendations and useful guidelines for future research topics.

6.1 Conclusions

The main goal of this Thesis was to investigate if point cloud data gathered with currently available LiDAR scanners is a good source of geometric information for structural engineering research carried for steel lattice towers. By conducting the study presented in the work, answers to the research questions raised in the first chapter were found.

6.1.1   Answering the research questions

In order to investigate LiDAR point cloud data's applicability for structural engineering purposes, the following research questions were brought:

- *Does LiDAR point cloud data acquired by an aerial/terrestrial scanner provide sufficient geometric information to create a 3D geometric model with level of detail adequate for FEM application?*

- *How does discrepancy of 3D geometric model based on point cloud data compared to an idealized 3D geometric model based on technical drawings impact FEA results?*

Based on the literature study and performed analysis, final conclusions addressing both research questions are given:

Geometric model generation

- The aerial point cloud allowed to obtain sufficient information regarding the global geometry of the structure but accurate registration of member deformation or modelling of connections is not possible. The noise level in the aerial point cloud data being the limiting factor will not allow to achieve a higher level of detail. Thus, the generated model is believed to be a state-of-the-art example obtainable for the aerial point cloud dataset.

- The terrestrial point cloud enabled for a higher level of detail inclusion due to its overall higher point cloud quality. For the geometric model based on terrestrial data the member detail level was reached, allowing to include the flexural buckling deformation and real joint to joint length of each member. What is more, the eccentricity of the connection was also captured. The limitation of the terrestrial point cloud came from registration issues preventing from acquiring precise cross-sectional measurements.

- Regarding connections modeling, the quality of the terrestrial point cloud data would suffice the extraction of dimensions needed for detailed reconstruction of the end plates and bolts location. Nonetheless, a detailed connection analysis was not part of the study. The main focus was put on investigating the difference in FEA results between an idealized model based on design documentation and a point cloud based model representing the in-situ state of the structure. Since no information regarding connection details were included in the provided design documentation, the FEA model was limited to member level with connections discretized as single nodes.

- What is more, imperfections recognized only in the cross-sectional perspective could be introduced into the analyzed model which includes the torsional part of the flexural-torsional deformation. A commonly occurring buckling mode for L-shaped profiles widely used for steel lattice towers.

FEA results

- Considering deformations, the response of the point cloud based model to the applied loading was equivalent to the idealized model. The critical buckling modes in all analyzed cases were equate. Although the initial imperfections in both models differed, the deformation shape at the ultimate load step for both models was alike. For the member analysis, all isolated members experienced a torsional-flexural deformation. In the global analysis the collapse mechanism was identical for all loading cases. What is more, the magnitude of applied loading during the global analysis stayed within a reasonable deviation range of 3% to 10% for cases were corresponding members reached the structural resistance.

- Regarding the differences in results between the two FEA models, the impact of different initial imperfection inclusion methods is noticeable. For the member analysis the ultimate load for idealized models stayed within the boundaries of conservative analytical and overestimated LBA results, depicting a clear post-buckling behavior in all analyzed cases. Results for idealized members scattered between 19% above than the analytical and 54% below the LBA critical forces. Whereas, the force-displacement graphs vary for each analyzed member in the point cloud based model. Depending on the magnitude of applied initial imperfection, the response is either more or less favorable. The TLS point cloud based models stayed within the boundaries of 48% above the analytical and 62% below LBA response. An exception were three isolated members for which the initial imperfections were so large that no linear force-displacement response was present at the first loading stages, resulting in the reached ultimate forces lower by approximately 30% compared to the corresponding idealized members response.

- For the global analysis the asymmetry introduced to the point cloud based model by the imperfect geometry of the in-situ structure effected the redistribution of forces across the analyzed tower segment. Depending on the load case setup, members corresponding to the same position in a given orientation would exhibit a different stress level resulting in deviations between the load cases reaching up to 60% difference in resulting stresses.

- Combining both of the phenomena of the extensive initial imperfection introduction (depicted in the member analysis) and force redistribution caused by in-situ based imperfections inclusion (witnessed in the global analysis) could lead to an dangerous situation. Let us assume scenario with an identical load case as in the global analysis. The main diagonal members in the middle section are critically loaded. On top of that, the initial imperfection of those members is so large that the ultimate load is lower than the critical buckling load applied to an idealized member. A situation like that would lead to a decreased ultimate resistance of analyzed tower segment compared to a result based on idealized model. Therefore, if in practice a traditional approach for the structural stability check would be adopted the analysis results could be potentially underestimated. This worst case scenario example highlights the main advantage of the proposed modelling approach and summarizes the differences between the two methods, thereby concluding the answer to the second research question.

6.2 Recommendations

This Section is dedicated for recommendations and guidelines useful for future research in the topic of generating geometrical models of steel lattice structures using point cloud data, specifically for FEA applications.

General recommendations:

Recommendations for geometrical model generating method improvements:

- In order to validate the accuracy of the geometrical model generated using the proposed ap-proach, in-situ measurements using traditional geodetic methods of predefined reference points on the analyzed structure would be advised,

- As a general rule, terrestrial LiDAR scanner is a more suitable hardware for data acquisition of steel lattice towers compared to an aerial one. The main advantages are its higher output point density and lower noise level compared with an aerial scanner, which are important parameters when gathering geometric data of slender L-shaped profiles,

- The required geometrical model constrains should be defined prior to the data acquisition process. Using the approach proposed in the study as a set of guidelines and recommendations allows to make a conscious decision on the required data quality,

- Further development of the proposed method is encouraged, increasing the complexity level of the geometrical model will allow to better understand the real behavior of the erected lattice structure. Possible topics for geometrical model generation are the cross-section identification and detailed connection reconstruction.

Potential topics to be addressed for FEA model improvements

- Modelling of a full detail of the one leg bolted connection, considering the high sensitivity of the buckling behavior to the correct boundary conditions definition,

- Defining the cross-section types based on the point cloud data of in-situ structure rather than using design documentation as reference,

- Adding torsional deformation to the geometrical model by determining the orientation of the L-shaped profile in pre-defined cross-sections across the analyzed member,

Possible applications of the geometrical modelling method proposed in this study:

- Applying the method beyond the power grid sector, for e.g. lattice bridges, prefabricated trusses,

- Conduct a design documentation validation study by identifying the deviations between the design and erected structure on a global, member and cross-sectional level,

- Use the geometrical model to obtain information regarding the deformed state of the structure.

Appendices

Appendix A: Analytical results

A.1 Member analysis analytical computation

Appendix A.1 presents the results and computation procedure of the analytical solution based on EN 1993-1-1 [27] performed for the isolated idealized members during the member analysis.

The computational stage will be presented on an example of member 1 (see Section 5.2).

The geometrical properties of the analyzed member are given in Tab. 15.

L 110x10 geometrical properties					
L [mm] =	3097	$I_{y,z}$ [mm⁴] =	2,38E+06	$i_{y,z}$ [mm] =	33,5
t [mm] =	10	I_v [mm⁴] =	9,77E+05	y_0,z_0 [mm] =	25,6
b [mm] =	110	I_u [mm⁴] =	3,78E+06	i_v [mm] =	2,15E+01
u₁ [mm] =	43,3	I_t [mm⁴] =	7,24E+04	i_u [mm] =	4,23E+01
u₂ [mm] =	38,8	I_w [mm⁶] =	6,43E+07		

Table 15 Member 1 geometrical properties- L 110x10 profile

Figure 155 L- shaped cross section

Material proper-ties	
E [GPa]	210
G [GPa]	80,77

Table 16 Material properties

Considering L shaped profiles are susceptible to torsional, flexural and combined torsional-flexural buckling, the critical buckling forces for the three modes had to be calculated.

Flexural buckling mode

The analytical response of flexural buckling mode was computed using the Euler's critical load formula:

$$N_{cr,F} = \frac{\pi^2 EI}{L_w{}^2}$$

Equation 17

where E is the Young's modulus, I is the moment of inertia of member's cross-Section about the critical axis and L_w is the effective buckling length of the analyzed member about the critical axis computed as the unsupported length of the member multiplied by the effective length factor dependent on the boundary conditions about the critical axis.

For all members analyzed in this work identical boundary conditions were defined. For the isolated members in the member analysis simply supported pinned connections have been defined, therefore the effective length factor was equal to 1,0.

The critical axis is the one about which the obtained critical load value is the lowest. For the L shaped profile the bending about the minor v-v axis, portrayed in Fig. 117, v-v defined as Z-Z lead to a critical load for flexural buckling.

Computation carried on the example of member 1:

$$N_{cr,F} = \frac{\pi^2 * 210000 * 9,77\text{E} + 05}{3134^2} = 211,08 \; kN$$

<div align="right">Equation 18</div>

Torsional buckling mode

The elastic critical torsional buckling load was computed according to formula 5.24 from 'Theory of Elastic Stability' [33]. The expression for the elastic critical torsional buckling load is given below:

$$N_{cr,T} = \sigma_{cr,T} * A = \frac{A}{I_o}\left(GI_t + \frac{\pi^2 EI_w}{L_T^2}\right)$$

<div align="right">Equation 19, [33] 5.24</div>

with:

$$\frac{A}{I_o} = i_o^2 = i_v^2 + i_u^2 + u_1^2 + v_1^2$$

<div align="right">Equation 20</div>

where G is the shear modulus, I_t is the torsion constant of the gross cross-Section, I_w is the warping constant of the gross cross-Section, L_T is the torsional buckling length of the member, i_o is the cross-Section polar radius with respect to its shear centre, i_v, i_u are the radiuses of gyration of the gross cross-Section about the v-v and u-u axis, u_1, v_1 are the shear centre coordinates with respect to the centroid of the gross cross-Section. In the given formula, the stress in the through-thickness direction is assumed to be zero and the Poisson's ratio effect is ignored.

The buckling length L_T for torsional and torsional-flexural buckling should be determined taking into account the degree of torsional and warping restraint at each end of the analyzed member. According to [33], for a simply supported opened thin walled member the buckling length L_T can be assumed as the system length. For the FEA performed on isolated members simply supported pinned connections have been defined, therefore L_T for torsional and torsional-flexural buckling has been assumed as equal to the system length.

Computation carried on the example of member 1:

$$N_{cr,T} = \frac{1}{4126,43}\left(80770 * 7,24\text{E} + 04 + \frac{\pi^2 * 210000 * 6,43\text{E} + 07}{3134^2}\right) = 1420,15 kN$$

<div align="right">Equation 21</div>

with:

$$i_o{}^2 = 21,5^2 + 42,3^2 + 43,3^2 + 0^2 = 4126,43 mm^2$$

Torsional-flexural buckling mode

The elastic critical flexural-torsional buckling load was computed according to formulas 5.38 and 5.39 from 'Theory of Elastic Stability' [33]. The expression for the elastic critical flexural-torsional buckling load is derived from formulas given below:

$$\begin{cases} i_o{}^2\left(N_{cr,TF} - N_{cr,F}\right)\left(N_{cr,TF} - N_{cr,T}\right) - N_{cr,TF}{}^2 u_1{}^2 = 0 \\ 1,6 N_{cr,TF}{}^2 - \left(N_{cr,F} + N_{cr,T}\right) * N_{cr,TF} + N_{cr,F} * N_{cr,T} = 0 \end{cases}$$

Computation carried on the example of member 1:

$$\begin{cases} 4126,43\left(N_{cr,TF} - 211,08\right)\left(N_{cr,TF} - 1420,15\right) - N_{cr,TF}{}^2 43,3^2 = 0 \\ 1,6 N_{cr,TF}{}^2 - (211,08 + 1420,15) * N_{cr,TF} + 211,08 * 1420,15 = 0 \end{cases}$$

$$N_{cr,TF} = min, positive\{-1,01; 196,71; 1018,42; 2792,87\} = 196,71 \, kN$$

Resulting Critical Load

The final critical load is the minimal load of the three computed buckling modes

$$N_{cr,TF} = min\{N_{cr,F}; \ N_{cr,T}; \ N_{cr,TF}\}$$

On the example of member 1:

$$N_{cr,TF} = min\{211,08 \, ; 1420,15; 196,71 \, \} = 196,71 \ kN$$

~End of the example

Results for all analyzed isolated members

Table below presents the results for all members analyzed in the member analysis, Tab. 17.

Member ID	x-Section	Ncr,F [kN]	Ncr,T [kN]	Ncr,TF [kN]
M1	L110x10	211,08	1420,15	196,71
M2	L80x7	42,19	777,18	38,45
M3	L65x6	49,19	608,30	43,66
M4	L60x6	67,34	650,46	59,18
M5	L70x6	61,30	562,23	51,56
M6	L80x7	54,30	777,32	46,77

Table 17 Critical buckling loads for flexural, torsional and torsional-flexural bucking for members analyzed in the member analysis

A.2 Analytical calculations for L150x12 horizontal member deformation utilized in Section 3.5

Appendix A.2 presents the analytical computation conducted for the vertical deformation of L150x12 horizontal member loaded by the self-weight. The results are utilized in Section 3.5- *Comparison of the Terrestrial LiDAR point cloud with standard profiles geometry according to EN 1090-2 [22], where the analytical value is used as the reference.*

The L150x12 member is assumed to be a simply supported of length *L= 7m.* The geometrical and material properties are given in Tab. 18.

L150x12 geometrical & material properties			
L [mm] =	7000	G [kg/mm] =	0,02735
t [mm] =	12	I [mm⁴] =	7,37E+06
b [mm] =	150	E [GPa]	210,00
A [mm²] =	3483		

Table 18 Member L150x12 geometrical and material properties

 The vertical deflection of the L150x12 member has been computed using given formula:

$$d = \frac{5}{384} \frac{q_G L^4}{EI} = \frac{5}{384} \frac{0,2735 * 7000^4}{210000 * 7,37E + 06} = 0,6 cm$$

Equation 28

where:

$$q_G \approx G * 10 = 0,2735 \, {N}/{mm}$$

Equation 29

Additionally, a manufacturing out of straightness imperfection based on permissible manufacturing tolerance according to EN 1090-2 has been added to the vertical deformation as follows:

$$d_{tot} = d + d_{manufacturing} = 0,6 + 0,7 = 1,3 cm$$

Equation 30

where:

$$d_{manufacturing} = \frac{L}{1000} = \frac{700}{1000} = 0,7 cm$$

Equation 31, Table B.6

Appendix B: Bifurcation results

Appendix B presents the results of the linear buckling FEA conducted for members analyzed in the member analysis. Eigenvalues for the 1st buckling mode are depicted in Fig. 153.
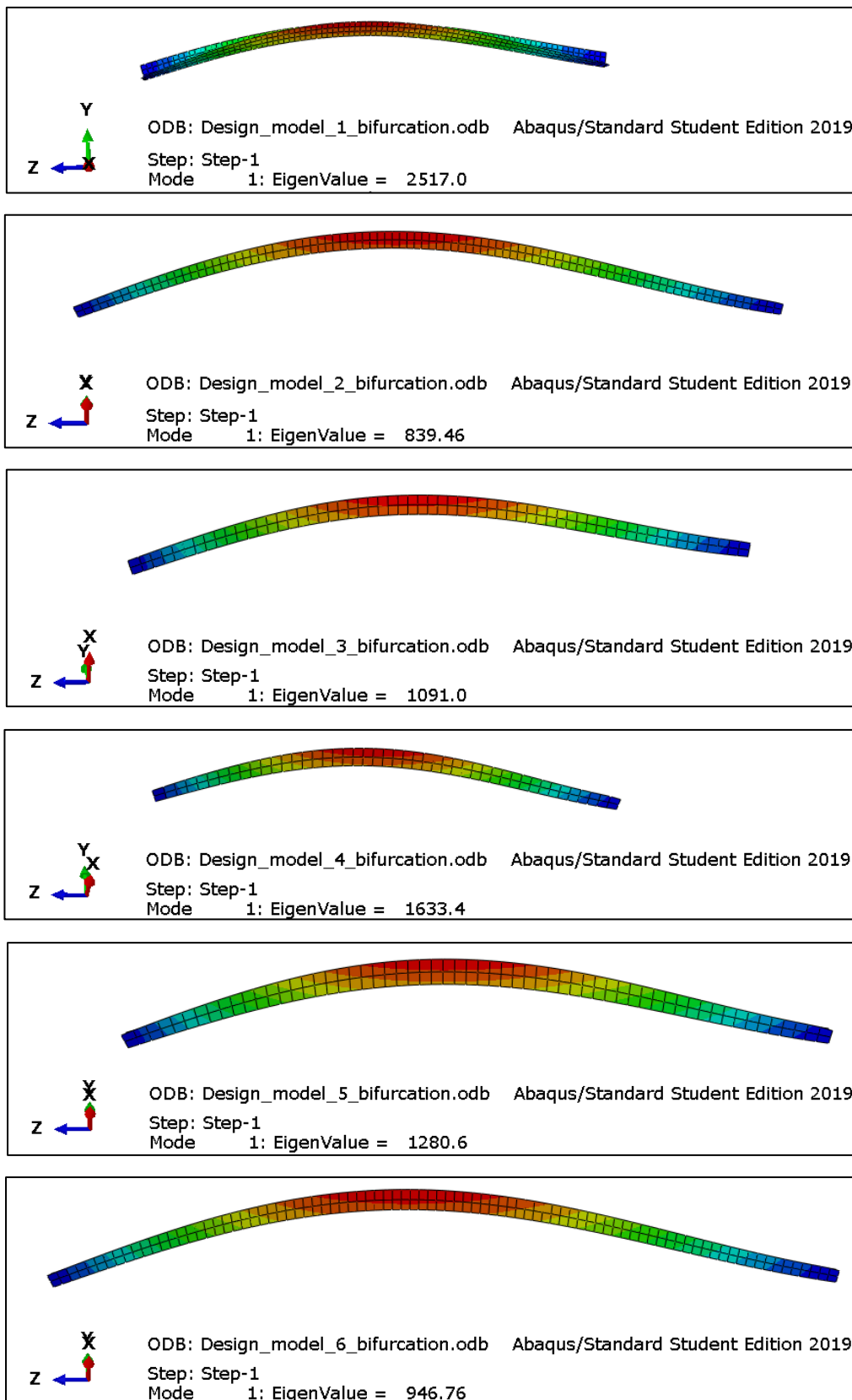
Figure 156 LBA eigenvalues of the first buckling mode. Member analysis

In the Linear buckling analysis performed in Abaqus the isolated members were loaded by a unit shell edge load in the member's longitudinal direction along one legs edge. The units of the shell edge load is force divided by edge length (units FL^{-1}) . In order to compute the critical buckling load value the eigenvalue obtained in the linear buckling FEA needed to be multiplied by the edge of one leg of each L shaped member. The results are presented in Tab. 19.

Member ID	x-Section	Eigenvalue [-]	t [mm]	Ncr [kN]
M1	L110x10	2517	110	276,87
M2	L80x7	839,46	80	67,16
M3	L65x6	1091	65	70,92
M4	L60x6	1633,4	60	98,00
M5	L70x6	1280,6	70	89,64
M6	L80x7	946,76	80	75,74

Table 19 Critical buckling loads for the member linear buckling FEA

Appendix C: Reference point definition for the terrestrial LiDAR point cloud based model

Appendix C presents the terrestrial LiDAR point cloud based model. Each member is discretized by a set of 3 reference points, both end points and the location of the maximum deformation d_{max} defined in Fig. 115. The discretized model is given in Tab. 20 below.

Member Id	X	Y	Z
[-]	[mm]	[mm]	[mm]
1	2194	315.93	2650.8
1	1693.9	441.2	3394.4
1	721.47	639.2	4726.1
2	325.86	2258.1	2592.6
2	468.65	1571.8	3550.9
2	639.41	735.29	4713.5
3	2369.4	16567	2579.7
3	1698.1	16427	3507.4
3	839.04	16252	4713.7
4	14630	258.54	2562.4
4	15269	389.36	3448
4	16169	576.52	4714.7
5	754.72	16171	4706.4
5	557.29	15299	3498.6
5	412.8	14633	2577.4
6	16284	665.57	4723.8
6	16403	1389.8	3699.7
6	16617	2193.3	2594.7
7	16633	14566	2578.4
7	16498	15262	3548.2
7	16329	16096	4711.5
8	16247	16187	4708.6
8	15401	16368	3538.7
8	14710	16524	2586.9
9	3524.2	13423	6619.2
9	2133.8	13313	5442.6
9	612.47	13197	4142.7
10	13460	3400	6613.6
10	13332	1930.4	5381.2
10	13223	490.43	4160.8
11	3497.8	3428.8	6624.2
11	3611.5	1948.9	5373.1
11	3714.3	526.96	4158.1
12	16399	3647	4156.8
12	15198	3558.4	5174.4
12	13474	3430.3	6611.6
13	13512	13382	6621.2
13	14921	13256	5428.8
13	16414	13128	4147.1
14	13272	16314	4159.9
14	13373	14944	5326.5
14	13496	13403	6623.8
15	3499.7	3432.1	6624.6
15	1808.4	3602	5231.2
15	562.83	3708.4	4160.5
16	16048	13865	6898.1
16	16367	16115	4711.4
16	16367	16115	4711.4
17	951.62	2957.9	6892.7
17	826.1	2155.3	6126
17	601.76	689.39	4723.6
18	16199	549.64	4719.3
18	15174	688.91	5699.6
18	13952	878.81	6890.4
19	16006	2891.3	6884.2
19	16118	1993	6030.6
19	16306	644.25	4715.9
20	3051.1	15966	6895.5
20	2329.5	16071	6188.2
20	835.32	16279	4753.8
21	16275	16220	4706.4
21	15091	16063	5851.9
21	14011	15920	6889.1
22	2976.9	910.42	6899.4
22	2015.2	788.72	5991.7
22	706.39	606.38	4726.6
23	1000.5	13934	6877.1
23	903.89	14702	6145.6
23	707.18	16143	4732.5
24	1291.4	4033.7	9227.8
24	1438.3	2758.8	10388
24	1570.9	1559.2	11458
25	15376	1519.4	11449
25	15482	2473.1	10603
25	15669	3948.1	9211.9
26	1541.4	6514.1	11320
26	1402.8	5096.9	10052
26	1298	4198.9	9231
27	15658	4091.2	9212.8
27	15537	5116.8	10134
27	15373	6439.6	11332
28	4047.5	1247.4	9224.3
28	2827.4	1397.2	10330
28	1590.5	1543.5	11449
29	6487.4	1538.8	11334
29	4182.1	1245.2	9225.8
29	4182.1	1245.2	9225.8
30	6566.6	15381	11342
30	4980.2	15555	9885.6
30	4270.2	15639	9228
31	15713	12795	9215.3
31	15573	14029	10342
31	15434	15279	11459
32	1313.9	12899	9199
32	1476.2	14085	10345
32	1610.9	15344	11391
33	12947	15589	9222.9
33	14174	15439	10335
33	15412	15298	11457
34	4062	15630	9246.8
34	2965	15504	10257
34	1637	15371	11424
35	15344	1481.5	11451
35	14453	1383.3	10652
35	12889	1204.8	9222.3
36	15445	15040	11360
36	15316	14048	12353
36	15164	12482	13605
37	14477	4365.7	17923
37	14309	3430.4	18942
37	14153	2762.7	19666

38	2756	2727.8	19678	53	3133.6	4013.9	22232	68	12037	4848.2	8995.9
38	4452.7	2469.6	17931	53	3890.1	6079.9	23572	69	12071	11948	9003.7
38	4452.7	2469.6	17931	54	3052.6	13912	21528	69	11488	14109	7739.2
39	14244	14101	19756	54	4624.2	13759	22586	69	10979	16001	6619.4
39	13530	14215	18970	54	6230.6	13619	23660	70	16073	10837	6618.9
39	12564	14384	17916	55	6195.3	3261.7	23680	70	14121	11384	7779.9
40	2815.9	2815	19685	55	4531.2	3112.3	22565	70	12071	11962	9000
40	2615.7	3351	19090	55	3029.6	2982.5	21549	71	16046	5935.1	6636.1
40	2481.8	4422	17926	56	13882	13896	21439	71	14096	5406.2	7791.7
41	2806.2	14117	19684	56	12431	13745	22517	71	12042	4844	8996.7
41	2628.6	13088	18590	56	10786	13594	23631	72	14030	2947.2	21667
41	2517	12488	17910	57	13948	2941.3	21534	72	13824	4857.7	22841
42	14517	12424	17916	57	12376	3091.6	22592	72	13684	6141	23628
42	14371	13387	18967	57	10821	3246.1	23660	73	13955	13861	21551
42	14286	14042	19678	58	4526.1	15102	13521	73	13821	12029	22763
43	4481.7	14417	17903	58	3229.5	15199	12671	73	13672	10676	23659
43	2945.4	14211	19616	58	1932.7	15388	11271	74	3311.2	10696	23624
43	2945.4	14211	19616	59	12583	14922	13618	74	3178.1	12330	22600
44	14210	2649.3	19706	59	14048	15105	12491	74	3017.2	13907	21588
44	13426	2539.9	18864	59	15350	15259	11448	75	1974.7	12501	13615
44	12544	2428.1	17886	60	10487	15282	11372	75	1821.4	13779	12632
45	6506.4	2725.9	19785	60	11816	15454	10131	75	1662.9	15215	11485
45	5128.1	2829.5	20464	60	12809	15583	9220.7	76	15703	12641	9188.9
45	3002.3	3028.9	21492	61	15296	1528.8	11462	76	15582	11602	10199
46	14209	6417.8	19781	61	14152	1633	12362	76	15446	10302	11323
46	14080	4772.1	20592	61	12581	1817.3	13620	77	15016	4316.5	13632
46	13907	2921.5	21488	62	1620.1	1577.9	11441	77	15213	2882.7	12499
47	2800.6	10428	19784	62	3078.8	1735.7	12591	77	15373	1560.7	11447
47	2897.9	11828	20469	62	4418.7	1886.5	13629	78	1569.2	1617.2	11462
47	3091.5	13923	21473	63	12730	1206.5	9221.2	78	1694.4	2714.7	12320
48	14231	10359	19795	63	11673	1335.3	10196	78	1883.8	4384.4	13630
48	14124	12231	20701	63	10416	1473.9	11315	79	1330.8	12654	9227.9
48	13988	13857	21525	64	941.24	10899	6619.9	79	1503.3	11279	10481
49	14002	13854	21478	64	3123.2	11494	7921.2	79	1627.4	10381	11339
49	12026	14000	20518	64	4957.2	12000	9001.5	80	3537.7	13438	6626
49	10518	14137	19776	65	913.84	5995.5	6625.7	80	3669.5	14903	5381.2
50	2896.4	2985.9	21502	65	2886.8	5447.9	7799.5	80	3797.8	16366	4129
50	2884.2	4159.7	20921	65	4929	4877.1	8992.2	81	661.11	4371.9	4874.7
50	2855.5	6462.9	19782	66	4927.8	4877.1	8986.2	81	864.64	3345.2	6339.5
51	13948	2909.9	21512	66	5490.2	2805.4	7780.7	81	1335.3	1320.3	9240.6
51	11491	2764.2	20293	66	6017	869.47	6626.2	82	4334.3	636.49	4950.5
51	10456	2708.9	19780	67	6077.9	15998	6631.3	82	3063.5	903.22	6773.8
52	6475.8	14162	19688	67	5575.8	14196	7704.1	82	1335.5	1269	9227.6
52	4426	14023	20821	67	4928.6	11995	8987.7	83	15603	1210	9223.6
52	3015.3	13955	21457	68	10921	849.23	6638	83	13670	816.24	6490.2
53	3067.2	2993.1	21536	68	11469	2796.3	7791.3	83	12480	579.44	4784

84	16291	4329	4884.4	99	2232.8	12826	9206.7	114	4293.7	9173.1	25940
84	16052	3181.1	6480.5	99	1417.1	12016	9206	115	6004.5	3705.7	25975
84	15648	1249.9	9238.5	100	3148	13736	9207.7	115	5282.8	4351	25952
85	714.94	12514	4864.3	100	4002.7	14578	9211.3	115	5281	4352.9	25952
85	1040.8	14090	7097.9	100	4959	15532	9218.5	116	6119.8	13300	25963
85	1365.4	15564	9223.8	101	15655	1209.4	9225.3	116	5233.9	12500	25950
86	1392.8	15634	9222.1	101	8872.1	1239.6	9228.7	116	3705.5	10922	25960
86	3242.3	15996	6618.5	101	1297.9	1274.5	9231.9	117	6056.7	6032.5	25912
86	4473.3	16238	4870.1	102	15699	15554	9179.2	117	5179.4	5990.5	25922
87	16314	12453	4867.3	102	8631.1	15595	9251.9	117	3662	6061.5	25940
87	16032	13907	6953.5	102	1365.7	15626	9185.6	118	6085.1	10950	25928
87	15706	15515	9226.1	103	11511	4946.5	9089.2	118	6106	8552.7	25926
88	12594	16210	4881.8	103	11511	4946.5	9089.2	118	6057.9	6073.9	25922
88	13938	15926	6781.2	103	11511	4946.5	9089.2	119	8489.4	3606.9	25962
88	15654	15569	9223.5	104	6617	5510	25940	119	7457.7	4654.7	25950
89	1589.2	12188	9201.4	104	6057.1	6043.9	25932	119	6612.4	5504.7	25940
89	2444.1	13031	9204.9	104	6057.1	6043.9	25932	120	8385.1	13273	25959
89	3298.9	13873	9198.2	105	10908	5887.2	25915	120	7265.8	12002	25937
90	4742.6	15314	9217.7	105	9073.3	4081.8	25952	120	6178.8	10967	25932
90	4103.7	14680	9210.8	105	9073.3	4081.8	25952	121	9073.3	4081.8	25952
90	3465.3	14046	9209.3	106	13325	5870.6	25966	121	8535.6	3606.9	25970
91	6623.2	15609	9248.5	106	12630	5252.1	25966	121	8535.6	3606.9	25970
91	7123.2	15607	9250.8	106	12132	4770.3	25964	122	10957	10965	25929
91	7622.9	15608	9253.4	107	5280.2	4352	25953	122	9486.2	12309	25939
92	8671.3	15592	9258.5	107	4726.1	4929.2	25950	122	8482.2	13213	25945
92	8172.1	15602	9255.1	107	3655.2	5954.9	25950	123	12132	4770.3	25964
92	7671.8	15604	9258.2	108	6061	6119.9	25938	123	12022	4662.5	25964
93	8272.4	15598	9258.2	108	4646	7459.5	25941	123	11043	3588	25961
93	9071.8	15595	9251.4	108	3698.6	8469.6	25953	124	12137	12053	25946
93	9871.8	15589	9251.3	109	13290	8399.7	25966	124	11760	12444	25951
94	11671	4946.9	9083.6	109	12294	7391.7	25936	124	11601	12611	25952
94	10871	4946.7	9082.5	109	10911	6045.2	25923	125	13063	8656	25955
94	10071	4948.2	9078.1	110	3662.6	8588.6	25952	125	12852	8869.8	25950
95	11072	15584	9234.1	110	4298.3	9167.9	25940	125	12644	9085.6	25946
95	10572	15586	9240.3	110	4298.3	9167.9	25940	126	1316.6	1274	9215
95	10072	15589	9245.1	111	10936	10823	25925	126	1313.5	8644.4	9236.1
96	15685	9354.2	9228	111	12270	9455.9	25942	126	1368.1	15622	9202.4
96	15688	10561	9222.9	111	13315	8403.6	25957	127	13306	3576	25876
96	15700	12554	9214.8	112	13360	10854	25953	127	8477.8	3604.1	25857
97	5043.2	4986	9103.1	112	12573	11642	25951	127	3623.3	3630	25871
97	5033.3	8333.6	9078.5	112	12167	12085	25948	128	3642.5	3631.2	25872
97	5067.3	11890	9099.9	113	11601	12611	25952	128	3638.9	8147.3	25847
98	15708	15557	9214.4	113	11370	12855	25953	128	3735.9	13322	25871
98	15679	8465.8	9226.8	113	10981	13250	25954	129	13322	13251	25865
98	15638	1216.4	9221.4	114	6012.4	10867	25924	129	13341	7621.3	25853
99	2943.7	13529	9207.5	114	5080.6	9840.4	25932	129	13227	3517.9	25878

130	13335	13250	25868	145	4957.9	13820	9172	160	11957	11852	9096.6
130	7576.1	13295	25859	145	4930.9	11997	9111.8	161	5031.9	4985.5	9089.4
130	3682.3	13313	25864	146	8567	15603	9250.8	161	8698.5	4953.3	9075.2
131	6086.9	10845	25919	146	6588.7	13648	9145.5	161	11932	4944.9	9092.4
131	8882.1	10838	25926	146	4952.6	12027	9103.2	162	15654	4829.9	9202.1
131	10956	10777	25928	147	12099	11972	9103.2	162	13982	4835.1	9161.2
132	6058.1	6084.6	25963	147	10473	13609	9141.6	162	12052	4847.9	9098.3
132	9216.3	6019.6	25924	147	8498.2	15608	9249.8	163	1307.4	4888.2	9222.2
132	10906	6022.9	25922	148	12121	11970	9089.9	163	4918.7	4859.5	9092.9
133	10918	10823	25939	148	13731	10317	9133	163	4918.7	4859.5	9092.9
133	10916	8248.5	25911	148	15700	8367	9213.4	164	13834	2921.1	21556
133	10906	6016.2	25917	149	11959	11861	9084.8	164	10462	2931.8	21560
134	6056.2	6009.2	25950	149	11948	8193.7	9086.5	164	3002.5	3139.2	21551
134	5179.5	5996.7	25961	149	11933	4947.8	9080.6	165	2998.2	3007.3	21544
134	3661.9	6061.4	25975	150	12038	4844.8	9099.5	165	3059.1	11687	21548
135	5992.8	3618.2	25922	150	12039	3357.2	9151.7	165	3072.5	13942	21543
135	6057.9	6073.9	25924	150	12026	1226	9208.8	166	13999	13832	21545
135	6057.9	6073.9	25924	151	4900.7	1254.3	9224.3	166	7620.3	13894	21546
136	6089.7	10954	25920	151	4912.5	3274.4	9148.5	166	3066.1	13944	21563
136	4859.4	10897	25925	151	4917	4859.3	9106.9	167	14023	13820	21555
136	3678.6	10791	25944	152	15684	8422.5	9217.8	167	13975	9738.5	21555
137	13356	10842	25939	152	13784	6539.2	9131.5	167	13902	2911.9	21545
137	10957	10823	25930	152	12071	4842.1	9098.8	168	111.81	16674	381.21
137	10957	10823	25930	153	12049	4830.4	9099	168	721.83	12417	4967.7
138	13330	6012.6	25898	153	10365	3149.1	9135.3	168	1291.7	8490.1	9230.8
138	11793	6014.9	25904	153	8429	1237.8	9227	169	8481.8	15625	9260.8
138	10906	6016.2	25908	154	15584	4836.1	9199.1	169	4488.3	16249	4889.9
139	10905	3590.3	25944	154	13934	3206	9196.9	169	396.77	16892	454.65
139	10911	5151.2	25909	154	12043	1320.7	9212	170	16701	16817	441.14
139	10923	6016	25899	155	4918.7	4850.4	9085.9	170	12453	16202	5030.4
140	6089.7	10950	25920	155	8516.8	1229.7	9223.1	170	8571.8	15632	9252.3
140	6085.5	13303	25929	155	8516.8	1229.7	9223.1	171	-20.687	40.158	390.77
140	6085.5	13303	25929	156	1397.7	4886.7	9225.1	171	1681	1669.6	12159
141	10960	10823	25928	156	3324.9	2954.3	9202.7	171	3643	3603.3	25907
141	10959	11559	25931	156	4898.8	1353.3	9217.7	172	17008	16851	22.828
141	10932	13257	25940	157	1309.3	8495.8	9216.1	172	15421	15259	11500
142	4951.9	11998	9109.1	157	3207.9	6581.7	9130.2	172	13356	13236	25951
142	3064.2	12003	9162.1	157	4907.9	4858.9	9090.9	173	13325	3551.8	25858
142	1334	12020	9218.5	158	1316.3	8402.3	9233.2	173	15238	1619.3	12263
143	12082	11958	9095.1	158	3254.3	10341	9128.5	173	16885	-39.163	214.9
143	13963	11955	9159.7	158	4929.1	11999	9113.5	174	129.41	16903	37.546
143	15696	11952	9211	159	12081	15502	9214	174	1720.5	15255	11979
144	12085	11957	9089.8	159	13689	13876	9197.6	174	3692	13286	25971
144	12084	13832	9163.8	159	15620	11950	9202.9	175	8499.7	1211.1	9217.9
144	12091	15577	9211.5	160	5052.6	11886	9094.5	175	12602	566.7	4782.9
145	4963.8	15617	9224.9	160	8671.5	11888	9084.6	175	16481	-32.008	587.95

176	8506.8	1239.9	9389.1	191	6849.2	13690	23099	206	456.02	16575	2451.2
176	3416.8	474.74	3834.6	191	3754.9	13343	25867	207	16628	16496	2439.5
176	237.08	10.722	445.16	192	8479.7	13870	21546	207	15538	16521	2450.1
177	16901	206.36	458.39	192	10647	13599	23510	207	14787	16542	2451.2
177	16310	4228.5	4783.3	192	13279	13275	25861	208	13197	475.84	4170.4
177	15699	8341.7	9230	193	8436.2	2953.8	21557	208	14950	2214.5	4159.9
178	15701	8418.6	9221.2	193	10899	3245	23784	208	16399	3644	4156.5
178	16307	12377	4947.6	193	13201	3504.8	25862	209	4239.9	608.43	4716.5
178	16948	16592	387.37	194	8509.3	2980.5	21557	209	2793.6	627.08	4720.4
179	25.912	329.07	524.29	194	5877.1	3314.1	23962	209	681.83	640.69	4715.1
179	641.27	4254.7	4745.2	194	3704.4	3584.5	25894	210	12589	572.94	4716.5
179	1288.7	8401.8	9240.8	195	2227.7	2195.2	15907	210	14379	574.76	4718.6
180	15689	8351.4	9225.6	195	2594	4846.1	18310	210	16257	583.91	4713.5
180	15202	11939	13079	195	3033.2	8417.1	21551	211	16333	16177	4704.7
180	14802	14654	15996	196	2228.6	14689	15925	211	14368	16208	4717.6
181	14721	2128.2	15986	196	2600.1	11799	18535	211	12771	16231	4720.8
181	15158	5190.1	12706	196	3021.8	8495.5	21551	212	751.5	16325	4721.2
181	15682	8424.8	9226.3	197	14749	14384	16153	212	2660.2	16225	4706.3
182	1297	8482.2	9232	197	14376	11565	18690	212	4358.9	16302	4728.7
182	1700.9	5691	12230	197	13939	8436.1	21556	213	16044	5943.4	6633.8
182	2217.3	2185.5	15998	198	14758	2140.1	15911	213	13486	3438.2	6610.8
183	2280.9	14692	15993	198	14459	4670.8	18201	213	10899	834.82	6650.9
183	1868.4	11898	12969	198	13986	8352.4	21539	214	6026.8	860.18	6631.2
183	1324	8420.7	9235.1	199	3639.6	13200	25856	214	3526	3398.2	6626
184	8491.2	15606	9250.8	199	3382.1	11112	23996	214	949.5	5978.2	6636.2
184	11774	15056	12754	199	3047.7	8393.5	21531	215	1002.6	10956	6631.1
184	14789	14632	15975	200	3593.2	3700.3	25870	215	3503.4	13401	6622.8
185	14718	2116.9	15978	200	3216.9	6893.7	22995	215	6103.9	15992	6635
185	12389	1779.5	13481	200	3009.6	8468.5	21568	216	2759.2	925.43	6955.4
185	8407.4	1211.7	9219.5	201	13342	3631.9	25889	216	2057.2	920.82	6957.8
186	8514.1	1236.3	9221	201	13763	6917.6	22930	216	940.87	928.57	6956.1
186	5284.4	1745.6	12696	201	13953	8426.3	21557	217	14136	868.96	6957.7
186	2229.2	2213.1	15997	202	13381	13122	25864	217	14738	864.52	6957.8
187	14847	14682	15853	202	13657	11021	23963	217	15997	856.17	6952.1
187	11667	14277	18726	202	13979	8346.6	21549	218	16051	15908	6942.1
187	8546.5	13890	21542	203	8557.1	15703	9259.7	218	14914	15907	6955.1
188	8495.2	13862	21561	203	5274.1	15137	12760	218	14212	15907	6950
188	4966.1	14337	18341	203	2267.1	14720	15990	219	2842.8	15955	6955.9
188	2259.4	14694	15904	204	2154.8	288.98	2441.9	219	2041.7	15973	6953.8
189	8441.2	2940.3	21570	204	1576.1	296.96	2453.4	219	984.73	15981	6942.5
189	5589	2594	18955	204	312.21	323.17	2420.5	220	340.33	317.1	2460.2
189	2209.9	2137.5	15931	205	16583	259.42	2454.2	220	302.19	1526.8	2461.5
190	8523.3	2988	21570	205	15492	253.5	2448	220	322.91	2135.6	2458.5
190	11831	2536.4	18534	205	14712	239.59	2453.4	221	16619	2062.4	2452.4
190	14723	2151.8	15915	206	2261.5	16590	2448	221	16602	1402.9	2453.5
191	8558.6	13890	21525	206	1663.7	16584	2444.9	221	16586	264.13	2443.4

222	438.61	16577	2438.1
222	412.91	15476	2441.5
222	393.66	14748	2444.2
223	16658	14691	2448.5
223	16648	15503	2440.9
223	16651	16495	2443.3
224	558.62	3703.3	4164
224	2094.4	2157.8	4160.5
224	3709.2	532.21	4159.3
225	3798.7	16341	4156.1
225	2299.6	14854	4158.1
225	624.49	13199	4152
226	13260	16322	4159.4
226	14799	14761	4157.3
226	16413	13128	4150.7
227	652.45	4233.4	4727.5
227	654.62	2573.3	4725.6
227	664.94	636.29	4721.3
228	16313	4177	4723.1
228	16288	2628.3	4718.8
228	16263	584.32	4713.7
229	16334	12594	4709.9
229	16333	14205	4709.2
229	16337	16178	4711.3
230	741.13	16256	4706
230	726.42	14288	4706.7
230	691.23	12660	4717.5
231	11032	15918	6635.3
231	13477	13416	6622.1
231	16072	10821	6618.6
232	960.29	2933.4	6955.7
232	950.42	2149.9	6965.6
232	944.46	933.65	6942
233	16000	856.15	6959.3
233	15992	1896.9	6962.8
233	15996	2834.1	6963.5
234	16040	13903	6953.6
234	16053	14868	6955.3
234	16063	15908	6959.7
235	1024.9	16041	6945.8
235	1012.1	14942	6951.2
235	1020.6	13988	6949.7
236	10598	1517.6	11456
236	12812	1521.5	11456
236	15375	1513.7	11449
237	15407	15303	11443
237	12921	15275	11457
237	10604	15264	11454
238	1528.9	1534.5	11477
238	4261.1	1552.5	11451
238	6404.5	1550.2	11469
239	1686.1	15322	11448
239	4179	15335	11454
239	6439.7	15357	11468
240	4368.2	1897.1	13655
240	3057.3	1886.5	13665
240	1875	1893.2	13663
241	15076	1831.8	13663
241	13720	1819.5	13669
241	12684	1816.6	13674
242	12807	14926	13657
242	13803	14936	13659
242	15144	14964	13661
243	1946.3	15057	13634
243	3254	15062	13669
243	4451.9	15081	13624
244	15361	6338.6	11460
244	15361	3876.2	11454
244	15377	1524.8	11459
245	15403	10486	11455
245	15400	12740	11445
245	15401	15298	11445
246	1610.2	6307.3	11459
246	1606.8	4207.1	11452
246	1605.5	1541.6	11455
247	1633.2	10485	11456
247	1632.5	12737	11448
247	1628.3	15320	11462
248	1798.6	1882.7	13684
248	1875.8	3007.4	13672
248	1622.6	4345.5	13709
249	15081	1809.1	13623
249	15067	2594.1	13647
249	15026	4286	13666
250	15124	14965	13654
250	15146	12837	13609
250	15132	12416	13606
251	1988.5	12540	13650
251	1963.1	13725	13658
251	1944.6	15057	13641
252	4378.2	2436.7	17820
252	3436.1	2458.3	17819
252	2408.3	2469	17837
253	14597	14356	17823
253	13320	14385	17810
253	12650	14390	17810
254	4346.3	14370	17963
254	3287.4	14458	17779
254	2533.1	14458	17824
255	10627	14130	19677
255	12289	14121	19680
255	14344	14096	19673
256	14072	2634	19681
256	12258	2673.7	19676
256	10525	2693.4	19683
257	6466.3	2707.9	19684
257	4771.5	2721.8	19682
257	2767.7	2741.5	19710
258	6311.5	14157	19677
258	5070.5	14174	19664
258	2802.1	14188	19679
259	2474.9	4352.5	17866
259	2447.8	3266.1	17827
259	2429.9	2475.2	17854
260	14600	14333	17829
260	14584	13444	17820
260	14558	12555	17797
261	14492	4285.9	17850
261	14480	3210.8	17851
261	14460	2408	17855
262	2535.6	14472	17813
262	2518.2	13354	17811
262	2509.3	12597	17811
263	14330	10506	19675
263	14321	12266	19681
263	14345	14109	19675
264	14236	6305.1	19680
264	14217	4787.8	19682
264	14185	2554.6	19672
265	2815.9	6366.6	19674
265	2701	4779.1	19694
265	2755.5	2736.2	19686
266	2818.3	14213	19673
266	2786.3	12117	19678
266	2772.5	10543	19678
267	13694	13658	23709
267	12102	13635	23707
267	10836	13619	23682

268	13703	3249.2	23720
268	12218	3252.1	23713
268	11099	3247.2	23718
269	3336.9	13601	23713
269	4760.7	13597	23706
269	6028.5	13604	23708
270	6143.2	3223.4	23716
270	4606.1	3220.7	23722
270	3450.1	3227.3	23723
271	13614	10732	23712
271	13624	12232	23699
271	13641	13673	23710
272	13691	3246.7	23712
272	13704	4360.8	23722
272	13705	6073	23685
273	3334.1	13601	23712
273	3336.9	11861	23717
273	3324.3	10825	23691
274	3291.7	6105.5	23721
274	3379.9	4784.1	23710
274	3374.6	3221.2	23715
275	14460	2414.6	17850
275	13518	2454.2	17844
275	12596	2461.6	17840

Table 20 Terrestrial LiDAR point cloud based model reference points

Bibliography

[1] Klinger, C., M. Mehdianpour, D. Klingbeil, D. Bettge, R. Häcker, and W. Baer. 'Failure Analysis on Collapsed Towers of Overhead Electrical Lines in the Region Münsterland (Germany) 2005'. Engineering Failure Analysis, The Fourth International Conference on Engineering Failure Analysis Part 2, 18, no. 7 (1 October 2011): 1873–83.

[2] 'VDE-AR-N 4210-4'. (August 2014).

[3] Phan, Anh Thu Thi, and Ngoc Thi Huynh. 'Generating 3D Point-Cloud Based on Combining Adjacent Multi-Station Scanning Data in 2D Laser Scanning: A Case Study of Hokuyo UTM 30lxk'. Archives of Civil Engineering Vol. 67, no. nr 4 (2021).

[4] Barazzetti, Luigi, Fabrizio Banfi, Raffaella Brumana, Gaia Gusmeroli, Mattia Previtali, and Giuseppe Schiantarelli. 'Cloud-to-BIM-to-FEM: Structural Simulation with Accurate Historic BIM from Laser Scans'. Simulation Modelling Practice and Theory 57 (September 2015): 71–87.

[5] Stałowska, Paulina, Czesław Suchocki, and Miłosława Rutkowska. 'Crack Detection in Building Walls Based on Geometric and Radiometric Point Cloud Information'. Automation in Construction 134 (1 February 2022): 104065.

[6] Xu, Yusheng, and Uwe Stilla. 'Toward Building and Civil Infrastructure Reconstruction From Point Clouds: A Review on Data and Key Techniques'. IEEE Journal of Selected Topics in Applied Earth Observations and Remote Sensing PP (19 February 2021): 1–1.

[7] Conde-Carnero, B., B. Riveiro, P. Arias, and J. C. Caamaño. 'Exploitation of Geometric Data Provided by Laser Scanning to Create FEM Structural Models of Bridges'. Journal of Performance of Constructed Facilities 30, no. 3 (June 2016)

[8] Wang, Qian, and Min-koo Kim. 'Applications of 3D Point Cloud Data in the Construction Industry: A Fifteen-Year Review from 2004 to 2018'. Advanced Engineering Informatics 39 (1 January 2019): 306–19.

[9] Truong-Hong, Linh, and Debra F. Laefer. 'Octree-Based, Automatic Building Façade Generation from LiDAR Data'. Computer-Aided Design 53 (August 2014): 46–61.

[10] Vosselman, G. (George), and Hans-Gerd Maas. 'Airborne and Terrestrial Laser Scanning'. Whittles Publishing, 2010.

[11] Silverman, B.W. 'Density Estimation for Statistics and Data Analysis'. 1986.

[12] Kamdi, Shilpa, and R Krishna. 'Image Segmentation and Region Growing Algorithm'. Int. J. Comput. Technol. 2 (1 January 2012).

[13] Hough, P. V. C. 'Machine Analysis of Bubble Chamber Pictures'. Edited by L. Kowarski. Conf. Proc. C 590914 (1959): 554–558.

[14] Baronti, Luca, Mark Alston, Nikos Mavrakis, Amir Ghalamzan, and Marco Castellani. 'Primitive Shape Fitting in Point Clouds Using the Bees Algorithm'. Applied Sciences 9 (29 November 2019).

[15] Schnabel, R., R. Wahl, and R. Klein. 'Efficient RANSAC for Point-Cloud Shape Detection'. Computer Graphics Forum 26, no. 2 (June 2007): 214–26.

[16] 'RIEGL_VZ-400i_Datasheet'. (2019).

[17] 'EN 1992-1-1', (2004).

[18] Delaunay, Boris. 'Sur La Sphère Vide'. (1934).

[19] Kazhdan, Michael, Matthew Bolitho, and Hugues Hoppe. 'Poisson Surface Reconstruction'. (2006).

[20] Lu, Xiaohu, Yahui Liu, and Kai Li. 'Fast 3D Line Segment Detection From Unorganized Point Cloud'. ArXiv:1901.02532 [Cs], 8 January 2019.

[21] 'EN 50341-1'. (2012).

[22] 'EN 1090-2'. (2008).

[23] Laefer, Debra F., and Linh Truong-Hong. 'Toward Automatic Generation of 3D Steel Structures for Building Information Modelling'. Automation in Construction 74 (1 February 2017): 66–77.

[24] Gargantini, Irene. 'An Effective Way to Represent Quadtrees'. Communications of the ACM 25, no. 12 (December 1982): 905–10.

[25] Lehmann, Maja, Schneider, Kai. 'Statische Berechnung fur: Mastschaft mit Quertragern, Donau + Einebene'.(30 October 2019).

[26] Ramalingam, Raghavan. 'Failure Analysis of Lattice Tower like Structures'. IOP Conference Series: Earth and Environmental Science 80 (July 2017): 012024.

[27] 'EN 1993-1-1', (2005).

[28] 'Abaqus/CAE User's Manual'. (2011).

[29] Jain, Amit, and Durgesh C. Rai. 'Lateral-Torsional Buckling of Laterally Unsupported Single Angle Sections Loaded along Geometric Axis'. Journal of Constructional Steel Research 102 (1 November 2014): 178–89.

[30] S. Sirqueira, A. da, L. R. O. de Lima, P. C. G. da S. Vellasco, F. R. Sarquis, and A. T. da Silva. 'Experimental and Numerical Assessments of Hot-Rolled Carbon Steel Fixed-Ended Angles in Compression'. Thin-Walled Structures 157 (1 December 2020): 107018.

[31] Mesacasa, Enio, Pedro Borges Dinis, Dinar Camotim, and Maximiliano Malite. 'Mode Interaction in Thin-Walled Equal-Leg Angle Columns'. Thin-Walled Structures, COUPLED INSTABILITIES IN METAL STRUCTURES, 81 (1 August 2014): 138–49.

[32] 'EN 1993-3-1', (2006).

[33] Timoshenko, Stephen P., and James M. Gere. 'Theory of Elastic Stability'. Courier Corporation, 2012.

[34] Wu, Z., H. Wang, W. Yu, J. Xi, W. Lei, and T. Tang. '3D HIGH-EFFICIENCY AND HIGH-PRECISION MODEL-DRIVEN MODELLING FOR POWER TRANSMISSION TOWER'. The International Archives of the Photogrammetry, Remote Sensing and Spatial Information Sciences XLIV-4/W3-2020 (23 November 2020): 421–26.

[35] A Transmission Tower Tilt State Assessment Approach Based on Dense Point Cloud from UAV-Based LiDAR'. Accessed 13 June 2022.